BILINGUAL
PUBLISHING CO.
Pioneer of Global Academics Since 1984

Journal of
Mechanical Engineering Research

Volume 4 · Issue 2 · September 2021 | ISSN 2630-4945 (Online)

BILINGUAL
PUBLISHING CO.
Pioneer of Global Academics Since 1984

Editor-in-Chief

Dr. Jan - Awrejcewicz
Lodz university of technology, Poland

Associate Editor

Dr. Kong Fah Tee
University of Greenwich, United Kingdom

Editorial Board Members

Manuel Teixeira Braz-Cesar, Portugal
Gadang Priyotomo, Indonesia
Asit Kumar Parida, India
Ravinder Kumar, India
Milon Selvam Dennison, India
Mohaned El wazziki, Canada
Zichen Deng, China
Khalil Ur Rehman, Pakistan
Ravindra Jilte, India
Ramin Kouhikamali, Iran
Mehdi Safari, Iran
Yihua Cao, China
Xikun Wang, China
Arash Reza, Iran
Mohammad Nimafar, Iran
Kutsİ Savaş Erduran, Turkey
Abdelkader Doudou, Morocco
Wenbin Wang, China
Daniele Cafolla, Italy
Farshad Abbasi, Iran Sathyashankara
Sharma, India Ahmet YILDIZ, Turkey
Lyudmila Ivanovna Gracheva, Ukraine
Samuel Filgueiras Rodrigues, Brazil
Samad Nadimi Bavil Oliaei, Turkey
Pravin Tukaram Nitnaware, India
Majid Jabbari, Iran
Alper Uysal, Turkey
Arnaldo Casalotti, Italy
Matteo Strozzi, Italy
Youliang Huang, China
Vahid Tahmasbi, Iran
Akbar Salemi, Iran
Asim Mukhopadhyay, India
Elammaran Jayamani, Malaysia
Xuejun Jason Liu, United States
Philemon Kazimil Mzee, Tanzania
Yuan Kang, China
Mohammed Diany, Morocco
Shuang Li, China
Ahad - Gholipoor, Iran
Venanzio Giannella, Italy
Hongping Hu, China
Jiusheng Bao, China
Milad Armin, United Kingdom
Yu-Chun Kung, United States
Guang Yih Sheu, Taiwan
Salah Aguib, Algeria
Artur Portela, Brazil
Ambreen Afsar Khan, Pakistan
Hao Wang, China
Wuyi Wan, China
Hossein Hemmatian, Iran
Humaira Yasmin, Saudi Arabia
Bing Yang, China
Ladeesh Vgvg, India
Vinothkumar Sivalingam, India
Saad AbdelHameed EL-Sayed, Egypt
Sedat Yayla, Turkey
Paweł Grzegorz Kossakowski, Poland Mohamed
El-Amine Slimani, Algeria
Mohamed Kamal Ahmed Ali, Egypt
Chew Kuew Wai, Malaysia
Kishore Debnath, India
XinJiang Lu, China
Shahriar - Dastjerdi, Iran
Afshin Zeinedini, Iran
Jinglun Fu, China
Rongyun Zhang, China
Pradeep Kumar Gautam, India
Marcos Rodriguez Millan, Spain
Wei Cao, China
Jan Awrejcewicz, Poland
Nima Ahmadi, Iran
Vipin Nair, India
MD Shamshuddin, India
Reza Aghaei-Togh, Iran

Volume 4 Issue 2 • September 2021 • ISSN 2630-4945 (Online)

Journal of Mechanical Engineering Research

Editor-in-Chief

Dr. Jan - Awrejcewicz

BILINGUAL PUBLISHING CO.
Pioneer of Global Academics Since 1984

BILINGUAL
PUBLISHING CO.
Pioneer of Global Academics Since 1984

Volume 4 | Issue 2 | September 2021 | Page1-51
Journal of Mechanical Engineering Research

Contents

Articles

BILINGUAL PUBLISHING CO.
Pioneer of Global Academics Since 1984

Journal of Mechanical Engineering Research
https://ojs.bilpublishing.com/index.php/jmer

ARTICLE

Analysis of Autogenous Laser Welding in Low Carbon and Large Thickness Steel

Daniel Kohls[1] **Carlos Enrique Ninõ Bohorquez**[2] **Enori Gemilli**[3] **Majorie Anacleto Bernardo**[4*]

1. Federal University of Santa Catarina, Block A of the Department, Florianopolis, SC, 88.040-900, Brazil
2. Department of Mechanical Engineering, State University of Santa Catarina, Rua Paulo Malschitzki, Zona Industrial, Joinville, SC, 89.219-710, Brazil
3. State University of Santa Catarina, Rua Paulo Malschitzki, Zona Industrial, Joinville, SC, 89.219-710, Brazil
4. Federal University of Santa Catarina, Centro Block A of the Department, Florianopolis, SC, 88.040-900, Brazil

ARTICLE INFO

Article history
Received: 21 June 2021
Accepted: 27 July 2021
Published Online: 25 August 2021

Keywords:
Autogenous LASER welding
Welding of thick joints
Keyhole stability

ABSTRACT

With the use of laser welding, it is possible to join different steel, with different thicknesses, with or without the action of protective layers. The quality of laser radiation makes it possible to get certain characteristics that are impossible to get by other processes, such as high welding speeds, less metallurgical effects suffered by the heat-affected zone (ZAC), and this process also does not require filler metal, therefore it is free from possible contamination.

Combined with traditional welding methods, laser welding produces narrower weld beads, allowing for better prevention of corrosion and thermal distortions.

Although the process already has high industrial knowledge, some random defects, such as porosities and inconsistencies, are still found. This work presents a systematic study to determine the influence of laser welding parameters and how these parameters influence welding defects. For this, the experimental part was carried out in the welding laboratory - LABSOLDA, of the Federal University of Santa Catarina - UFSC, during the laser welding processes, a welding speed of 2.4 m/min was reached. For this experiment, argon was used as a shielding gas and 1020 steel was used as the base material.

1. Introduction

Welding is the most used process of joining metallic materials in the world, because of its vast practicality and ease, almost all production principles use welding in their production processes. Besides the production processes, welding is heavily used in equipment maintenance and recovery. One of the great advantages of welding is to get the union of materials, maintaining not only the external appearance but also the continuity of chemical and mechanical properties.

Theoretical Foundation

In 1960, Theodore Maiman [1] presented the first Laser light emission (Light Amplification by Stimulated

---

**Corresponding Author:*
Majorie Anacleto Bernardo,
Federal University of Santa Catarina, Centro Block A of the Department, Florianopolis, SC, 88.040-900, Brazil;
Email: anacletomajorie@gmail.com

DOI: https://doi.org/10.30564/jmer.v4i2.3381

Emission of Radiation). This was the first emission located in the visible range of the electromagnetic spectrum. Since then, the development of this technique for application in the industry has been continuous and encouraged by the good results achieved.

Since then, the development of the potential for application in the industry has been continuous and encouraged by the results achieved.

The physical principle of laser light, or stimulated emission of light came from the theory planned by AlbertEinstein, which postulated that the quantization of energy from harmonic oscillators could also be given as if light comprised “quanta” of energy, and light passed to be described as made up by small amounts of electromagnetic energy, or by photons with the same wavelength, synchronous, and in the same direction and direction as an incident photon as a form of stimulus [2].

The laser welding process involves focusing a high-power beam on a small area, which can generate intensities greater than 104 W/mm^2. At these power levels, the material vaporizes at the laser’s focal point creating a cavity called a keyhole. This cavity helps to transmit the beam into the material by multiple reflections, which increases the coupling between the beam and the material (increased absorptivity) [3].

This stimulated emission should, however, have higher rates than the spontaneous absorption and emission to ensure a larger possible amount of atoms in the excited state to produce another identical photon (light) with the same energy and in phase, in the direction of the incident photon that constitutes the laser beam.

Phenomena such as light reflection and absorption, heat conduction, enable better adequacy of the production process and the choice of material to be worked, influence the laser process, which is related to optical and thermal properties, and not to the mechanical proprieties [4].

Reflectivity, which is the index indicative of the portion of the incident light beam reflected by the workpiece material, can vary with the wavelength of laser radiation. Materials such as aluminum and copper have high reflectivity, which makes laser processing and application difficult. However, as the surface temperature increases, the reflectivity decreases, which forms a reflectivity-minimizing feature.

Figure 1 shows the laser welding process. This stimulated emission should, however, have higher rates than the spontaneous absorption and emission to ensure a larger possible amount of atoms in the excited state to produce another identical photon (light) with the same energy and in phase, in the direction of the incident photon that constitutes the laser beam.

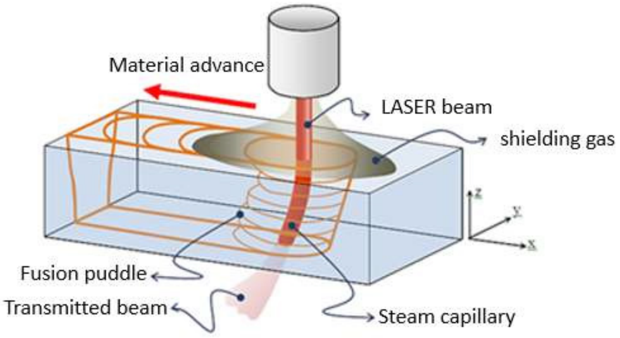

Figure 1. Illustration of the laser welding process

Source: Adapted from MIRIM, 2011

As the laser beam moves to create the bead, materials continuously fused in front of the beam, flowing around the keyhole and solidifying at the back of the weld pool. The intrinsic characteristics of penetration welding establish the maximum and minimum for the process speed: top speeds cause the keyhole to collapse, while very low speeds cause burrs and holes due to the liquid flow [5].

An important concept in welding is welding energy (E) which is defined as the heat given to the weld joint per unit of length (J/mm). The higher the welding energy, the larger the grain size of the molten zone and the larger the heat-affected zone (ZAC). For slower cooling speeds, grains in the region close to the melting line grows. In processes where low values of welding energy are involved, such as in Laser welding, the heat-affected zone (ZAC) is narrow and rarely has a defined grain growth region [6].

In laser welding, there are basically two different techniques, namely conduction welding and penetration welding or Keyhole. The energy density characterizes conduction welding being below 106 W/cm², not generating significant evaporation of the material, only a change in state from solid to liquid [7].

In the penetration welding process, higher energy densities than conduction welding characterize it (between 106 W/cm² and 109 W/cm²), and it is possible to carry out welding of components with great thickness. The difference between the welding techniques can be seen in Figure 2.

For welding low carbon steels, they’re characterized by low strength and hardness, high tenacity, and ductility. They have good machinability, good weldability and are not heat-treated, besides requiring attention in the generation of discontinuities due to the absence (or low percentage) of alloying elements, such as Mn. Besides the low metallurgical complexity, low carbon steels have a simple chemical composition where they do not cause major microstructural changes in the heat-affected zone

DOI: https://doi.org/10.30564/jmer.v4i2.3381

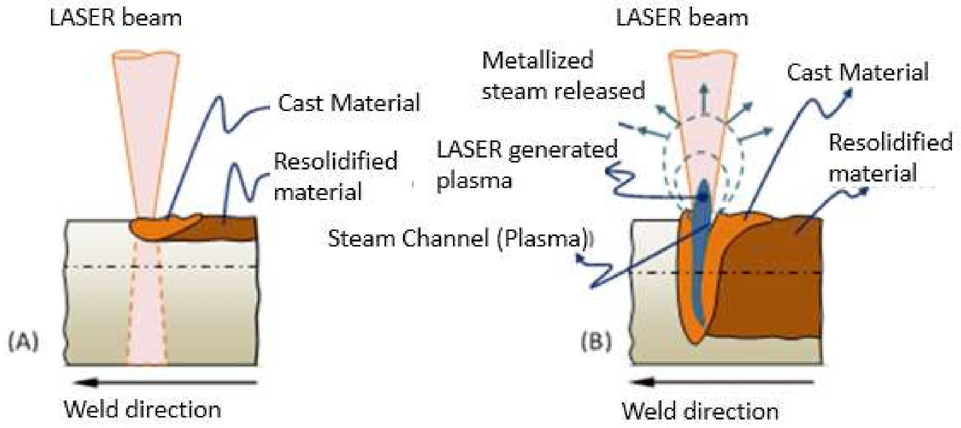

Figure 2. Representation of the conduction welding process (A) and penetration welding (B)

Source: Adapted from ENGEMANN, 1993.

(ZAC). The fusion and solidification of the material does not cause transformations in the crystalline structure that harm the characteristics of the welded joint, having a part without defects and properties and performance required for application [8].

2. Purpose

The objective of this work is to qualify the applicability of the 10 kW IPG fiber laser model YLS-10000 as a processing tool in the autogenous laser welding of thick and low-carbon structural steel joints, varying the laser input parameters and evaluating the metallurgical properties of the welded joints got.

Measure the output variables of the process by analyzing the heat-affected zone (ZAC) and the molten zone of the processed material after interaction with the laser beam between the power of 10 kW at the speed of 2.4 m/min and focus -6 mm. These theoretical-experimental analyses based on empirical information from [9], carried out in the same laboratory, as well as previous experimental procedures.

3. Methodology

The experimental ordering consists of carrying out controlled tests based on the survey and admissible parameters, which result in a good weld quality (without cracks and porosity) and with total penetration into the welded joint. The controlled tests were carried out from the interaction of the Laser light beam with a solid plate just forming a bead on a plate. An important point to be investigated in this work is keyhole stabilization.

The present work was carried out using a10 kW IPG fiber Laser system as a tool for laser welding. The methods comprise carrying out controlled tests, to make a list of admissible parameters, to have weld quality, without cracks and porosity, and with total penetration.

As a base material for welding, SAE 1020 steel was used, which is widely used in the industry in general, whether automotive, civil, naval, or machinery, and as an advantage it has a low cost compared to other steels and alloys because it is a steel with low content of carbon, meeting the requirements proposed in this work.

In Table 1 the chemical composition of SAE 1020 steel presented, according to the Brazilian standard that establishes the numerical designation used to identify carbon and alloy steels, according to their chemical composition (ABNT NBR NM 87: 2000) [10], data on the percentage of chemical elements present in 1020 steel was showed by the manufacturer Gerdal (supplier).

Table 1. Composition of SAE 1020 steel

Element	C (Carbon)	Mn (Manganese)	P (Phosphor)	S (Sulfur)
% (Standard)	0,18 - 0,23	0,30 - 0,60	≤ 0,030	≤0,050
% (Provider)	0,18 - 0,23	0,30 - 0,60	≤ 0,040	≤0,050

Source: SOUZA, 2017.

The 1020 steel plate used in this work has dimensions of 400 x 127 mm with a thickness of 3/8” (value with an order of magnitude suitable for drawing conclusions about the behavior of autogenous high-depth laser welding (thick joint) from a fiber laser source with 10 kW power).

In Figure 3, the distribution of the specimens on the 3/8” plates is observed so that, after welding, these specimens were removed by cutting with a water jet. Specimens in the plate’s layout, the samples destined for

Charpy tests in the regions of the welded joints, as well as the samples used for tensile testing in the same region and finally the samples used for tensile testing of the base material are notorious. For hardness and metallography tests, the same specimens mentioned above will be used.

3.1 Reviews

Evaluating and measuring the output parameters carried the verification of the quality of penetration of the laser beam into the welded parts out, carried out through visual inspection, with the naked eye and the analysis of micrographs (optical microscopy). To verify the microstructure, metallographic preparation of parts of the specimens is necessary.

The samples were prepared on the premises of the Metallographic Preparation Laboratory.Sample preparation was carried out following conventional metallography procedures, following the technical standards showed. In the sanding, the particle sizes 80,120,220,400, 600,800, 1200 were used in sequence. The samples were polished with 1 µm Alumina until reaching the desired surface quality. To allow the visualization of the microstructure of the material, a chemical attack was carried out with Nital 2% reagent (2% HNO_3 by volume of ethanol) for 15 seconds on the surface to be analyzed [11].

The quality verification of laser beam penetration into welded parts was carried out by evaluating and measuring the output parameters, carried out through visual inspection and the analysis of destructive and non-destructive tests discussed in the subsequent items.

3.1.1 Destructive Tests

Charpy traction and impact tests (type A) were performed at room temperature. The purpose of the first test is to evaluate the mechanical strength and ductility of the solder joint and the base metal. Normally, for thin joints, the specimen is removed transversally to the weld bead. For each of the situations, the analysis of the resistance to the last and the stretching was performed to determine the possibility of use or not.

For tensile tests performed in accordance with the Brazilian standard for carrying out tensile tests - ASTM A370-10 [12]. They were performed on an Instron 300LX-C4-J3D instrument. For base metal, a specimen was extracted from the rolled profile in the longitudinal direction of the rolling direction. The respective dimension for this test piece with rectangular cross-section is specified in Figure 4.

Regarding the tensile tests for welded joints, three specimens were extracted for each weld specification in the transverse direction to the lamination of the base metal. The respective dimensions can be seen in Figure 5.

For approval under the API 1104 [13] standard, which standardizes gas and arc welding processes for low-alloy steels, welded joints must meet the following criteria for rupture outside the welded joint and in the welded joint:

a) Breakage outside the welded joint: the breaking limit must meet the minimum strength limit of the base material specification;

b) Breakage in the welded joint: the rupture limit must meet the minimum strength limit of the pipe material specification, as well as in the fracture cross section: no pores larger than 1.6 mm (with the sum of the area not exceeding 2% of the fracture area) and the slag inclusions should not be more than 0.8 mm thick or more than 3 mm long, with a minimum separation of 13 mm between adjacent inclusions.

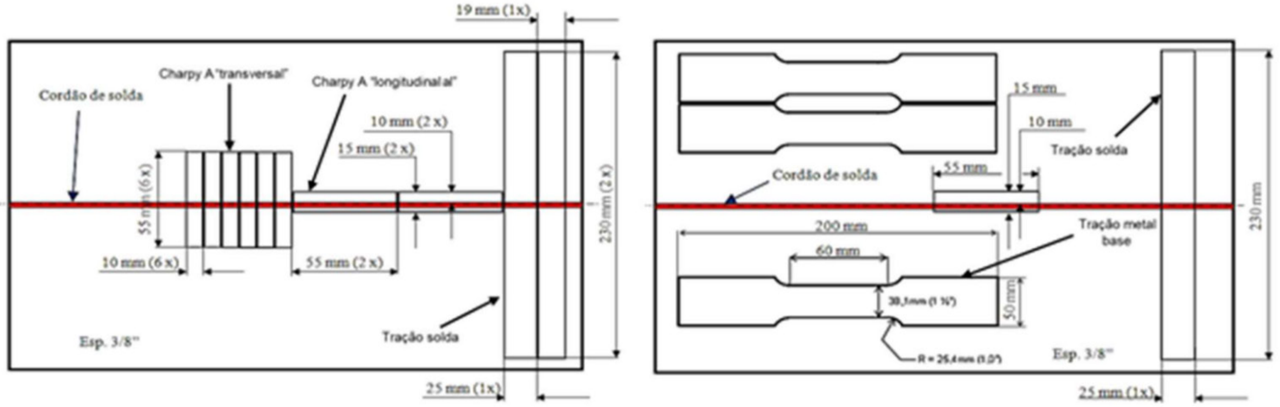

Figure 3. 3/8" x 400 x 127 mm plates intended for autogenous welding, which will be extracted by water cutting the specimens for Charpy A testing and traction on the base metal and welded joint

Source: Prepared by the authors, 2021.

DOI: https://doi.org/10.30564/jmer.v4i2.3381

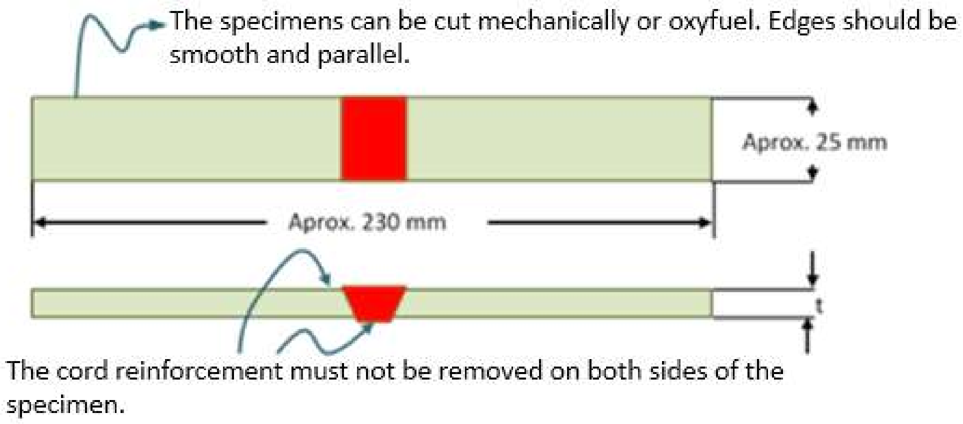

Figure 4. Dimensions of the tensile test specimens for the base metal, with thickness t = 9.54 mm (adapted from API 5L standard, 2007).

Source: Prepared by the authors, 2021.

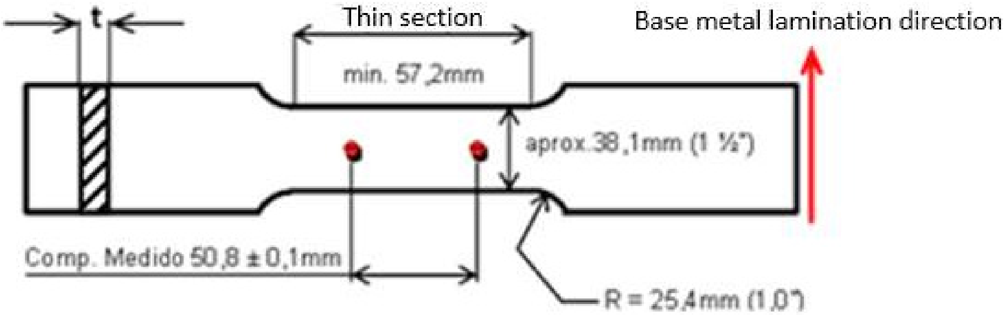

Figure 5. Representation of the tensile test body for the welded joints with the respective characteristic dimensions, being the thickness t = 9.54 mm.

Source: Prepared by the authors, 2021.

For the Charpy type A test, with a V-notch, it was made on the base metal, and in the welded region with the notches in the molten zone and in the heat-affected zone (ZAC), at room temperature as a variation of the ASTM E370 [14] standard in the dimensions of 10 mm x 10 mm x 55 mm, with three replicas for each condition analyzed. The notch was positioned in the thickness plane at positions relative to the center of the weld bead, heat-affected zone (ZAC).

The tests were carried out on the Wolpert universal impact testing machine; with three specimens for each welded joint in the longitudinal direction of the weld bead in the heat-affected zone (ZAC) and molten zone regions and in the transverse direction of the joint. The dimensions of the specimens and the representation of the welded profiles can be seen in Figure 6.

3.1.2 Non-destructive Testing

For the analysis of the macro and microstructure, the metallographic test was carried out by preparing sections of the specimens containing the welded regions of interest according to conventional procedures according to the technical standards indicated.

In the experimental procedure, sanding sectioned transversally and prepared the welded joints following the particle sizes 80, 120, 220, 400, 600, 800, 1200 respectively, with the samples being polished with 1 μm alumina until reaching the desired surface quality. The chemical attack was carried out with Nital 2% (2% HNO3 by volume of ethanol) for 15 seconds on the surface to be analyzed [11].

Vickers hardness tests (HV) were performed using a Future-Tech microhardness tester, model FM-800, and following the guidance of the ASTM E92-82 [15] standard. They were tested for each region of interest, base metal, heat-affected zone, and steel melt zone in the plane normal to the rolling direction and to the weld bead, as seen in Figure 7. In the procedure to get the hardness, a load of 500 g was used for a time of 15 seconds and a distance between impressions of 0.15 mm.

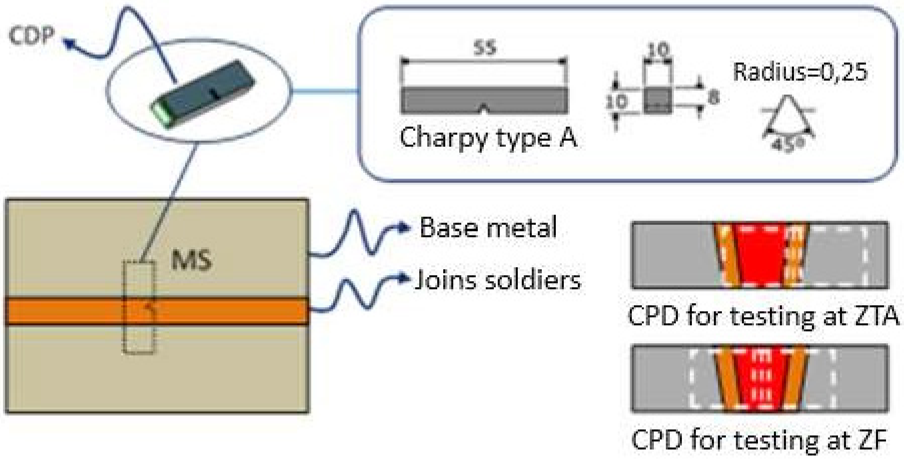

Figure 6. Representation of the specimen for the Charpy type A impact test with their respective dimensions taken from the welded material in the laser process and from the joins soldiers.

Source: Prepared by the authors, 2021.

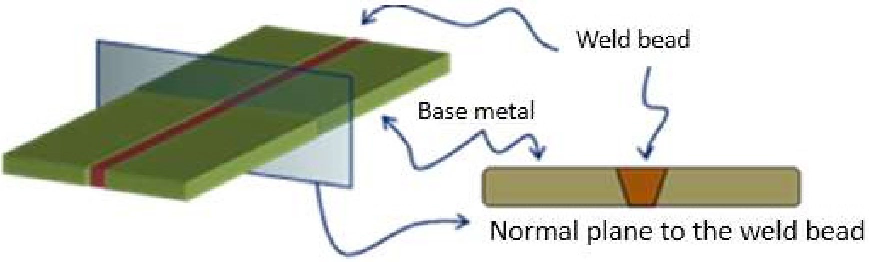

Figure 7. Representation of the planes for obtaining the Vikers hardness in the welded specimen

Source: Prepared by the authors, 2021.

4. Results

This chapter describes the experimental results obtained from the techniques seen in item 3 for destructive (tensile and Charpy A) and non-destructive (metallographic, hardness and Vickers microhardness) tests.

5. Discussion

5.1 Metallographic Test

For the macrograph verification of the welds, (Figure 8), it is verified that the width of the zone is affected by the heat-affected zone (ZAC) varies a lot: it is smaller in the root region and larger in the intermediate region (half the thickness). It is plausible that this is associated with differences in cooling rates across thickness and, as a result, differences in microstructure and hardness.

In Figure 9, there is a micrograph of the welded joint at a magnification of 50 x, where the appearance of the weld in the regions of the base metal, heat-affected zone(ZAC) and molten zone is observed. Visual inspection of the section shows the presence of porosity.

In the micrograph of Figure 10, the ferrite-pearlite microstructure, characteristic of 1020 steel, can be seen. The molten zone is also more clearly observed, indicated by point (A) and characterized by the presence of larger grains, heat-affected zone (ZAC), indicated by (B) and the base metal, region indicated by point (C), not affected by the high temperature in the welding process.

5.2 Hardness Test

Due to the variation in the width of the welding profile verified in Figure 8, three hardness profiles were made, parallel to the plate surface and at different depths. As the penetration of the welds was around 7 mm, the profiles were made at the following distances measured from the surface of the sheet: 1 mm; 3.5mm and 6mm.

The hardness profiles included 3 measurement points in the molten zone and the other 6 or 7 remaining in the heat-affected zone (ZAC), and base metal, as shown in Figure 11. The values are presented in Table 2, in which the zones in which the hardness are located base metal, heat-affected zone, and steel melt zone are identified.

DOI: https://doi.org/10.30564/jmer.v4i2.3381

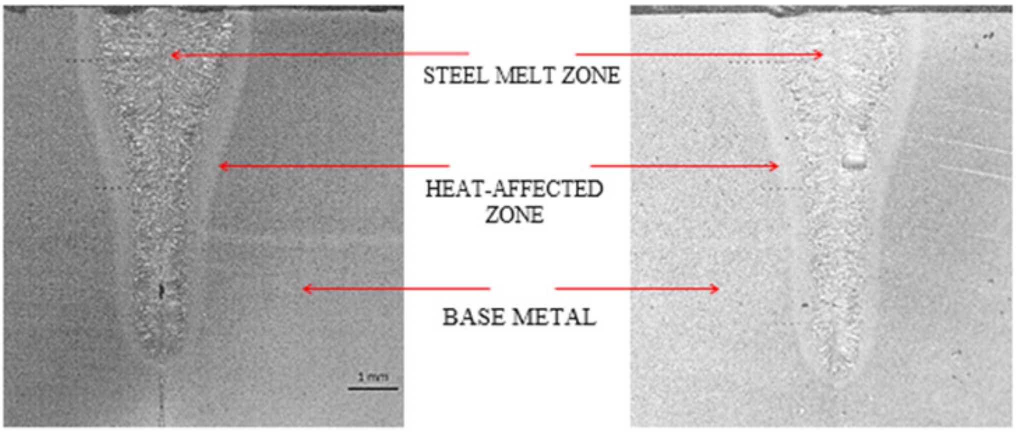

Figure 8. Macrographs of the cross sections of the welds performed with: a) low energy; b) high energy.

Source: Prepared by the authors, 2021.

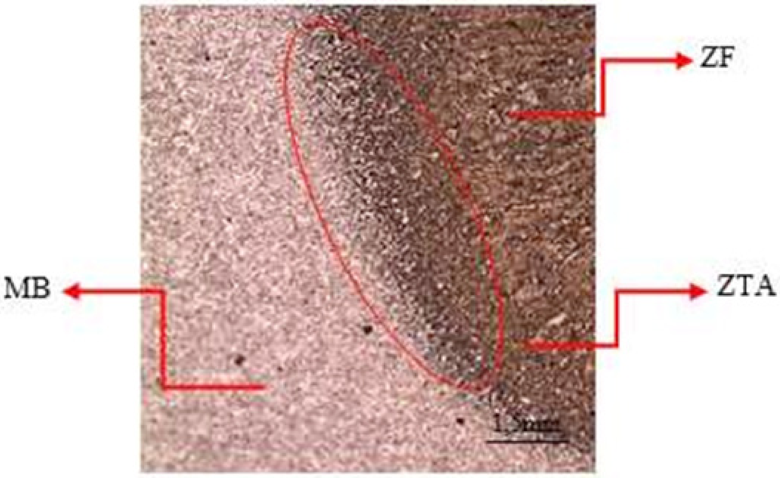

Figure 9. Micrograph of the welded joint at 50x magnification

Source: Prepared by the authors, 2021.

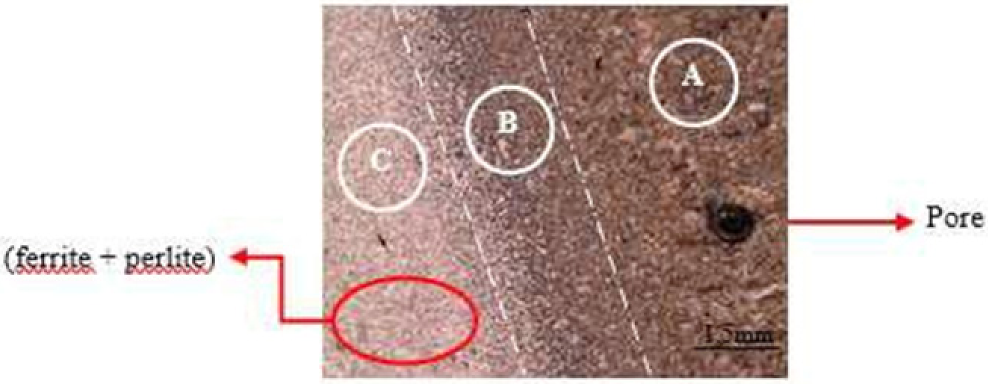

Figure 10. Micrograph of the welded joint at 50x magnification

Source: Prepared by the authors, 2021.

DOI: https://doi.org/10.30564/jmer.v4i2.3381

Table 2. Values of microhardness of the welded joint profile in which the hardness zones located base metal, heat-affected zone, and steel melt zone are identified.

Region	Average Hardness (HV) Face profile	Region	Average Hardness (HV) Intermediate profile	Region	Average Hardness (HV) Root profile
Base metal	161	Base metal	180	Base metal	195
Heat-affected zone	234,6	Heat-affected zone	238,8	Heat-affected zone	314
Steel melting zone	324,2	Steel melting zone	332,7	Steel melting zone	405,7

Source: Prepared by the authors, 2021.

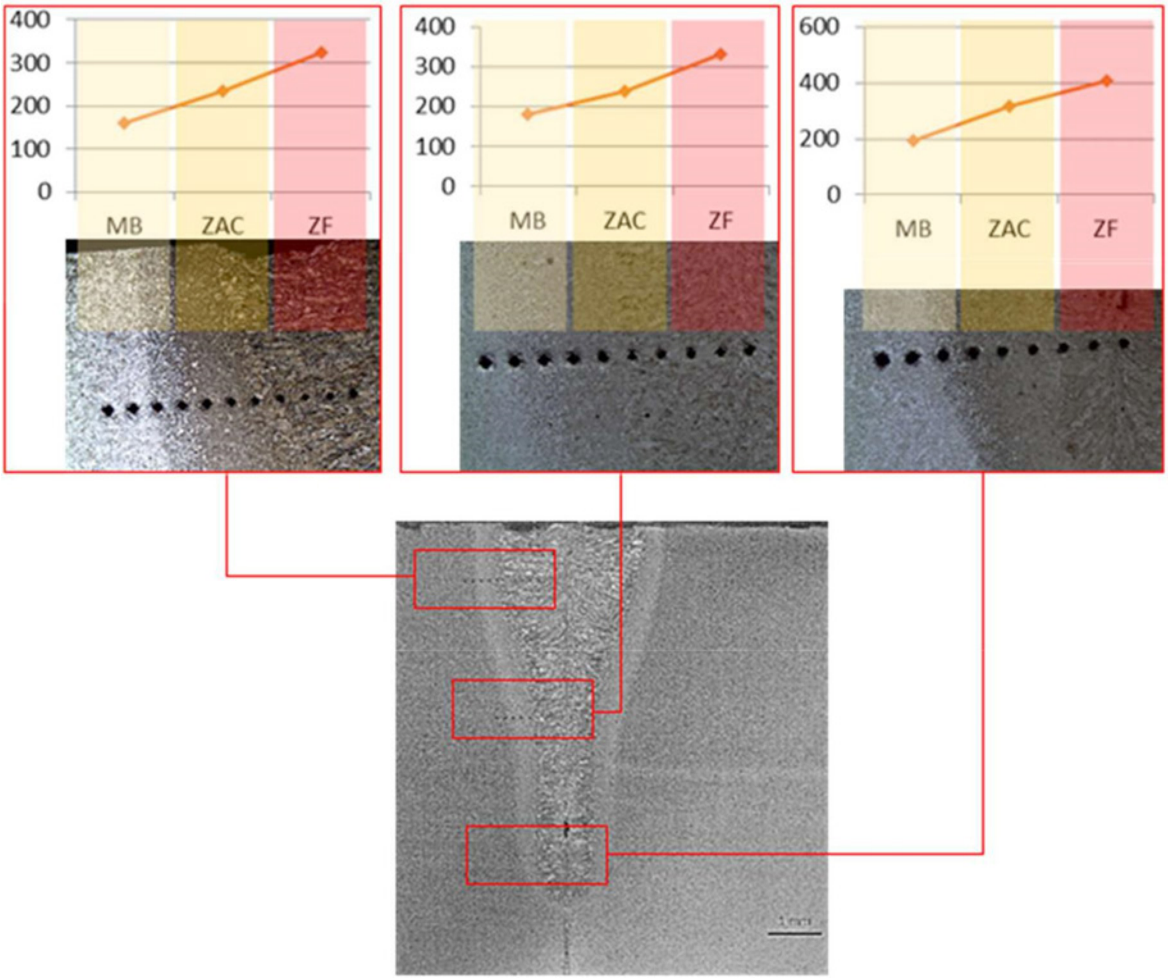

Figure 11. Representation of the hardness profiles carried out, with the identification points to determine the Vikers microhardness profile with the average of three points at three levels for the base metal, Thermally Affected Zone (ZTA) and molten zone.

Source: Prepared by the authors, 2021.

Regarding the verification of a relatively lower hardness of MB, the result was already expected because it is 1020 steel, but in heat-affected zone (ZAC), there was a high increase, due to the possible formation of martensite. In other words, even though the material has low hardenability, the high cooling rates resulting from the use of the laser promoted the formation of martensite.

5.3 Charpy Impact Test

The major result of the Charpy test is the energy needed to deform and fracture the specimen, called the global energy, which is read directly on the machine's gauge. This energy corresponds to the difference in potential energy of the pendulum hammer before and after the impact. The results got from absorbed energy as a function of temperature and brittleness index for the specimens can be seen in Table 3.

Table 3. Values of energy absorbed in the impact test for the 3 samples.

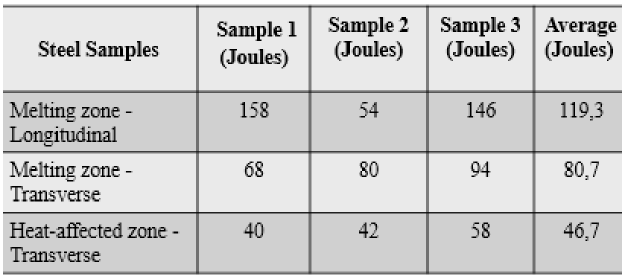

Steel Samples	Sample 1 (Joules)	Sample 2 (Joules)	Sample 3 (Joules)	Average (Joules)
Melting zone - Longitudinal	158	54	146	119,3
Melting zone - Transverse	68	80	94	80,7
Heat-affected zone - Transverse	40	42	58	46,7

Source: Prepared by the authors, 2021.

First, the surfaces of the samples tested differed according to the fracture mode, comparing the longitudinal fracture specimens and the transversal weld fracture specimens (Figure 12). For steel specimens with fracture initiated by the melting zone, the fracture occurred irregularly, featuring a triaxiality of tensions, while those fractured in the heat-affected zone (ZAC), transversely to the weld showed a surface with greater flatness. The results verified in Table 3 also reveal a very strong divergence of values (more than 60%).

It is observed that in the heat-affected zone (ZAC) region, compared to the other regions, lower values of impact energy were recorded due to microstructural changes caused by the thermal cycle in welding. This thermal cycle leads to a heat-affected zone (ZAC), with the possible presence of martensite in the microstructure, resulting in lower fracture toughness. This fact, together with the discontinuity and porosities in the welding, corroborates the fact that the impact energy is lower in the transverse heat-affected zone (ZAC).

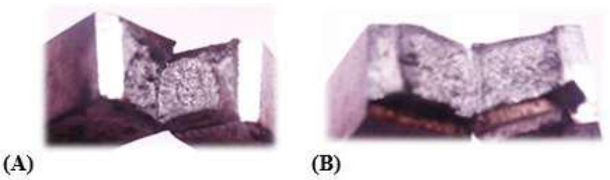

Figure 12. Comparative fracture images between a Charpy impact steel specimens. for longitudinal steel melt zone with pronounced irregularity on the fractured surface (A) and transverse heat-affected zone (ZAC), with a surface with greater flatness.

Source: Prepared by the authors, 2021.

5.4 Tensile Test

In the tensile test made for the base metal according to ASTM A370-10 [10] standard, although the extracted specimens are aligned in the rolling direction, the results of the values of the yield limit, rupture limit, maximum stress, and elongation, can be seen in Table 4.

The test specimens for the weld joints were not successful in the test, given the rupture in the weld region. This behavior is due to the welding failures found in the beads, causing a decrease in area and stress concentration, as well as the possible formation of embrittlement micro-constituents such as martensite arising from the cooling process of the bead.

Table 4. Yield limit, rupture limit, maximum stress and elongation values in the tensile test for the base metal and welded joint.

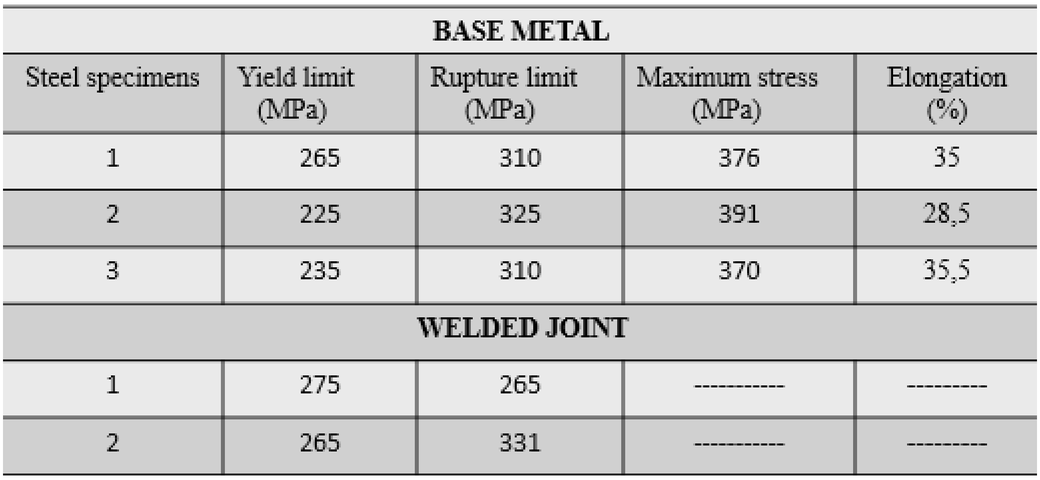

BASE METAL				
Steel specimens	Yield limit (MPa)	Rupture limit (MPa)	Maximum stress (MPa)	Elongation (%)
1	265	310	376	35
2	225	325	391	28,5
3	235	310	370	35,5
WELDED JOINT				
1	275	265	-----------	---------
2	265	331	-----------	---------

Source: Prepared by the authors, 2021.

5. Conclusions

The “tests made from the parameters chosen in the autogenous laser welding of SAE 1020 steel with a thickness of 3/8”, using a 10 kW IPG fiber laser model YLS-10000 at a speed of 2.4 m/min and focus - 6 mm was a priori satisfactory in external aspect. The experimental adjustments, compared with the literature of tests carried out with the same steel, with the same thickness, and with the same equipment, tended to make the process repeatable. However, when analyzing the cross-sections of the samples, discontinuities, porosities, lack of welding, geometric variations in the weald profile along with the depth, and significant microstructural changes were also verified in the mechanical tests. These deleterious defects led to the failure of those welded specimens submitted to the tensile test that broke in the joint, disqualifying the process, seen in Table 4.

The increase in hardness in the heat-affected zone (ZAC) in over 75% in the intermediate part of the weld in relation to base metal indicates the possibility of martensitic formation in this region, even though it is low carbon steel. This possibility is even more emphasized when compared to the Charpy impact energy in this region with an average of 46.6 J in the transverse heat-affected zone (ZAC), seen in Table 3.

One aspect that can be associated with variations in hardness and toughness and consequently with microstructural modifications is the large geometric variation in the weld profile seen in Figure 8, showing a variation in cooling rates along with the profile, which allows for microstructural change.

The low speed associated with the low power can influence the verified porosity and discontinuity (not forming the keyhole in the entire thickness of the plate).

This indicates that for a safe welding process with repeatable results, there may be other conditions with sensitive implications for the last quality. This influence can be verified not only in the equipment process parameters but also in the dimensional characteristics of the parts themselves (joint linearity, thickness) and their fastenings (joint alignment), as well as the welded regions of the parts given the thermal flow with relation to mass and conductivity to the environment.

References

[1] MAIMAN, T.H. Simulated optical radiation in ruby. Nature, v. 187, p. 493-494, 1960.

[2] STEEN, W. M. Laser material processing, SpringerVerlag, ISBN 1852336986. 2005.

[3] MENDEZ, P. F.; EAGAR, T. W. Penetration and defect formation in high-current arc welding. Welding Journal, p. 296- 306, 2003.

[4] LEIDINGER, D., et al. Improved manufacturing processes with high power lasers. Infrared Phys. Technol. vol. 36, No. 1, Great Britain, 251-266 p ,1995.

[5] LADARIO, P. F et.al A study of the laser welding process of automotive blanks, with and without coating, in the industrial environment aiming at incremental improvements and cost reduction. Pág. 02, 2009.

[6] CARVALHO S. M. Study of laser and TIG weldability of commercially pure grade 2 titanium used in aircraft pneumatic systems. Thesis - USP, Lorena, Brazil,2012.

[7] SAUCEDO, F. V., et al. Industrial Laser solutions for manufacturing, 2016. [Online]. Disponível em: [Acesso em: 10- Out-2016].

[8] BELFORTE, D. Tailor blank welding in Europe. Industrial Laser Solutions, USA, v. March, 2002.

[9] HITZ, C. B., EWING, J. J., HECHT J. Introduction to Laser Technology. 4. ed. Piscataway: Wiley-IEEE Press, 2012. 312 p.

[10] ABNT-Brazilian Association of Technical Standards - NBR NM-87-2000 - Carbon Steel and Alloys for Mechanical Construction - Designation and chemical composition. Available in: https://vdocuments.com.br/nbr-nm-87-2000-aco-carbono-e-ligados-para-construcao-mecanica-designacao.html.

[11] BUEHLER SUM-MET - The Science Behind Materials Preparation. ISBN 0-9752898-0-2, 2004.

[12] ASTM A370-10. Standard Test Methods and Definitions for Mechanical Testing of Steel Products. Available in: https://www.astm.org/Standards/A370.htm.

[13] API Standard 1104, 21st Edition is the industry standard for welding practices. Available in: https://pdfcoffee.com/api-1104-05bilinguecorpo-da-norma-pdf-free.html.

[14] A370-20 Standard Test Methods and Definitions for Mechanical Testing of Steel Products yield - Tension test - Charpy impact test/ Izod. Available in: https://www.astm.org/DATABASE.CART/HISTORICAL/A370-17.htm.

[15] ASTM E92-82 - Standard Test Method for Vickers Hardness of Metallic Materials. Available in: https://www.astm.org/Standards/E92.htm.

DOI: https://doi.org/10.30564/jmer.v4i2.3381

BILINGUAL PUBLISHING CO.
Pioneer of Global Academics Since 1984

Journal of Mechanical Engineering Research
https://ojs.bilpublishing.com/index.php/jmer

ARTICLE

Conception the Fluid Flow Behavior within Oil Reservoir Rock by Using Computed Tomography (CT) Scan

Amani J. Majeed[1*] **Falah A Abood**[2] **Ahmed K. Alshara**[3]

1. Petroleum Engineering Department, University of Basrah, Iraq
2. Mechanical Engineering Department, University of Basrah, Iraq
3. Mechanical Engineering Department, University of Misan, Iraq

ARTICLE INFO

Article history
Received: 3 May 2021
Accepted: 2 June 2021

Keywords:
Computed Tomography (CT) scan
Al-Nour field
Fluid flow

ABSTRACT

The behavior of fluid flow has been studied during the different flow media over the past decades. In addition, the behavior of the flow of fluid through porous media has garnered much research interest. This paper sheds light on fissured rocks of oil reservoir media (as one of the porous media domain), and the effect of these fissured on fluid flow. In this article, the Finite Volume Method (FVM) has been used to visualize the behavior of single-phase fluid flow in an actual core according to the dual-porosity dual permeability model. The study was conducted in two parts, the first was the image processing for one of the real oil reservoir fractured rock images, where the image was processed and simulated by ANSYS-CFX software, and the results showed a complete visualizing of the fluid behavior during this domain. As for the other side, a simulation of a real reservoir rock belonging to the Al-Nour field in Iraq / Misan was made. The X-ray Computed Tomography (CT) scan has been used to convert the real fractured core to a dynamic domain. ANSYS-CFX program has been used and the results illustrated the pressure counter, the velocity counter, the velocity streamline, and the velocity vectors for the studied model in three dimensions. A comparison was made between the productivity index for fractured and non-fractured rock and the results explained that the presence of fracture can improve the productivity index to about 5.74%.

1. Introduction

Natural fractures are found in almost all petroleum reservoirs. These structures are difficult in their characterization and predictor. Representing the fluid flow behavior in a naturally fractured reservoir is very complex because of the complex nature of these domains. This topic took the attention of both engineers and geologists [1-3]. Two media could be recognized in this type of reservoir; fracture media and matrix media. The fracture and matrix are different in their porosity and permeability. The effect of the fracture and fracture permeability on the flow of fluid has been notarized by many studies, where these fissures may act as a barriers system, conduits system, or combined (conduit-barrier) systems [4,5]. A comprehensive study of the effect of fractures on the fluid flow within the subsurface has been given by scientists [6-12]. In 1990, Luthi and Souhait, performed 3D finite element models to investigate the response to fissures of the Formation Micro-Scanner, where a high resolution

---

**Corresponding Author:*
Amani J. Majeed
Petroleum Engineering Department, University of Basrah, Iraq;
Email: Amani.majeed@uobasrah.edu.iq

DOI: https://doi.org/10.30564/jmer.v4i2.3194

has been recorded for electrical scans for the borehole wall according to fissures. The detected, traced, and quantified fissures were the 3-steps that they used in their model. In the detection step, they used the Formation Micro-Scanner images for the locations that possibly had fissures, so when the electric conductivity overrides the local conductivity of the matrix by a statistically considerable amount the fracture locations are detected. After that, they performed an integration around these locations over a circular zone to gather all excessive currents; then the integral reduced to approximate the line integral. The trace step has been done by a line sharpening and neighbor connectivity tests then the apertures are computed for whole fissure locations. From the obtained results, they showed that their method successfully traces fractures, and their technique was novel and unique for characterizing fissures in wellbores [13]. In 2003, Hirono et. al, used the n X-ray computed tomography (CT) imaging method to visualize the behavior of fluid during the permeability testing. Moreover, along the permeable zone, they measured the localized permeabilities [14]. In 2007, Karpyn et. al., studied the fissures' effect on the two-phase flow of fluid (oil and water), and they used micro-computed tomography (MCT) to distinguish the internal structure of the fracture.

The focus of this research was on visualizing the flow inside the fractures differently, as several programs were used to obtain a comprehensive visualization of a single-phase fluid flow in these media. Moreover, the X-ray Computed Tomography (CT) scan has been used to convert the real fractured core (the core that was taken from the Al-Nour field in Iraq / Misan) to a dynamic domain, where several programs have been used to get a three-dimensional dynamic domain for the mentioned core.

2. Methodology

The behavior of fluid flow through a fracture profile in a permeable rock in an actual reservoir core, shown in Figure 1, according to dual-porosity-dual-permeability (DPDP) model has been performed numerically in this study. The study falls into two domains; the first one represents the simulation of a natural fracture picture, as shown in Figure 2. While the second one represents the simulation of the real fractured core. Where, the X-ray

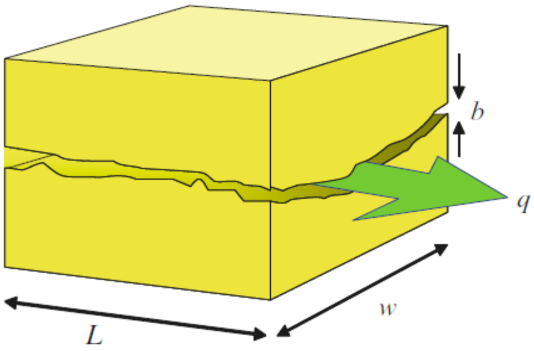

Figure 1. Flow in actual fracture

Figure 2. Fractures and Matrices. [16]

DOI: https://doi.org/10.30564/jmer.v4i2.3194

Computed Tomography (CT) scan was used to get a 3D picture of the real fractured core, as illustrated in Figure 3. This image was subjected to a series of software operations to be converted from a static model that can't be simulated, into a dynamic model that can be simulated. Figure 4 shows the chart for the series of programs used in image processing.

Two media could be recognized in this type of rock; fracture media and matrix media. The general form of mass balance equations can be given as [17,18];

- The mass balance equation for the fluid flow in the matrix system is given by the following equation

$$\frac{\partial \emptyset^m s^m}{\partial t} + \nabla \cdot \boldsymbol{u}^m = q^{f-m} + \psi^m \qquad (1)$$

where the phase fluxes in matrix ($\mathrm{u^m}$) is given by:

$$\boldsymbol{u}^m = -\frac{K_r^m K^m}{\mu}\left[\nabla P^m - \rho\, g\right] \qquad (2)$$

- The mass balance equation for the fluid flow in the fracture system is given by the following equation:

$$\frac{\partial \emptyset^f s^f}{\partial t} + \nabla \cdot \boldsymbol{u}^f = q^{m-f} + \psi^f \qquad (3)$$

where the phase fluxes in fracture ($\boldsymbol{u}^f$) is given by:

$$\boldsymbol{u}^f = -\frac{K_r^f K^f}{\mu}\left[\nabla P^f - \rho\, g\right] \qquad (4)$$

Where, $\emptyset$ is the porosity, s is the phase saturation, q is the volumetric flux, ψ is the volumetric source, Kr is a relative permeability, and the superscripts; f and m denote to the parameters which defined in fracture and matrix domains, respectively.

Moreover, the general form of a momentum conservation equation (Navier-Stokes equation) can be given as [19];

$$\rho\,\frac{D\,\boldsymbol{u}}{Dt} = -\ \nabla P - \mu\,\frac{\boldsymbol{u}}{k} + \mu_{eff}\,\nabla^2\,\boldsymbol{u} \qquad (5)$$

Where;

$$\mu \ \approx\ \mu_{eff} \qquad \textit{For large value of } k$$

Darcy introduced an equation for the mean filter velocity $\boldsymbol{u}$ for the fluid flow through a homogeneous porous media field with absolute permeability k, a viscosity of the fluid μ, and pressure gradient across the domain ∇P:

$$u = -\ \frac{k}{\mu}\,(\nabla P - \rho g) \qquad (6)$$

where

g = The acceleration due to the gravitational forces, which can be neglected for a horizontal layer flow (ft/s^2).

ρ= The density of the fluid (Ib/ft^3).

The mean filter velocity in Equation (3.7), is also called Darcy velocity, which is related to the average pore velocity u_p by the relation [20]:

$$\mathrm{u} = \ \emptyset\, \mathrm{u_p} \qquad (7)$$

Where $\emptyset$ is the effective porosity of the porous media.

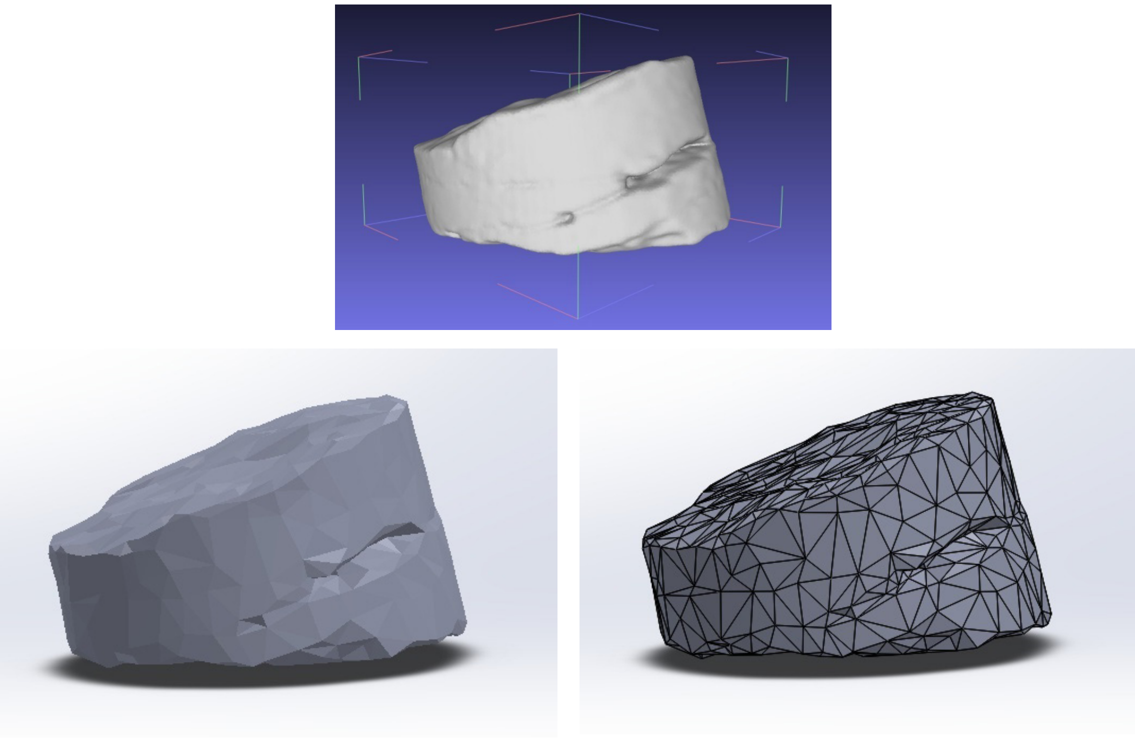

Figure 3. Actual Fractured core.

DOI: https://doi.org/10.30564/jmer.v4i2.3194

$$k_f = \frac{h_{avg}^2}{12} \tag{8}$$

Where h_{avg} is an average value for h_i, which can be calculated from the following:

$$h_{avg} = \frac{\sum_{i=1}^{n} h_i}{n} \tag{9}$$

For the single-phase flow conditions, the productivity index (*J*) defined as the relationship between flow rate and the pressure drawdown, the difference between a given average reservoir pressure and the bottom-hole flowing pressure:

$$J = \frac{q_o}{\bar{P}_R - P_{wf}} \tag{10}$$

Where; q_o is the oil flow rate, $\bar{P}_R$ the average reservoir pressure, and P_{wf} is the bottomhole pressure.

The parameters boundary conditions are; Fluid density = 49.94 Ib/ft^3 (0.8 g/cm^3), Fluid viscosity = 0.00010443 lbf s ft^{-2} (5 cp), The total pressure inlet = 3000 psi (2.068E7 Pa), No- slip wall conditions, and homogenous domain have been assumed.

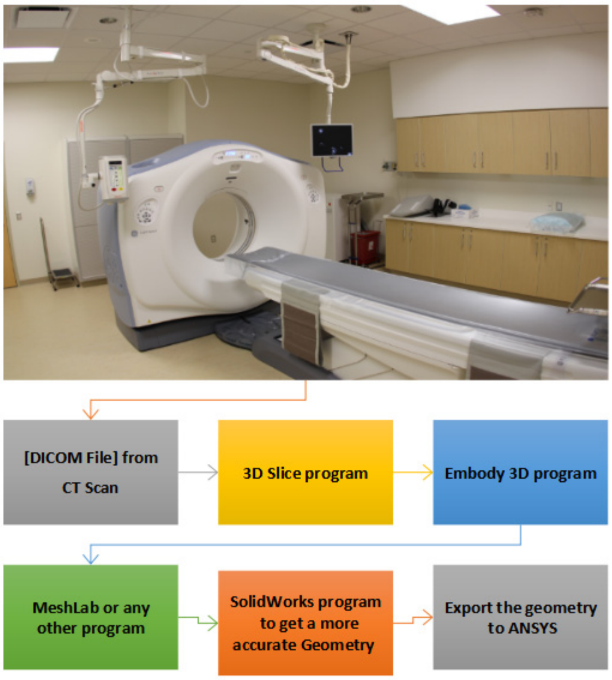

Figure 4. The CT-scan image transition.

3. Results and Discussion

The single-phase fluid flow is presupposed to be laminar and follow Darcy's Law. Moreover, the EbFV approach has been used in the analysis and the results in detail have been explained. The X-ray Computed Tomography (CT) scan was used to convert the actual rock domain to a dynamic picture domain, to make it suitable for simulating by the ANSYS-CFX program.

Figure 5-A represents the real image from which the measurements of the fracture were taken. While Figure 5-B represents the computational domain that corresponds to this image that was executed in the ANSYS program, CFX package. The average fracture apertures have been calculated in this model, where it is approximately (1.42 cm), which in turn can be used to calculate the permeability of fracture by using Equation 8.

Figure 6 shows the pressure contour throughout the computational domain where pressure gradient can be observed through the domain as a whole, in addition, to illustrate the pressure distribution through the fractured area.

Figure 7 illustrates the velocity contour throughout the computational domain. A rapid velocity increase in the fractured zone can be observed, which is attributed to its high permeability when compared to the permeability of the surrounding rock. Where the average velocity in the fracture is (0.007151 m/s, Re = 16.13), while the average velocity in the matrix is (0.00008143 m/s).

Figure 8 and Figure 9, visualize the velocity streamline and the velocity vectors throughout the computational domain, respectively, under (1000 psi) pressure drop and with fracture permeability equal to (0.0000168 m^2). Where the velocity streamline can be followed throughout the domain to move from the areas of high pressure to low pressure, in addition to the distribution within the fractured zone. The incoming velocity vectors to the fractured zone have been enlarged to give further indication of intensified fluid movement in this area.

On the other hand, the simulation of a real rock model (with 10.5 cm in diameter and 5.5 cm in length) obtained from the Misan Field, Bin Umar formation, at a depth (3688 m) was done. The tomography scan has been taken to the rock by using a CT scan device belonging to Al-Fayhaa Hospital, where a total of CT scan pictures have been obtained and several programs were treated so that the geometry could be converted into a 3D dynamic domain that could be simulated by ANSYS. These processes would convert the geometrical form of a static model into a dynamic model that can be manipulated with engineering programs and undergone the boundary conditions that are related to a special issue, as shown in Figure 10. The average fracture aperture is about (1.9054 cm). Here also the Equation (8) could be used to calculate the permeability of the fracture.

Figure 11 displays the pressure contour and the velocity contour if it is presumed that the rock without any fracture. Where the pressure drop during the rock is 1000

DOI: https://doi.org/10.30564/jmer.v4i2.3194

psi, while the average velocity on the outlet approximately (0.0001538 m/s). The velocity streamlines and the velocity vectors of the fluid during the non-fractured rock are depicted in Figure 12.

The pressure contour and the velocity contour of fractured rock illustrate in Figure 13. Obviously, the presence of a small fracture can contribute to raising the rate of fluid velocity where the average velocity of the outflow fluid reaches about (0.000162467 m/s). The difference in the pressure contour lines in both the fractured and non-cracked rock is illustrated in Figure 15, where the pressure lines are distributed clearly in

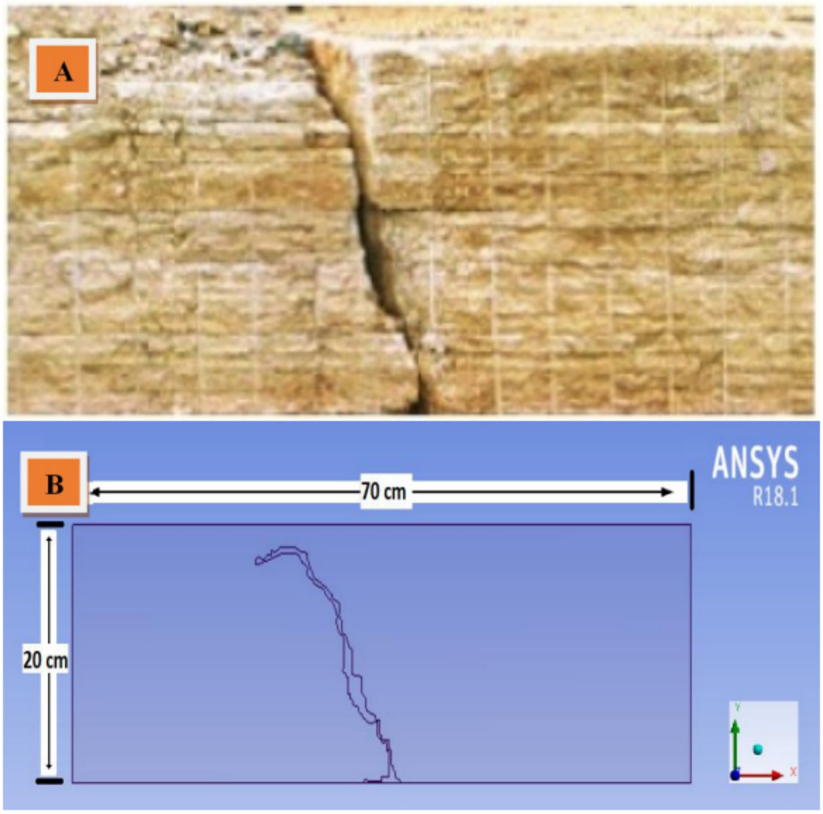

Figure 5. (A) Real fractured rock image, (B) The domain that has been designed by ANSYS program

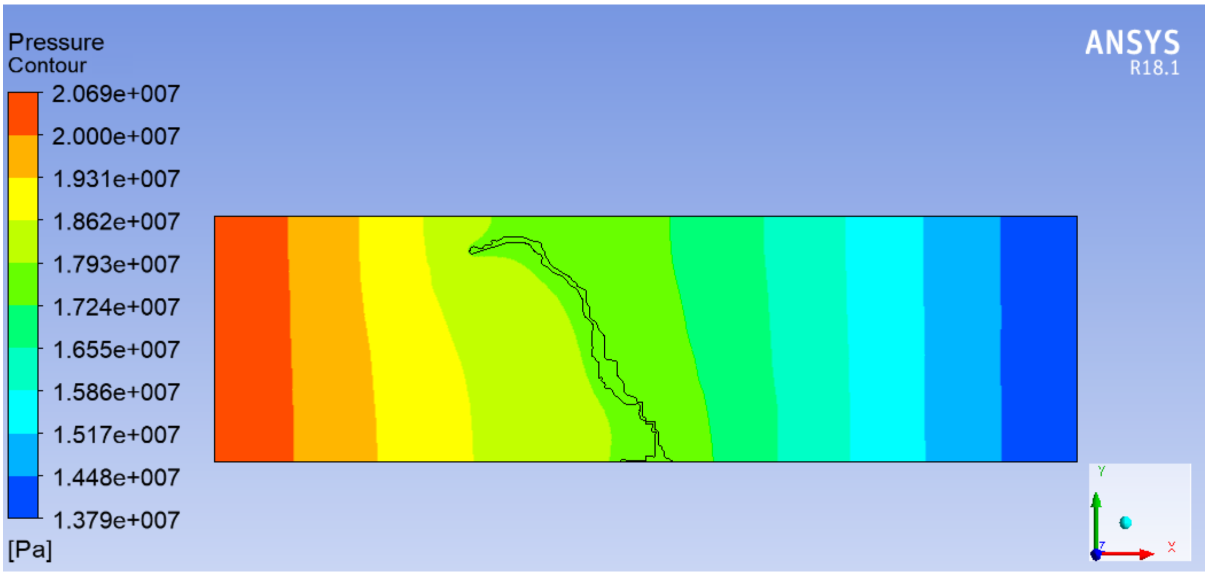

Figure 6. The Global pressure contour throughout the domain

DOI: https://doi.org/10.30564/jmer.v4i2.3194

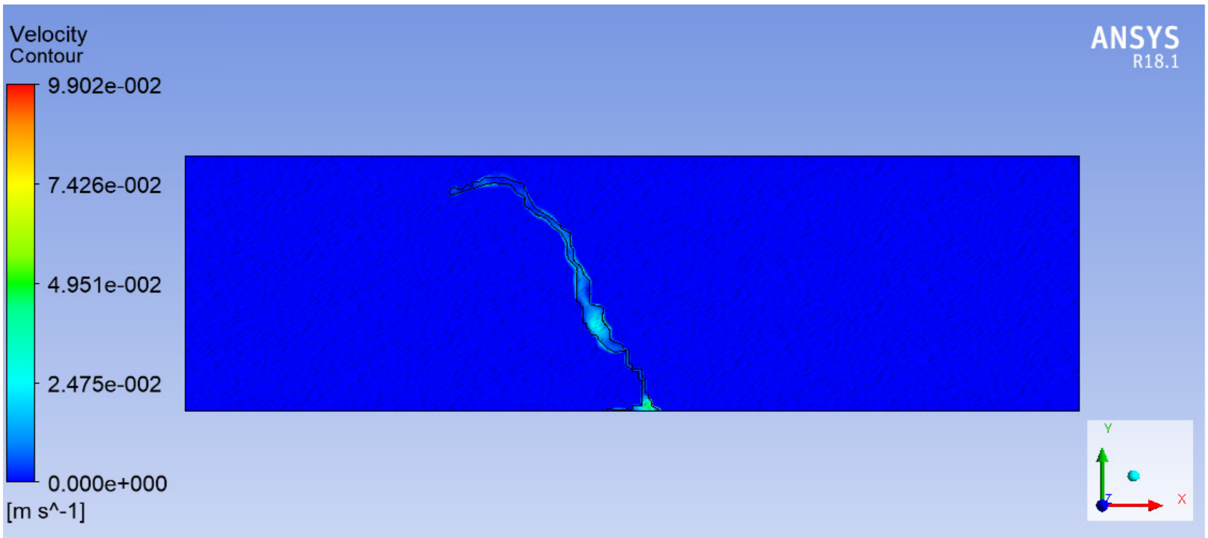

Figure 7. The velocity contour throughout the domain.

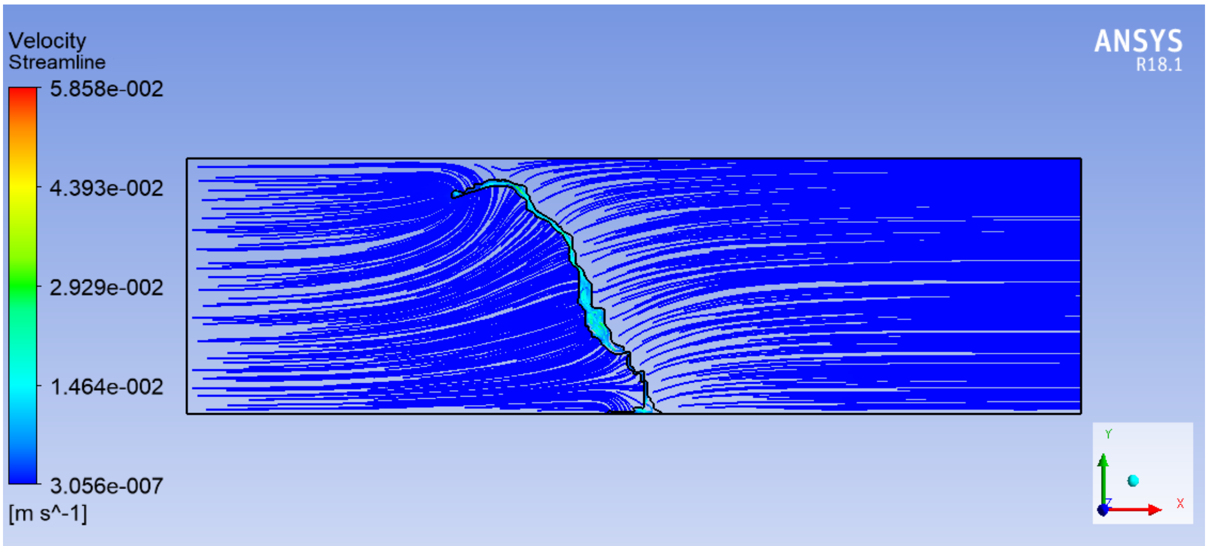

Figure 8. The velocity streamline throughout the domain.

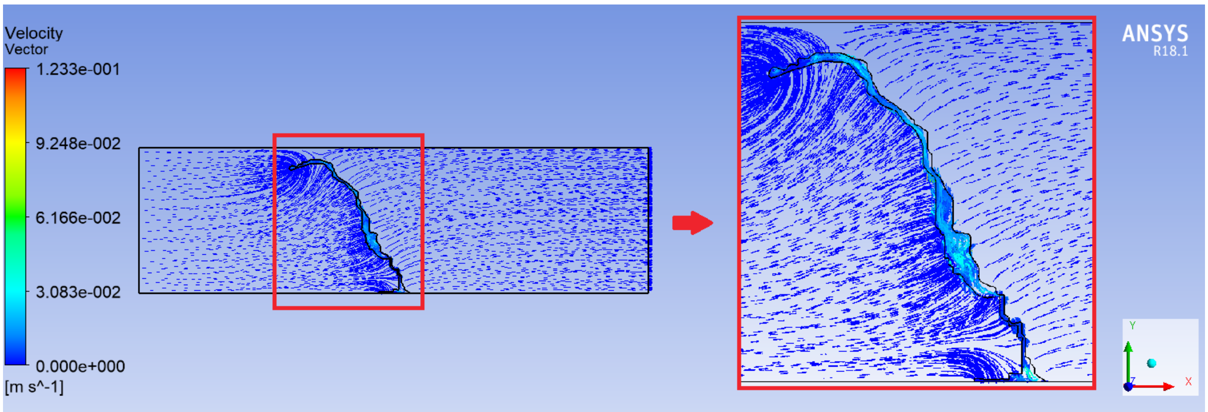

Figure 9. The velocity vectors throughout the domain.

DOI: https://doi.org/10.30564/jmer.v4i2.3194

both cases. In the absence of a fracture, the pressure distribution will be uniform to all layers of the rock from the high-pressure area to the low-pressure zone. In the case of fractured rock, the pressure will decrease at all sides of the fracture faster than adjacent layers. This is due to the high permeability of the fracture when compared with the matrix.

The velocity streamlines and the velocity vectors of the fluid over the fractured rock are depicted in Figure 14, where an increase in fluid velocity can be observed in the fracture zone, this is a reasonable behavior as the fluid would be attracted to the areas with high permeability. A comparison was made between the productivity index for fractured and non-fractured rock and the results explained that the presence of fracture can improve the productivity index to about 5.74%.

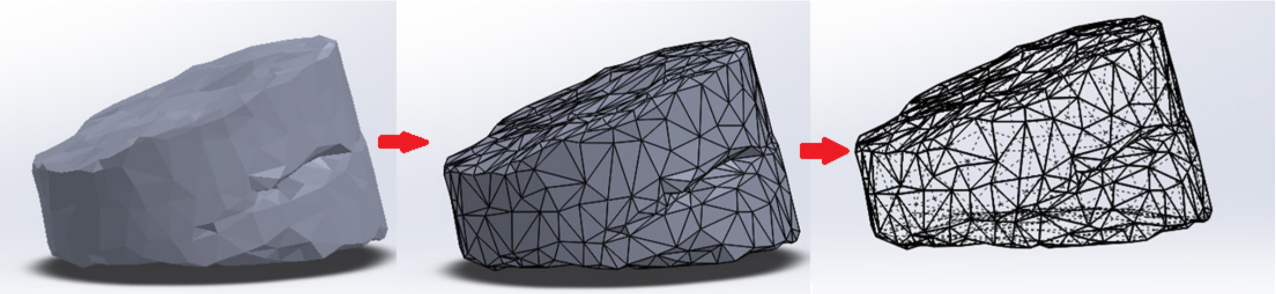

Figure 10. Converting static geometry to dynamic geometry.

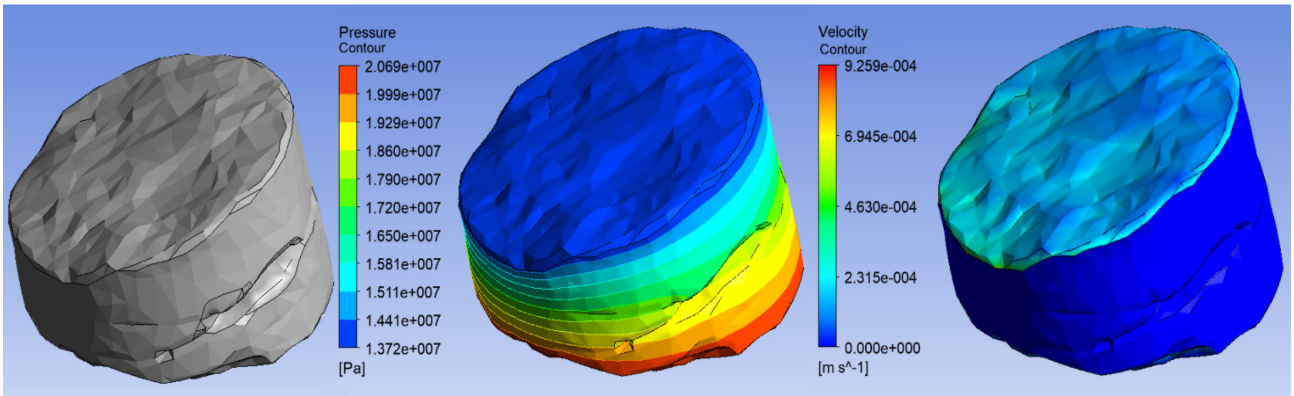

Figure 11. The pressure contour and velocity contour throughout the non-fractured rock

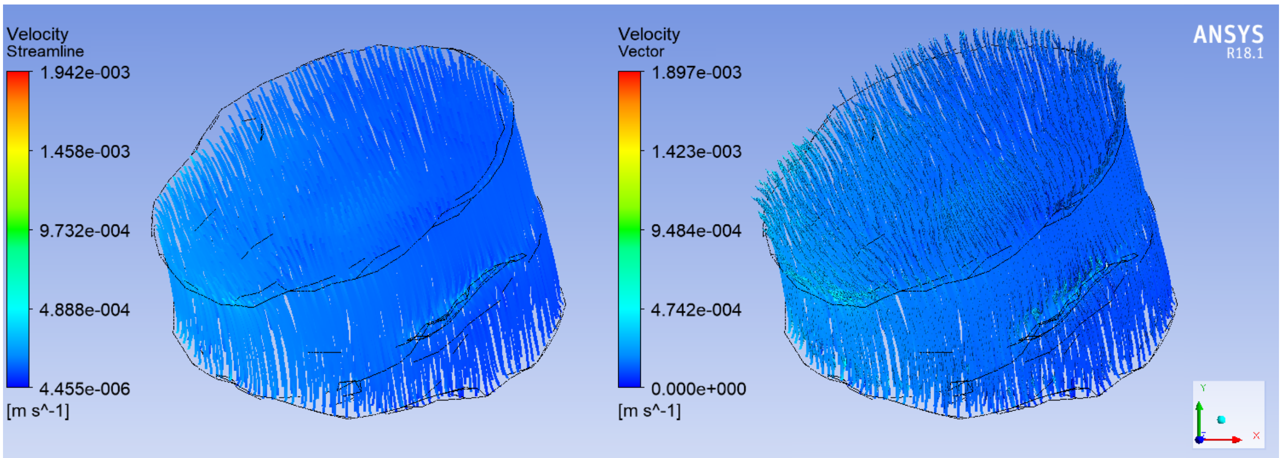

Figure 12. The velocity streamlines and the velocity vector throughout the non-fractured rock.

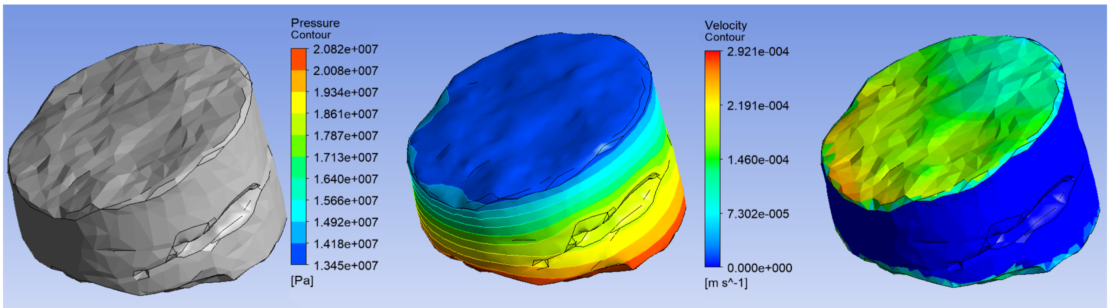

Figure 13. The pressure contour and velocity contour throughout the fractured rock.

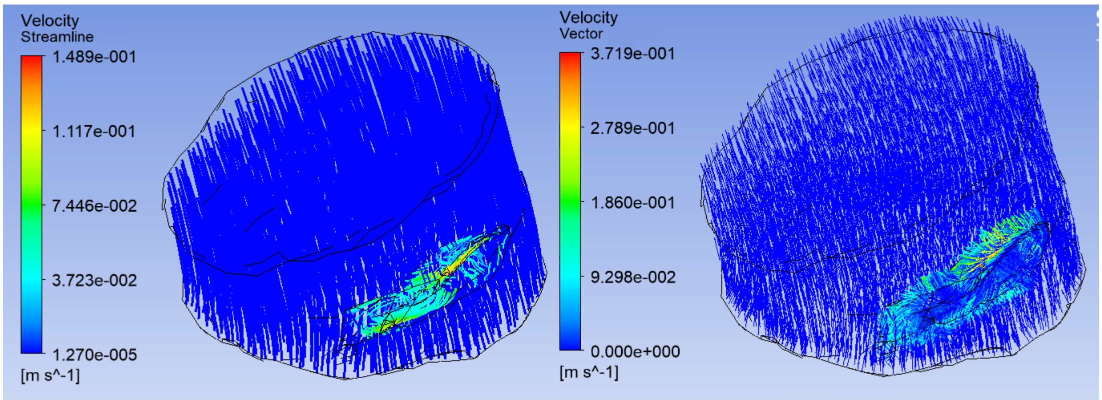

Figure 14. The velocity streamlines and the velocity vector throughout the fractured rock.

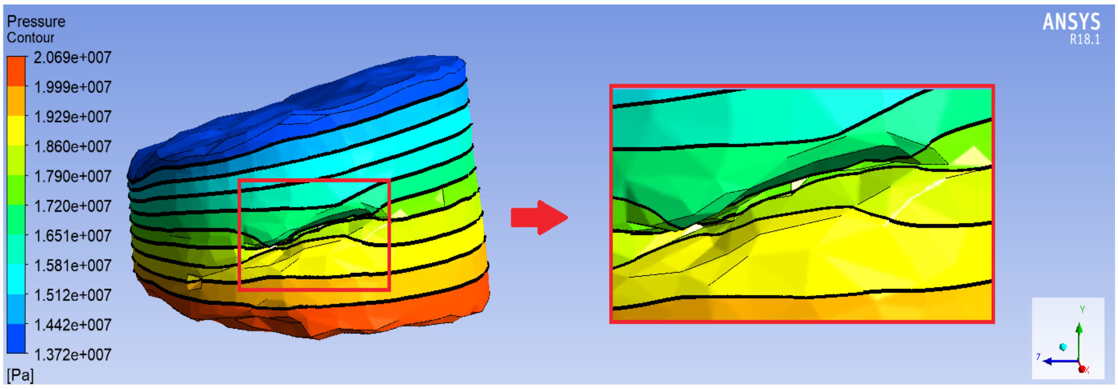

A) Non-Fractured Rock

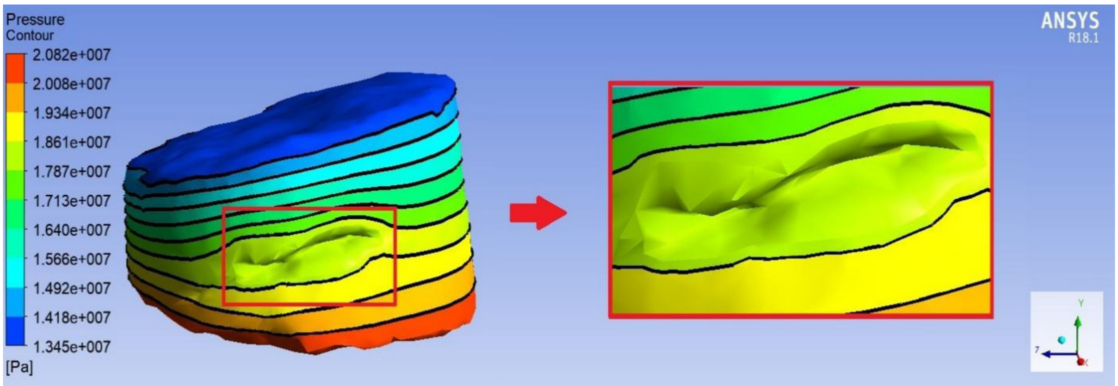

B) Fractured Rock

Figure 15. The pressure contour of the rock.

DOI: https://doi.org/10.30564/jmer.v4i2.3194

4. Conclusions

The numerical simulation for single-phase and laminar flow of fluid within fractured rock has been conducted in this study. The X-ray Computed Tomography (CT) imaging was successfully applied. However, the resulting images from the CT scan have been treated with several programs to get a three-dimensional dynamic domain. The three-dimension for fluid behavior in a rock has been illustrated. Moreover, the X-ray Computed Tomography (CT) imaging helped to diagnosis the fracture within the rock with high resolution and the behavior of fluid within the fracture has been visualized in detail. The results of this study explained that the presence of fracture can improve the productivity index to about 5.74%.

References

[1] Tsang, Y.W.: The effect of tortuosity on fluid flow through a single fracture. Water Resour. Res. 20, 1209-1215 (1984).

[2] Poon, C.Y., Sayles, R.S., Jones, T.A.: Surface measurement and fractal characterization of naturally fractured rocks. J. Phys. D. Appl. Phys. 25, 1269-1275 (1992).

[3] Al-Yaarubi, A.H., Pain, C.C., Grattoni, C.A., Zimmerman, R.W.: Navier-Stokes simulations of fluid flow through a rock fracture. In: Faybishenko, B., Gale, J. (eds.) Dynamics of fluids and transport in fractured rocks, vol. 162 of AGU Monograph, pp. 55-64. American Geophysical Union, Washington, DC (2005).

[4] Randolph, L., Johnson, B.: Influence of faults of moderate displacement on groundwater flow in the Hickory Sandstone aquifer in central Texas. Abstracts - Geological Society of America 21, 242 (1989).

[5] Mozley, P.S., Goodwin, K.B.: Patterns of cementation along a Cenozoic normal fault: a record of paleo flow orientations. Geology 23, 539 - 542 (1995).

[6] Barenblatt G., Zheltov I., and Kochina I., ''Basic concepts in the theory of seepage of homogeneous liquids in fissured rocks [strata]'', Journal of applied mathematics and mechanics, Vol. 24, No. 5, pp 1286-1303, 1960.

[7] Odeh A. S., ''Unsteady state behavior of naturally fractured reseroir'', Society of Petroleum Engineers Journal, Vol. 5, No. 1, pp 60-66, March, 1965.

[8] Kazemi H., ''Pressure Transient Analysis of Naturally Fractured Reservoirs with Uniform Fracture Distribution'', Society of Petroleum Engineers Journal, Vol. 9, No. 04, pp 451-462, 1969.

[9] Pickett G. R., and Reynolds E. B., ''Evaluation of fractured reservoir'', Society of Petroleum Engineers Journal, Vol. 9, No. 1, pp 28-38, March 1969.

[10] Abbasi M., Madani M., Shari M., and Kazemi A., "Fluid flow in fractured reservoirs: Exact analytical solution for transient dual porosity model with variable rock matrix block size", Journal of Petoleum Science and Engineering, Vol. 164, pp 571-583, 2018.

[11] Al-Husseini A. J., Abood F. A., Alshara A. K., Hydrodynamics Behaviour of Single and Multi Fracture with Different Orientations in Petroleum Reservoir, Basrah Journal for Engineering Sciences, Vol.19, No.1, pp.12-16, (2019).

[12] Majeed A. J., Alshara A. K., Al-Mukhtar A. M., Abood F. A.: Fracturing Parameters in Petroleum Reservoirs and Simulation. Advances in Material Sciences and Engineering. Pp. 491-8, (2020).

[13] Luthi S. M. and Souhaitet P.: Fracture apertures from electrical borehole scans, Geophysic, Vol. 55, No. 7. pp 821-833, July, (1990).

[14] Hirono, T., Takahashi, M., Nakashima, S.: In situ visualization of fluid flow image within deformed rock by X-ray CT. Eng. Geol. 70, 37-46 (2003).

[15] Karpyn, Z.T., Grader, A.S., Halleck, P.M.: Visualization of fluid occupancy in a rough fracture using micro-tomography. J. Colloid Interface Sci. 307, 181-187 (2007).

[16] Berg, R. R., ''Method for determining permeability from reservoir rock properties''. Transactions Gulf Coast Association of Geological Societies, Vol. 20, pp 303-317, (1970).

[17] Guo B., Tao Y., Bandilla K., and Celia M., "Vertically Integrated Dual-porosity and Dual-permeability Models for CO2 Sequestration in Fractured Geological Formation", Energy Procedia, Vol. 114, pp 3343-3352, Nov., (2017).

[18] Weirong L., Dong Z., and Lei G., "Integrating Embedded Discrete Ffracture and Dual Porosity Method to Simulate Fluid Flow in Shale Oil Reservoir", Energies, Vol. 10, No. 10, (2017).

[19] Hamdan M. H., '' Single-Phase through Porous Channels A Review of Flow Models and Channel Entry Conditions''. Applied Mathematics and Computation Vol. 62, No. 3, pp 203-222, May, 1994.

[20] Rudraiah N., Chandrasekhara B. C., Veerabhadraiah R., and Nagaraj S. T., ''Some Flow Problems in Porous Media'', PGSAM-2, Bangalore University, India, 1979.

NOMENCLATURE

Permeability [Darcy]	k
The phase saturation	s
Average reservoir pressure [psi]	$\overline{P}_R$
Bottom hole pressure [psi]	P_{wf}
Pressure gradient [psi]	∇P
Relative permeability	k_r
Gravity acceleration vector [m/s^2]	g
Phase flux [m/s]	u
Volumetric flux from the matrix domain to the fracture domain [m/s]	$q^{m\text{-}f}$
Volumetric flux from the fracture domain to the matrix domain [m/s]	$q^{f\text{-}m}$
Velocity [m/s]	v
Time [s]	t
Productivity index [BBl/psi Day]	J
Oil flow rate [BBl/Day]	q_o
Greek Letters	
Volumetric source term [m/s]	ψ
Porosity [-]	ϕ
The density of fluid [kg/m^3]	ρ
Dynamic viscosity [Pa. s]	μ
Superscripts	
Fracture	f
Matrix	m

DOI: https://doi.org/10.30564/jmer.v4i2.3194

BILINGUAL PUBLISHING CO.
Pioneer of Global Academics Since 1984

Journal of Mechanical Engineering Research
https://ojs.bilpublishing.com/index.php/jmer

ARTICLE

Recognition Methods of Geometrical Images of Automata Models of Systems in Control Problem

Anton Epifanov*

Institute of precision mechanics and control science of RAS, Rabochaya 24, Saratov, Russia

ARTICLE INFO

Article history
Received: 18 August 2021
Accepted: 23 September 2021
Published Online: 27 September 2021

Keywords:
Discrete deterministic dynamical system
Mathematical model
Automaton
Geometric image of an automaton mapping
Geometric curve
Sequence
Recognition of geometric images of automata

ABSTRACT

The laws of functioning of discrete deterministic dynamical systems are investigated, presented in the form of automata models defined by geometric images. Due to the use of the apparatus of geometric images of automata, developed by V.A. Tverdokhlebov, the analysis of automata models is carried out on the basis of the analysis of mathematical structures represented by geometric curves and numerical sequences. The purpose of present research is to further develop the mathematical apparatus of geometric images of automaton models of systems, including the development of new methods for recognizing automata by their geometric images, given both geometric curves and numerical sequences.

1. Introduction

In the class of discrete deterministic dynamical systems, finite deterministic automatons form the simplest, but rather studied subclass. Advanced methods of analysis, synthesis, recognition, etc. of finite state machines are effectively used in solving applied problems for real systems, the automaton models of which are explicitly specified by tables, matrices, graphs, logical equations, etc. After the introduction by McCulloch and Pitts (1943 [1]) of the basic provisions on which the concept of an automaton is built, the theory of automata was developed in [2-9] and many others etc. The research results presented in the works of these authors constitute the fundamental basis of the symbolic theory of automata, ie. theory, in which automata, as a rule, are not associated with classical numerical structures, which limits the application of the methods of classical mathematics in the automata theory.

In connection with the development of areas of application of the theory of automata, it turned out that for real systems of large dimension, the assignment of automata models with tables, matrices, graphs, and logical equations is practically ineffective. One of the ways to expand the field of application of the theory of automata was the research of Academician of the Russian Academy of Natural Sciences V.A. Tverdokhlebov, in which, since 1993, is considered the representation of the laws of functioning of automata, given by discrete symbolic next state and output functions, by continuous numerical structures.

**Corresponding Author:*
Anton Epifanov,
Institute of precision mechanics and control science of RAS, Rabochaya 24, Saratov, Russia;
Email: epifanovas@list.ru

https://doi.org/10.30564/jmer.v4i2.3588

For this, the automata mapping is assumed to be a set of points with numerical coordinates and the laws of functioning are represented by broken lines, the vertices of which are located on analytically specified curves. This approach to defining of automata as well as some methods of analysis, synthesis and recognition of automata by their geometric images are used and developed.

The geometric approach used in this work to define the laws of the functioning of automata ideologically intersects with the research of other scientists [16-21], but has fundamental differences. For example, in [16] Benjamin Steinberg also considers a geometric approach to automata theory, but in the context of its use in combinatorial group theory, to solve various problems on the overlap between group theory and monoid theory. In [17] finite automatons are used in problems of encoding and compressing images, as well as in considering regular ω-languages (sets of infinite words defined by finite automata).

The work [18], which studies discrete-event systems, is of great interest, although it also uses symbolic forms of defining automata models of systems.

Quite interesting are the results of [19], which uses a geometric approach to describe such properties, within the framework of which the output function can be characterized by its polygon in the unit square [0, 1] × [0, 1], in [19] also investigated the properties of such polygons and their relationship with the properties of the used output function are investigated.

In this paper, we consider problems from the general problem of recognizing of finite deterministic automatons by properties and signs of their functioning.

In [10] it is shown that for a fixed number of input signals of the automaton and the order on the set of input words, the geometric image is in one-to-one correspondence with the sequence of the second coordinates of the points of the geometric image. From the geometric image γ_s of the automaton $A_s = (S, X, Y, \delta, \lambda)$, where S is the set of states, X is the set of input signals, Y is the set of output signals, $\delta : S\times X\to S$ is the next-state function, $\lambda: S\times X\to Y$ is the function of outputs and $s \in S$ is the initial state, a sequence of second coordinates of points of the geometric image is selected, which one-to-one corresponds to the complete geometric image (with a fixed order on the set X* and the value m = | X |).

As a result, the laws of the automaton functioning and the specific processes of the automata functioning (that is, the phase trajectories) turn out to be uniquely determined by the sequence of the second coordinates of the points of the geometric image.

This allows us to consider an arbitrary sequence of elements from a finite set as a sequence of second coordinates of points of a geometric image and, therefore, as definition of the laws of the automaton functioning, which, in turn, opens up opportunities for analyzing the processes of the functioning of systems through the analysis of the properties of sequences.

The fundamental novelty of this research consists in the development of new recognition methods, which use not the classical specification of automata models of systems by tables, matrices, graphs, systems of logical equations, but the representation of automatic models by their geometric images located on analytically specified curves (and, under certain conditions, extracted from such curves of numerical sequences). The novelty of this research is determined by the fact that such a representation, in contrast to the classical existing methods, in a number of cases allows one to effectively overcome the dimensionality barrier of automaton models of real systems.

2. Mathematical Apparatus and Research Methods

Geometric images of the laws of the functioning of automata recognition of geometric images of automatic models of systems

Geometric image γ_s of the laws of operation (see [10-12]) (the next-state function $\delta : S\times X\to S$ and output functions $\lambda: S\times X\to Y$) of an initial finite state machine $A_s = (S, X, Y, \delta, \lambda)$ with sets of states S, input signals X and output signals Y is determined based on the introduction of a linear order ω in the automata mapping $\rho'_s = \bigcup_{p\in X^*}\{(p,\lambda'(s,p))\}$, where $\lambda'(s,p)=\lambda(\delta(s,p'),x)$, $p=p'x$. An automata mapping ρ'_s (set of pairs) is ordered by the linear order ω, defined based on the order ω_1 on X^* and given by the following rules:

Rule 1. A certain linear order ω_1 is introduced on the set X (which we will denote $\prec_1$);

Rule 2. The order ω_1 on X extends to a linear order on the set X^*, assuming that for any words $p_1,p_2\in X^*$ of unequal length ($|p_1|\neq|p_2|$) $|p_1|<|p_2|\to p_1 \prec_1 p_2$; for any words $p_1,p_2\in X^*$ for which $|p_1|=|p_2|$ and $p_1\neq p_2$, their ratio in the order ω_1 repeats the ratio of the nearest non-coinciding letters of the words p_1 and p_2 to the left.

The order ω'_2 on the set of words Y^* is defined similarly.

After introducing the linear order ω_1 on the set X^* we obtain a linearly ordered set $\rho_s = (\rho'_s, \omega'_1)$, where ω'_1 is the order on ρ'_s induced by the order ω_1 on X^*.

Defining the linear order ω_2 on the set Y and placing the set of points in the coordinate system with the abscissa axis (X^*, ω_1) and the ordinate axis (Y, ω_2), we obtain a geometric image of the laws of functioning of an initial finite state machine $A_s = (S, X, Y, \delta, \lambda, s)$. It should be noted

https://doi.org/10.30564/jmer.v4i2.3588

that the linear orders ω_1 on X^* and ω_2 on Y are generally independent. This means that the specific form of the a geometric image of the laws of functioning of an initial finite state machine $A_s = (S, X, Y, \delta, \lambda, s)$ depends on the chosen orders ω_1 and ω_2. Other variants of linear orderings on X^* are also possible (see, for example, [10,12]). In this paper, the study of the laws functioning of an initial finite state machine is carried out using the order ω_1 on X^* defined above. Linear orders ω_1 and ω_2 allow to replace elements of the sets X^* and Y by their numbers $r_1(p)$ and $r_2(p)$ in these orders. As a result, two forms of geometric images are determined, firstly, as a symbolic structure in a coordinate system D_1, and secondly, as a numerical structure in a coordinate system with integer or real positive semiaxes.

From the geometric image γ_s of the automaton A_s is extracted sequence of second coordinates of points of the geometric image, which one-to-one corresponds to the complete geometric image (for a fixed order on the set X^* and the value $m = |X|$). As a result, the laws of the automaton functioning (that is, the phase picture) and the specific processes of the automaton functioning (that is, the phase trajectories) turn out to be one-to-one determined by the sequence of the second coordinates of the points of the geometric image. This allows us to consider an arbitrary sequence of elements from a finite set as a sequence of the second coordinates of points of a geometric image and, therefore, as setting the laws of the automaton functioning.

The representation of a geometric image γ_s as a numerical structure allows to use the apparatus of continuous mathematics in the formulations and methods of solving problems: setting the laws of the functioning of automata by numerical equations, using numerical procedures, interpolation and approximation of partially given laws of functioning, etc. The geometric image γ_s completely determines the laws of the automaton functioning, that is, the entire phase picture of the connections of the input sequences with the output signals. Specific variants of the functioning processes, that is, phase trajectories, have geometric images $\gamma_s(p), p \in X^*$, in the form of γ_s sections along individual points. Geometric images can also be defined by numerical, rather than symbolic, equations.

3. Results

Recognition of geometric images of automata models of systems

In [10] a formal apparatus for replacing symbolic automaton models in the form of tables, graphs, logical equations, numerical structures in the form of geometric figures, numerical equations and sequences is proposed and developed. This approach is intended to search for new ideas and methods for organizing technical diagnostics of complex systems. In works [10] V.A.Tverdokhlebov proposed and developed methods for the synthesis of an automaton by sequences and geometric curves. In [10], a new type of automaton is proposed - R (α, m, d (α)) - automaton. The laws of functioning of this type of automaton are specified by the numerical sequence α, which is assumed to be the sequence of the second coordinates of the points of the geometric image. An initial segment of length d (α) of the sequence α is considered. The value m is the number of input signals of the automaton.

In this paper, we propose a method for recognizing an automaton in a given finite family of automatons, based on the selection of a set of characteristic sequences from geometric images. The laws of functioning of a complex system in case of malfunctions from a set of accounted for malfunctions and in an operable state are represented by geometric images of automatons. The search for diagnostic sequences with this method of setting the laws of functioning is reduced to finding such intervals on the abscissa axis in which the geometric images corresponding to various faults do not coincide.

In [10] it is shown that for a fixed number of input signals of the automaton and the order on the set of input words, the geometric image is in one-to-one correspondence with the sequence of the second coordinates of the points of the geometric image. In view of this, an effective search for diagnostic influences is possible based on the analysis of numerical sequences. A numerical sequence (a sequence of the second coordinates of the points of the geometric image of the automaton) is associated with each fault from the set of considered and taken into account faults, and the problem of fault recognition is reduced to the problem of finding such numbers of elements in sequences whose values are different in each of the sequences under consideration.

At the large number of sequences and a large length of the sequences themselves, this problem has a complex solution and requires large amounts of computational resources. In view of this, it is proposed to carry out the recognition of the original (numerical) sequences based on the analysis of characteristic (binary) sequences reflecting the location of the values of the elements in the original sequences.

The diagnostic method based on the decomposition of geometric images of automatons includes the following stages:

(1) Construction of a mathematical model of the system in a working state and mathematical models of the laws of the system's functioning in case of malfunctions (faults) in the form of partially specified geometric images of

https://doi.org/10.30564/jmer.v4i2.3588

automatons;

(2) Regularization of partially given geometric images to complete ones based on the use of classical interpolation methods (see [12,14]);

(3) Extraction of numerical sequences (sequences of second coordinates of points) from complete geometric images obtained on the basis of interpolation;

(4) Decomposition of sequences into a set of characteristic sequences without loss of information;

(5) Analysis of the obtained set of characteristic sequences in order to identify such a minimum set of characteristic sequences that covers all faults from the set of considered and taken into account system faults.

To illustrate the described diagnostic method with a reduction in the generality of reasoning, let us assume that the set of considered and taken into account system faults consists of 999 faults, and as a result of the implementation of stages (1)-(3) of the proposed diagnostic method, the following family of numerical sequences { H_0, H_1, H_2, …, H_{999}}, where H_0 is the sequence of the second coordinates of points of the geometric image of the automaton model of an operable system, and H_1, H_2, …, H_{999} are the sequences of the second coordinates of the points of the geometric image of the automaton models of the system in case of malfunctions.

With a reduction in the generality of reasoning, as the sequences H_0, H_1, H_2, …, H_{999}, numerical sequences of length 1000 characters are considered, extracted from the initial segment of a number π with a length of 1,000,000 characters according to the following rule: the first character of the sequence H_i , $0 \leq i \leq 999$, has a number $(i+1)\cdot 1000$ in number π, and the last sign of the sequence H_i has a number $(i+1)\cdot 1000$, i.e. the initial segment of number π with a length of 1,000,000 characters is sequentially divided into 1,000 subsequences of the same length 1,000 characters each.

As a result of the implementation of stage (4), a set of characteristic sequences was built, consisting of 10,000 sequences of length 1000. A computational experiment that implements stage 5 of the proposed diagnostic method revealed the following specific properties of the considerated set of characteristic sequences under. Recognition of all 1000 sequences H_0, H_1, H_2, …, H_{999} (in the case when all 1000 characters are analyzed) is possible using any of 10 characteristic sequences, i.e. each of the sequences H_0, H_1, H_2, …, H_{999} has a unique distribution of all ten digits.

Thus, the amount of necessary diagnostic information can be reduced by at least 10 times (for each malfunction, instead of storing the entire original sequence, it is sufficient to store any of 10 characteristic sequences).

In addition, the following properties are noted, which make it possible to more significantly reduce the amount of diagnostic information:

(1) When using only the first 10 points of the characteristic sequences, 85% of the sequences are recognized;

(2) When using the first 20 points of the characteristic sequences, more than 97% of the sequences are recognized;

(3) When using the first 25 points of the characteristic sequences, more than 99% of the sequences are recognized;

(4) To recognize all 1000 sequences, the first 60 points of the characteristic sequences are sufficient, highlighting the location of the digit 8 in the sequences H_0, H_1, H_2, …, H_{999};

(5) The use of any of the 10 sections of the geometric image for recognizing all 1000 sequences is possible when using the first 90 points of the characteristic sequences.

The performed computational experiment shows that the use of the diagnostic method using the decomposition of geometric images of automatons (using the example of the class (π, m, d (π)) - automatons constructed from the first 1,000,000 digits of π) can significantly reduce the amount of diagnostic information.

The effectiveness of the proposed method for reducing diagnostic information was investigated for another 9 classes of automatons constructed from 9 sequences by length of 1 million characters, specifying the approximations of the following mathematical quantities: e, $\varphi = \frac{1+\sqrt{5}}{2}$ (so-called golden ratio), $\sqrt{2}$, $\sqrt[3]{2}$, ln (2), ln(10), $\zeta(3) = \sum_{x=1}^{\infty} \frac{1}{x^3}$, Catalan's constants $C = \sum_{n=0}^{\infty} \frac{(-1^n)}{(2n+1)^2}$, Euler's constants $\gamma = \lim_{n\to\infty}(1+\frac{1}{2}+\frac{1}{3}+...+\frac{1}{n}-\ln(n))$ (see [15]).

Specific properties are defined for each class. For example, the largest number of recognizable sequences (88%) using only the first 10 points of characteristic sequences is noted in the class of automata constructed from the first million digits of a number $\sqrt[3]{2}$. In the class (e, m, d(e)) - automatons for recognizing all 1000 sequences, it is enough to know the first 54 points in the characteristic (binary) sequence that highlights the location of the digit 1.

The used geometric approach allows us to research the properties of the laws of functioning of discrete deterministic dynamic systems of large dimension based on the analysis of the properties of geometric curves and numerical sequences. In this paper, classes of discrete deterministic automatons are constructed and analyzed, which are determined on the basis of the mathematical properties of geometric images that define the laws of the functioning of automatons.

The results presented in the paragraph show the possibility of practical use of the apparatus of geometric images for specifying and studying the properties of the laws of functioning of discrete deterministic dynamical systems. A method for reducing diagnostic information based on the decomposition of geometric images is proposed. An illustration of the method is given on the example of the class (π, m, d (π)) - automatons constructed from the first million digits of the sequence specifying the approximation of the number π.

A method for recognizing automata, the vertices of the geometric images of the laws of functioning of which are located on analytically specified geometric curves

Let the automaton A_0 be a mathematical model of a workable technical system and the family of automatons $\alpha=\{A_i\}_{i\in I}$ represent the set of faults I of the technical system. Suppose that these automata are given by a geometric image γ_0 and , respectively, by a family of geometric images $\beta=\{\gamma_i\}_{i\in I}$. In the developed method of technical diagnostics, geometric images are assumed to be located on an analytically specified geometric curve L_0 and a family of analytically specified geometric curves $L=\{L_i\}_{i\in I}$. Then equality $L_0\cap\bigcup_{i\in I}L_i=\varnothing$ is determined by the solution of the control problem using a simple unconditional experiment.

Definition 1. Let L be a geometric curve and Δ - a segment on the abscissa axis, on which the curve or part of the curve L is defined. This part of the curve will be denoted by L (Δ).

Theorem 1. Let: - to the initial automaton $A_0 = (S, X, Y, \delta, \lambda, s_0)$, $s_0\in S$, there is a one-to-one correspondence with the geometric image $\gamma_0\subset X^*\times Y$ located on the geometric curve L_0; - the family of initial automatons $\alpha=\{A_i\}_{i\in I}$, where $A_i = (S_i, X, Y, \delta_i, \lambda_i, S_{0i})$, $S_{0i}\in S_i$, is in one-to-one correspondence with a family of geometric images $\beta=\{\gamma_i\}_{i\in I}$ located respectively on geometric curves $L=\{L_i\}_{i\in I}$.

For the proof, see, for example, [12,14].

On the basis of Theorem 1, is proposed a method of recognizing of automatons, the laws of functioning of which are defined by geometric images located on analytically given curves. The method consists of the following steps:

Stage 1. Construction (selection) of a family $L=\{L_i\}_{i\in I}$ of geometric curves and the location on them of geometric images of the laws of functioning of automatons from the family of automatons $\alpha=\{A_i\}_{i\in I}$.

Stage 2. For the system of inequalities $\{L_i\}\cap\{L_j\}=\varnothing$, *i, j*∈*I*, *i* ≠ *j*, is determined the family of solutions $\{\Delta_{ij}\}$, *i, j*∈*I*, *i* ≠ *j*.

Stage 3. A segment $\Delta=\bigcap_{i\neq j}\Delta_{ij}$ is determined, which, by construction, satisfies the following conditions:

(1) If $\bigcap_{i\neq j}\Delta_{ij}\neq\varnothing$, then each point of the segment Δ , which is the first coordinate of points of geometric images of automatons from a family of automatons $\alpha=\{A_i\}_{i\in I}$, determines the solution of the problem of recognizing an automaton in a family of automatons by a simple unconditional experiment.

(2) If $\bigcap_{i\neq j}\Delta_{ij}=\varnothing$, then for the selected specific geometric curves L_i, $i\in I$, and the arrangement of geometric images of the laws of the functioning of automata on these curves, the solution of the problem of recognizing an automaton in a family of automatons does not exist by a simple unconditional experiment.

Stage 4. In accordance with the conditions $\Delta\neq\varnothing$ or $\Delta=\varnothing$ a specific solution to the problem of recognizing an automaton in a family of automatons is determined by a simple unconditional experiment, or it is concluded that for a family of automatons $\alpha=\{A_i\}_{i\in I}$, a selected family of geometric curves $L=\{L_i\}_{i\in I}$ and a chosen arrangement of geometric images on curves, the solution to the problem recognition of an automaton in a family of automata does not exist by a simple unconditional experiment.

Remark to a method. In the developed method, symbolic structures - input and output sequences - are determined not by their numbers according to the linear orders ω_1 and ω_2, but by the numbers associated with the numbers. The numbers are matched to the numbers of the input sequences based on their alignment with points equally spaced on the abscissa axis. To the numbers of the output sequences are mapped half-intervals on the ordinate axis.

4. Discussion

Consider an example of constructing a solution to the problem of recognizing an automaton in a family of automatons whose points of geometric images of the laws of functioning are located on the following geometric curves (see Figure 1): $y_1=e^{(x-5.5)}$ (for an automaton $A_1=(S_1, X, Y, \delta_1, \lambda_1, s_{01})$), $y_2=1+\cos(\frac{x}{1.8}+1.75)$ (for the automaton $A_2=(S_2, X, Y, \delta_2, \lambda_2, s_{02})$), $y_3=\left(\frac{x+1}{6}\right)^3$ (for the automaton $A_3=(S_3, X, Y, \delta_3, \lambda_3, s_{03})$), $y_4=\left(\frac{x-2.8}{3}\right)^2$ (for the automaton $A_4=(S_4, X, Y, \delta_4, \lambda_4, s_{04})$).

For the example under consideration, we will restrict ourselves to 16 points of the geometric image. The relationship between input sequences, numbers of input sequences and numbers associated with numbers of input sequences is shown in Table 1 (with | X | = 2). For output signals, each signal is associated with a half-interval of the form (α, β]. This allows each point in the selected area of the plane with the first coordinate, which is the number associated with the input sequence number, to determine the semi-interval (to which the second coordinate of the point belongs).

In the example under consideration, the number of output signals of the automaton is 74 and each output signal $y_i \in Y$, where $1 \le i \le 74$, is compared to a semi-interval of the form (α_i, β_i], where $\alpha_i = \frac{(i-1)}{10}$ and $\beta_i = \frac{i}{10}$. Table 2 shows the values of the functions $y_1 = e^{(x-5.5)}$, $y_2 = 1+\cos(\frac{x}{1.8}+1.75)$, $y_3 = \left(\frac{x+1}{6}\right)^3$, $y_4 = \left(\frac{x-2.8}{3}\right)^2$ in points, the first coordinates of which are mapped to the numbers of the input sequences (see Table 1).

As a result of the specified choice of the family of geometric curves y_1, y_2, y_3 and y_4 (respectively, for the automatons A_1, A_2, A_3, A_4) and the chosen arrangement of the geometric images of the automatons on the curves (the numbers are corresponded to the numbers of the input sequences based on their alignment with equidistant on the abscissa axis points) and the analysis of the curves, 7 solutions of the problem of recognizing an automaton in a family of automatons $\alpha=\{A_1, A_2, A_3, A_4\}$ were found by a simple unconditional experiment.

Table 1. Relationship of input sequences, number of input sequences and numbers associated with numbers of input sequences.

Numbers of input sequences	Input sequences	Numerical value
1	x_1	0
2	x_2	0,5
3	x_1 x_1	1
4	x_1 x_2	1,5
5	x_2 x_1	2
6	x_2 x_2	2,5
7	x_1 x_1 x_1	3
8	x_1 x_1 x_2	3,5
9	x_1 x_2 x_1	4
10	x_1 x_2 x_2	4,5
11	x_2 x_1 x_1	5
12	x_2 x_1 x_2	5,5
13	x_2 x_2 x_1	6
14	x_2 x_2 x_2	6,5
15	x_1 x_1 x_1 x_1	7
16	x_1 x_1 x_1 x_2	7,5

The solutions obtained using the developed method are the input sequences $p_1= x_1\ x_2\ x_1$, $p_2= x_2\ x_1\ x_1$, $p_3 = x_2\ x_1\ x_2$, $p_4= x_2\ x_2\ x_1$, $p_5= x_2 x_2\ x_2$, $p_6= x_1\ x_1\ x_1\ x_1$, $p_7= x_1\ x_1\ x_1\ x_2$.

Table 3 shows the reactions of the automatons A_1, A_2, A_3, A_4 on 16 input sequences (based on the comparison to the numbers of the output signals $y_i \in Y$, where $1 \le i \le 74$, a semi-interval of the form (α_i, β_i], where $\alpha_i = \frac{(i-1)}{10}$ and $\beta_i = \frac{i}{10}$).

Table 2. Values of functions y_1, y_2, y_3, y_4.

Numbers of input sequences	Numerical value	$y_1=e^{(x-5.5)}$	$y_2 = 1+\cos(\frac{x}{1.8}+1.75)$	$y_3 = \left(\frac{x+1}{6}\right)^3$	$y_4 = \left(\frac{x-2.8}{3}\right)^2$
1	0	0.004	0.821	0.004	0.871
2	0,5	0.006	0.558	0.015	0.587
3	1	0.011	0.329	0.037	0.36
4	1,5	0.018	0.151	0.072	0.187
5	2	0.030	0.039	0.125	0.071
6	2,5	0.049	0	0.198	0.01
7	3	0.082	0.037	0.296	0.004
8	3,5	0.135	0.148	0.421	0.054
9	4	0.223	0.325	0.578	0.16
10	4,5	0.367	0.553	0.770	0.321
11	5	0.606	0.816	1	0.537
12	5,5	1	1.093	1.271	0.81
13	6	1.648	1.362	1.587	1.137
14	6,5	2.718	1.604	1.953	1.521
15	7	4.481	1.799	2.370	1.96
16	7,5	7.389	1.933	2.843	2.454

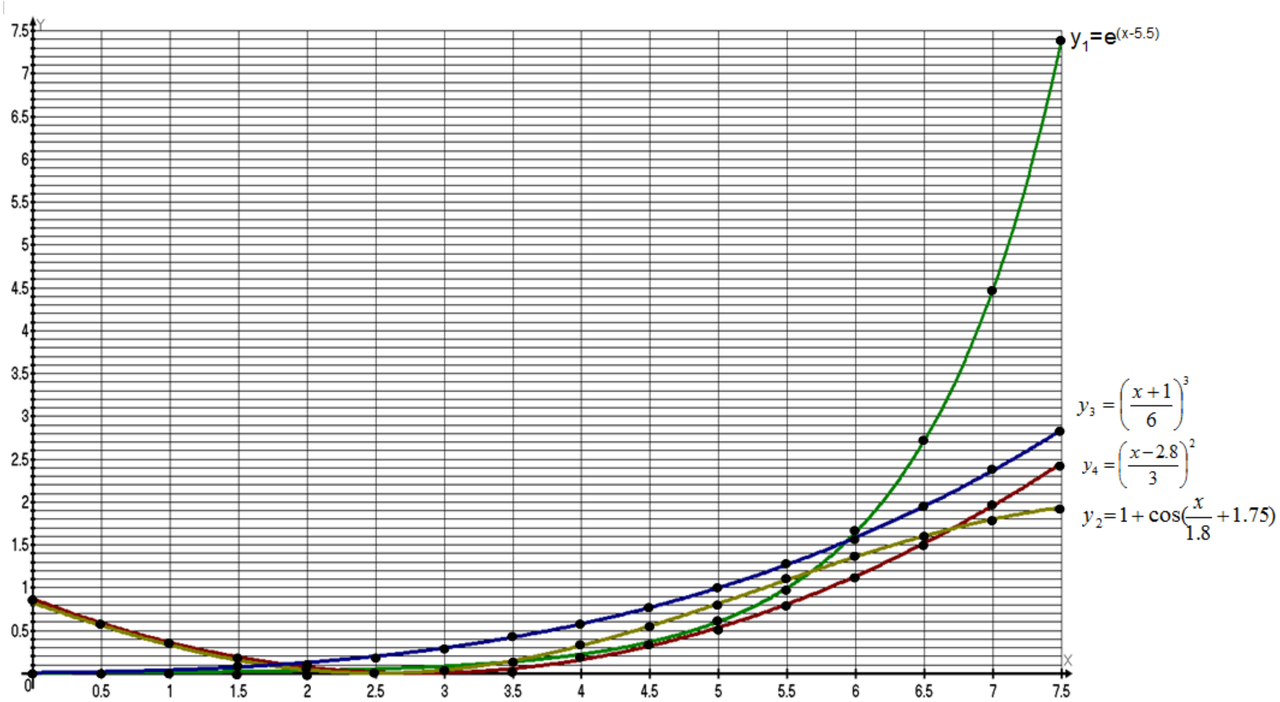

Figure 1. Geometric curves on which the geometric images of the laws of functioning of the automatons A_1, A_2, A_3, A_4 are located

Table 3. Reactions of automatons A_1 , A_2 , A_3 , A_4 .

Number of sequence	Numerical value	Input sequences	A_1	A_2	A_3	A_4
1	0	x_1	y_1	y_9	y_1	y_9
2	0,5	x_2	y_1	y_6	y_1	y_6
3	1	$x_1\ x_1$	y_1y_1	y_9y_4	y_1y_1	y_9y_4
4	1,5	$x_1\ x_2$	y_1y_1	y_9y_2	y_1y_1	y_9y_2
5	2	$x_2\ x_1$	y_1y_1	y_6y_1	y_1y_2	y_6y_1
6	2,5	$x_2\ x_2$	y_1y_1	y_6y_1	y_1y_2	y_6y_1
7	3	$x_1\ x_1\ x_1$	$y_1y_1y_1$	$y_9y_4y_1$	$y_1y_1y_3$	$y_9y_4y_1$
8	3,5	$x_1\ x_1\ x_2$	$y_1y_1y_2$	$y_9y_4y_2$	$y_1y_1y_5$	$y_9y_4y_1$
9	4	$x_1\ x_2\ x_1$	$y_1y_1y_3$	$y_9y_2y_4$	$y_1y_1y_6$	$y_9y_2y_2$
10	4,5	$x_1\ x_2\ x_2$	$y_1y_1y_4$	$y_9y_2y_6$	$y_1y_1y_8$	$y_9y_2y_4$
11	5	$x_2\ x_1\ x_1$	$y_1y_1y_7$	$y_6y_1y_9$	$y_1y_2y_{10}$	$y_6y_1y_6$
12	5,5	$x_2\ x_1\ x_2$	$y_1y_1y_{10}$	$y_6y_1y_{11}$	$y_1y_2y_{13}$	$y_6y_1y_9$
13	6	$x_2\ x_2\ x_1$	$y_1y_1y_{17}$	$y_6y_1y_{14}$	$y_1y_2y_{16}$	$y_6y_1y_{12}$
14	6,5	$x_2\ x_2\ x_2$	$y_1y_1y_{28}$	$y_6y_1y_{17}$	$y_1y_2y_{20}$	$y_6y_1y_{16}$
15	7	$x_1\ x_1\ x_1\ x_1$	$y_1y_1y_1y_{45}$	$y_9y_4y_1y_{18}$	$y_1y_1y_3y_{24}$	$y_9y_4y_1y_{20}$
16	7,5	$x_1\ x_1\ x_1\ x_2$	$y_1y_1y_1y_{74}$	$y_9y_4y_1y_{20}$	$y_1y_1y_3y_{29}$	$y_9y_4y_1y_{25}$

5. Practical Use

Construction and analysis of automata models of FPGA

Field Programmable Gate Array (FPGA) concern to a class of complex technical devices with large dimensions of a set of signals and memories. FPGA is complex digital integrated microcircuits consisting of programmed logic blocks and programmed connections between these blocks. FPGA are widely used not only for realization of simple controllers and the interface units, but also for digital processing signals, complex intellectual controllers, neurochips and in systems of mobile communication.

Mathematical models of integrated chips are the basic information for the decision of problems of development of chips, the analysis and technical diagnosing, optimization of structures and laws of functioning of integrated circuit. Field Programmable Gate Array (FPGA) concern to technical devices with enough complex structure, complex laws of functioning and the big dimension of sets of signals and memories (at present the industry lets out models of FPGA with more than 1000 pins). In this connection mathematical models of FPGA available now, particularly, the finite state machines, are not sufficient not only for the decision of problems, but even for explicit representation of FPGA.

In this parer is considered construction of mathematical model of FPGA in the form of symbolical and numerical graph (located on analytically set curves) and also a basic provisions of diagnosing of FPGA based on use of the apparatus of geometrical images of laws of functioning of state machines (automatons). Without loss of generality as an example in article is analyzed one of the most widespread classes of algorithms of digital processing of signals, realizing on FPGA– the algorithms based on application of orthogonal transformations.

Now FPGA is used for construction various on complexity and opportunities digital devices. Existing mathematical models of FPGA, in particular, the finite state machines, do not allow to represent obviously FPGA in view of their big dimension (existing FPGA contain up to 10 million logic gates, have more than 1000 pins and tens mbyte of the built in block memory). In this work is offered to use the mathematical apparatus of geometrical images of state machine (see [10]) for the representation and research of laws of functioning of FPGA, including for the decision of problems of technical diagnosing. In work [10] Tverdohlebov V.A. is shown, that, technical diagnosing of systems, which are characterized as large-scale or complex systems carried out in conditions of essential restrictions on mathematical models and means of diagnosing. FPGA as object of diagnosing does not suppose enough a full and exact intuitive review and formal representation by traditional means: tables, columns, the logic equations. Besides opportunities of means of diagnosing in each used interval of time are limited by supervision only parts of structure of object and supervision only some functions of object. The analysis of working capacity and localization of defects can be demanded on the interval of time somehow removed from the beginning of functioning of object. Technical diagnosing of FPGA cannot be carried out by homogeneous means of diagnosing. Only overlapping of testing, measurement of physical parameters, the analysis of processes of "decision" objects of diagnostic problems, optical survey and the signal system, etc. should form means of diagnosing.

The method of technical diagnosing of complex systems with use of the apparatus of geometrical images [10] includes construction of mathematical models of means of technical diagnosing in the form of communication of diagnostic interactions with reactions to them of object of diagnosing; construction of mathematical models in the form of geometrical images for object of the diagnosing, including development of geometrical images on the basis of interpolation and extrapolation; development of strategy of carrying out of diagnostic experiment on the basis of the analysis of geometrical images and realization of diagnostic experiment according to the developed strategy.

To illustrate the possible practical application of the apparatus of geometric images of automata in this paper is considered construction of mathematical model in the form of a geometrical image of the FPGA of family Xilinx Spartan II (see [22]), including development of geometrical images on the basis of classical methods of interpolation of Newton, Lagrange and Gauss (a detailed description of the method of synthesizing an automaton model of an FPGA in the form of a geometric image is not given due to limitations on the size of the article, it can be found, for example, in work [12]). One of the basic classes of algorithms of digital processing signals implementated by FPGA – the algorithms based on application of orthogonal transformations is considered: fast Fourier transformation (FFT), Hartly, EWT, Hadamard, Karhunene-Loev expansion etc. (Figure 2 represent as an example the algorithm based on orthogonal transformation - algorithm of 16-dot fast Fourier transformation (FFT)).

FPGA is programmed on realization of the specified algorithms with use of system Xilinx ISE 9.2i. Efficiency of the specified methods of interpolation for restoration of partially set geometrical images of laws of functioning is analyzed at a various arrangement and number of units of interpolation. In Figure 3 is represented the example (it is schematically shown) of comparison on an initial interval of an initial geometrical image and the geometrical image constructed with use of a method of interpolation of Newton (in the given example at programming of FPGA as off pins are used only 4 pin). Lack of a method of interpolation of Gauss unlike the considered methods of interpolation of Newton and Lagrange is restriction of an opportunity of its use only for a case of equidistant units of interpolation. (A detailed description of the research of the effectiveness of various interpolation methods as a means of completing the definition of automatons models can be found in work [12]). The given property imposes additional restrictions on allocation of units

https://doi.org/10.30564/jmer.v4i2.3588

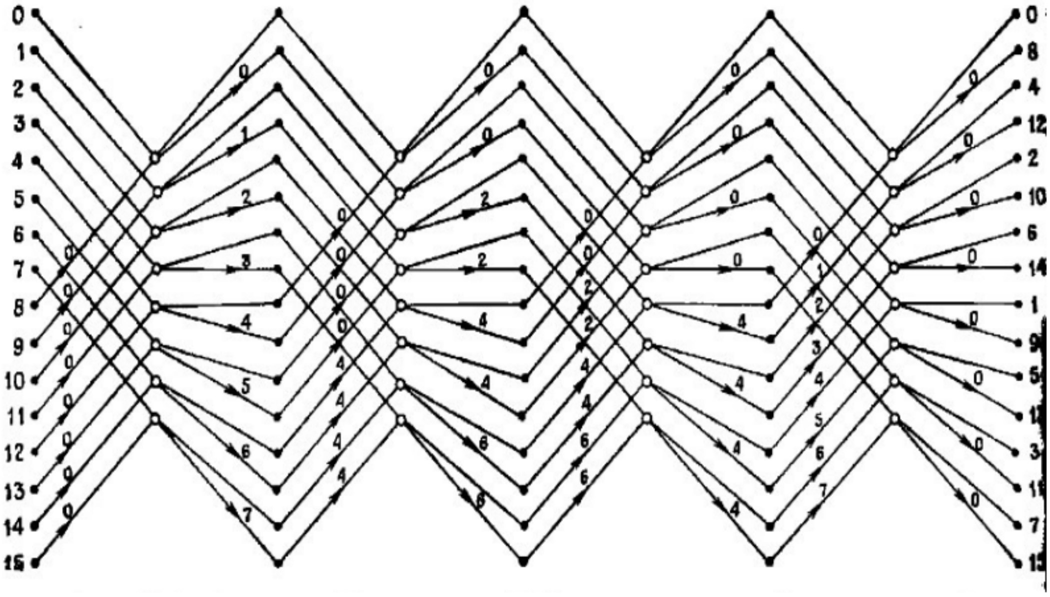

Figure 2. Algorithm 16-dot FFT on the basis 2 with constant structure, without replacement, with normal order and binary-inverse on an output (multipliers for decimation on time and frequency are shown).

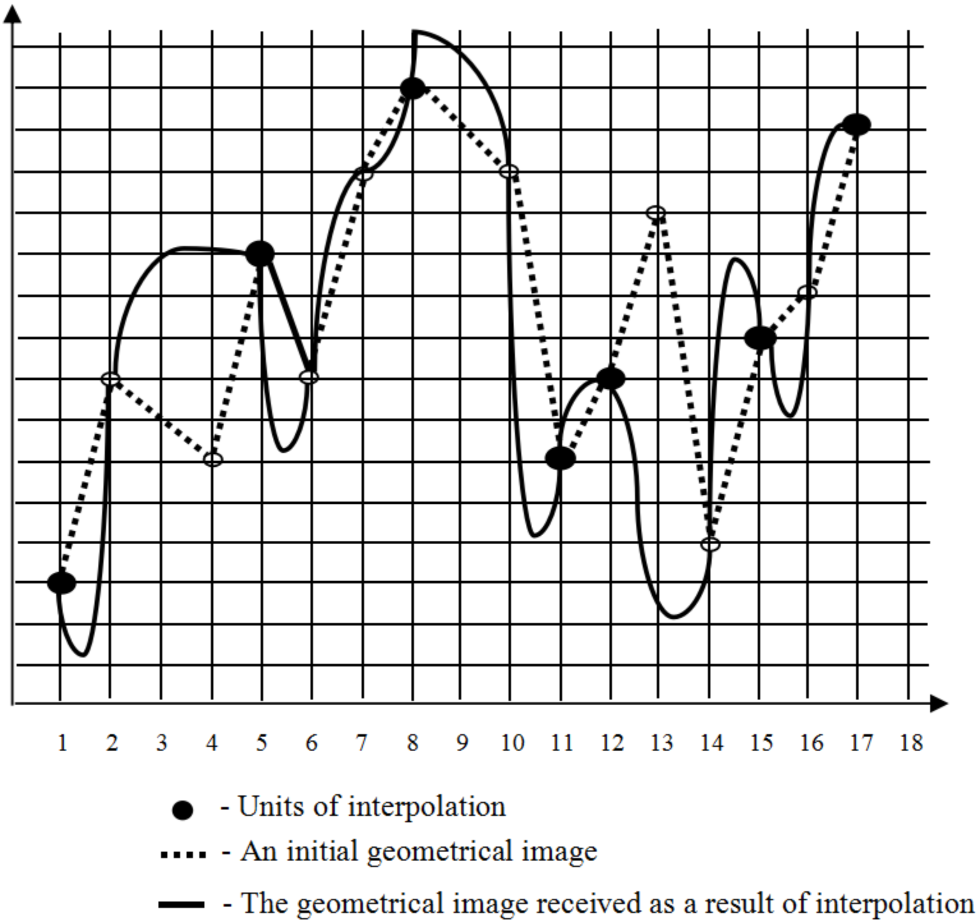

Figure 3. Initial pieces of an initial geometrical image and restored by means of a method of interpolation of Lagrange.

https://doi.org/10.30564/jmer.v4i2.3588

of interpolation. On the basis of the lead computing experiment it is shown, that for a considered class of algorithms the method of interpolation of Gauss yields the best results, than methods of interpolation of Newton and Lagrange. For each of the considered algorithms from 2 methods of interpolation (Newton and Lagrange) the most effective method is certain.

Base model of the discrete determined dynamic systems are the finite state machines. The analysis of such state machines can be made on the basis of research of the mathematical structures representing specificity of laws of functioning of the state machines. As such structures can be used geometrical images of laws of functioning of automata. Use of the apparatus of geometrical images for the definition of laws of functioning of the discrete determined dynamic systems allows to carry out search of diagnostic sequences effectively. For this purpose from set of considered malfunctions and to an efficient condition of system the mathematical model in the form of a geometrical image of laws of functioning of the state machine is compared with each malfunction. Points of geometrical images are assumed located on the curves which can be set analytically. At such way of the definition of diagnostic model search of diagnostic sequences is reduced to a finding of intervals on an axis of abscissa in which the geometrical curves representing mathematical models of malfunctions, have no even points. Effective search of such intervals can be carried out on the basis of the decision of systems of inequalities (or equalities).

6. Conclusions

In this paper we propose methods for recognizing automata models of systems defined by analytically specified geometric curves (on which points are located, interpreted by using the apparatus of geometric images of automata as a pairs of automata mappings). It is proposed to carry out the recognition of automata by their geometric images based on the decomposition of the original (numerical) sequences into a set of characteristic sequences and their subsequent analysis. In a number of cases, the combined use of the proposed methods for recognizing automata makes it possible to effectively overcome the dimensionality barrier of automaton models of systems. One of the problems of interest for further research is the problem of developing a search method under the conditions of specific variants of restrictions on the use of means of control and diagnostics of variants of specific sets of observation sites of control and diagnostic information.

References

[1] McCulloch W.S., Pitts W. (1943). A logical calculus of the ideas immanent in nervous activity [J]. Bulletin of Math. Biophysics. 5:115-133.

[2] Agibalov G.P. (1993). Discrete automata on semilattices [M]. Tomsk.

[3] Aizerman M.A. et al. (1963). Logic. Automatons. Algorithms [C].. Fizmatgiz.

[4] Aperiodic automata [C]. (1974). Moscow, Nauka .

[5] Arbib M. (1966). Automata theory and control theory: a rapprochement.Automatica [C], 3:161-189.

[6] Arbib M. (1967). Tolerance automata . Kybernetic[J], 3:223-233.

[7] Achasova S.M. (1978). Algorithms for the synthesis of automata on programmable matrices [M]. Moscow, Radio and Communication.

[8] Aho A., Hopcroft J., Ullman J. (1979). Construction and analysis of computational algorithms [M]. Moscow, Mir.

[9] Neumann J. (1966). Theory of Self-Reproducing Automata [M]. University of Illinois Press.

[10] Tverdokhlebov, V.A. (2008). The geometrical images of laws of functioning of finite state machines [M]. Science book, Saratov.

[11] Tverdokhlebov, V.A. (2005). The geometrical images of the finite state machines [J], Proceedings of Saratov State Univercity (a New series), 5:141-153.

[12] Epifanov, A.S. (2014). Models and methods for analysis and redefining the laws of functioning of discrete dynamic systems [M], Publishing Center Science, Saratov.

[13] A. Gill (1962). Introduction to the Theory of Finite-state Machines [M]. McGraw-Hill.

[14] Epifanov A.S. (2017). Redefinition, recognition and analysis of automatic models of systems by their geometric images [C]. Proceedings of MLSD‘2017 conference: Management of Large-Scale Systems Development (MLSD‘2017).

[15] http://oeis.org/.

[16] Steinberg B. (2001). Finite state automata: a geometric approach [J]. Transactions of the american mathematical society. 9:3409-3464.

[17] J¨urgensena H., Staigerc L., Hideki Yamasakid. (2007). Finite automata encoding geometric figures [J]. Theoretical Computer Science. 381: 33-43.

[18] Schneider S. (2019). Deterministic pushdown automata as specifications for discrete event supervisory control in Isabelle [D]. Technische Universität Berlin.

[19] Sergey Yu. Melnikov, Konstantin E. Samouylov. (2020) Polygons characterizing the joint statistical properties of the input and output sequences of the binary shift register [C]. ICFNDS ,20: The 4th International Conference on Future Networks and Distributed Systems (ICFNDS). Article No.: 10 Pages 1–6 https://doi.org/10.1145/3440749.3442601.

[20] Rosin P., Adamatzky A., Xianfang Sun. (2014). Cellular automata in image processing and geometry [C], Springer.

[21] Su, R., van Schuppen, J.H., Rooda, J.E., and Hofkamp, A.T. (2010). Nonconflict check by using sequential automaton abstractions based on weak observation equivalence. Automatica, 46(6), 968-978.

[22] www.xilinx.com.

BILINGUAL PUBLISHING CO.
Pioneer of Global Academics Since 1984

Journal of Mechanical Engineering Research
https://ojs.bilpublishing.com/index.php/jmer

ARTICLE

Use of the Method of Guidance by a Required Velocity in Control of Spacecraft Attitude

Mikhail Valer’evich Levskii*

Research Institute of Space systems, Khrunichev State Space research-and-production Center, Korolev, Russia

ARTICLE INFO

Article history
Received: 17 September 2021
Accepted: 28 October 2021
Published Online: 3 November 2021

Keywords:
Method of guidance by a required velocity
Iterative control
Free trajectory method
Terminal control
Quaternion
Spacecraft attitude
Prognostic model

ABSTRACT

We apply the method of guidance by a required velocity for solving the optimal control problem over spacecraft’s reorientation from known initial attitude into a required final attitude. We suppose that attitude control is carried out by impulse jet engines. For optimization of fuel consumption, the controlling moments are calculated and formed according to the method of free trajectories together with principle of iterative control using the quaternions for generating commands to actuators. Optimal solution corresponds to the principle “acceleration - free rotation - separate corrections - free rotation - braking”. Rotation along a hitting trajectory is supported by insignificant correction of the uncontrolled motion at discrete instants between segments of acceleration and braking. Various strategies of forming the correction impulses during stage of free motion are suggested. Improving accuracy of achievement of spacecraft's final position is reached by terminal control using information about current attitude and angular velocity measurements for determining an instant of beginning of braking (condition for start of braking based on actual motion parameters is formulated in analytical form). The described method is universal and invariant relative to moments of inertia. Developed laws of attitude control concern the algorithms with prognostic model, the synthesized control modes are invariant with respect to both external perturbations and parametric errors. Results of mathematical modeling are presented that demonstrate practical feasibility and high efficiency of designed algorithms.

1. Introduction

Control problem of turning the spacecraft into given angular position from arbitrary initial attitude in a finite time t_f with minimization of propellant consumption and given accuracy of reorientation was solved. Spacecraft motion around the center of mass is described by quaternion of attitude [1]. Designing the optimal rotation program is based on quaternion models, method of free trajectories, and method of iterative guidance as particular case of the method of guidance by a required velocity [2].

Now, spacecrafts are used in many areas of scientific occupations and industry. In particular, astrophysical researches and other scientific discoveries would be impossible without modern spacecrafts [3-5]. Success of mission and duration of performance in a working point of orbit (orbital position) are provided by successful control of motion, by an efficiency of attitude control (an improved system of spacecraft attitude is especially important for the spacecrafts with instruments and devices for astronomy measurements and for satellites of Earth supervision).

**Corresponding Author:*
Mikhail Valer’evich Levskii,
Research Institute of Space systems, Khrunichev State Space research-and-production Center, Korolev, Russia;
Email: levskii1966@mail.ru

DOI: https://doi.org/10.30564/jmer.v4i2.3725

Numerous papers study control problems of rigid bodies in various statements [6-29]. For spherically symmetric body, time-optimal spatial rotation is known [1]. Diverse methods are used for constructing control program of spacecraft orientation, in particular, algorithm of fuzzy logic [7] or concept of inverse problem of dynamics [8,9]. Finding the optimal solution of spacecraft s motion control is known also [10-24]. Time-optimal maneuvers are more popular [11-20]. Some solutions are obtained for axially symmetric spacecraft [19-22]. Terminal control for orbital orientation of a spacecraft was considered also [25]; controlling the spacecrafts with control moment gyroscopes has features [26-28]. Optimization of spacecraft attitude with minimum fuel consumption is a difficult issue in mathematical aspect (and difficult engineering problem, also). This paper describes optimal program of spatial turn of arbitrary spacecraft realizing the mode of guidance by a required velocity and method of free trajectories. We give numerical estimates of fuel expenditure for realization of a turn taking into account disturbances acting upon the spacecraft (in particular, gravitational and aerodynamic torques). Issues of economical control of spacecraft motion are still relevant and topical today, so the solved problem of a turn is practically important.

2. Angular Motion's Equations and Statement of Control Problem

We consider the case when parameters of a turn (for example, components of turn quaternion) are known in advance, even before the beginning of maneuver; any initial angular differences are possible (from a few degrees up to 180 degrees), angular orientation of right-hand coordinate system *OXYZ* related with a spacecraft (as well as its initial and final positions) being determined relative to a chosen reference basis. It is assumed that the reference system coincides with inertial coordinate system (inertial basis ***I***), as the most popular case. Spacecraft rotation satisfies dynamical equations [1,6]:

$$J_1\dot{\omega}_1 + (J_3 - J_2)\omega_2\omega_3 = M_1,$$
$$J_2\dot{\omega}_2 + (J_1 - J_3)\omega_1\omega_3 = M_2,$$
$$J_3\dot{\omega}_3 + (J_2 - J_1)\omega_1\omega_2 = M_3 \qquad (1)$$

where J_i are central principal moments of inertia of spacecraft, M_i are projections of torque **M** onto principal axes of spacecraft s inertia ellipsoid, ω_i are projections of spacecraft s absolute angular velocity vector $\boldsymbol{\omega}$ onto axes of body basis ***E*** formed by the principal central axes of spacecraft s inertia ellipsoid ($i=\overline{1,3}$). Spacecraft attitude is described by known equation [1].

$$2\dot{\Lambda} = \Lambda \circ \omega \qquad (2)$$

where ω is vector of absolute angular velocity of spacecraft; Λ is quaternion of orientation with respect to basis ***I*** (we assume $||\ \Lambda(0)\ || = 1$). Equation (2) has the boundary conditions $\Lambda(0)=\Lambda_{in}$ and $\Lambda(T)=\Lambda_f$, where T is time of termination of a turn (Λ_{in} and Λ_f have any a priori given values which satisfy the condition $\|\Lambda_{in}\| = \|\Lambda_f\| = 1$ (because quaternion Λ is normalized). We assume that initial and final angular velocities are equal to zero: $\boldsymbol{\omega}(0)=\boldsymbol{\omega}(T)=0$. If spacecraft s actuators are jet engines which control rotations about three axes of a spacecraft, general form of index for fuel expenditure is

$$G = \int_0^T \left(\frac{|M_1|}{l_1} + \frac{|M_2|}{l_2} + \frac{|M_3|}{l_3} \right) dt \qquad (3)$$

where l_1, l_2, and $l_3 > 0$ are the arms of thrust action of jet engines (for attitude control) in channels *x*, *y*, *z*. Optimization problem of spacecraft s spatial reorientation is a finding a control rotating the spacecraft from position Λ_{in} into position Λ_f and minimizing the index (3) under constraint [1,11]:

$$M_1^2 + M_2^2 + M_3^2 \le m_0^2 \qquad (4)$$

and requirement $T \le T_{des}$, where m0 is maximal possible magnitude of control torque M which actuators can give (m0 characterizes a power of spacecraft's actuators); Tdes is a desired duration of turn.

3. Solving the Formulated Problem of Controlled Turn

We assume that spacecraft is solid (it is rigid body). Optimal control of three-dimensional turn must rotate spacecraft from attitude to th Λ_{in} e required attitude Λ_f according to the Equations (1), (2) with minimal functional (3). When finding optimal law of rotation (in sense of minimum (3)), we assume that angular velocity ω (t) is a piecewise continuous time function. It is known [23], spacecraft s rotation optimal in fuel consumption includes two phases with maximal control torque (segment of acceleration and segment of braking), and free motion phase when control torque is absent. This type of controlling reorientation of a spacecraft is called two-pulse control (first pulse for imparting the required angular momentum L to spacecraft s body, and second pulse suppress angular velocity). Taking into account that disturbances act slightly (disturbance torque much less control torque), we suggest that free rotation is optimal for arbitrary spacecraft in sense of consumption G (since control moment Mc is absent). Free rotation is described by known system of equations

$$\dot{\omega}_1 = k_1\omega_2\omega_3\ ,\ \dot{\omega}_2 = k_2\omega_1\omega_3\ ,\ \dot{\omega}_3 = k_3\omega_1\omega_2 \qquad (5)$$

where $k_1 = (J_2 - J_3)/J_1$, $k_2 = (J_3 - J_1)/J_2$, and $k_3 = (J_1 - J_2)/J_3$ are constant coefficients.

Idea of the proposed principle of control consists in determining such angular momentum **L*** under which spacecraft transfers in given attitude Λ_f under free motion. In this case, fuel is expended for spacecraft s acceleration and braking (for increasing the angular velocity and damping of rotation). Reorientation itself is fulfilled without control torque ($\mathbf{M}_c = 0$), and therefore, regime of fuel economy is made practically along entire trajectory of motion. For this approach, basic turn is executed with zero fuel expenditure, and mode of a controlled turn is optimum. Possibility of designing the optimal solution in class of two-impulse control is justified by fact that each segment of attitude trajectory is optimal for chosen criterion. Expense is $G = G_{ac} + G_{fm} + G_{br}$, where G_{ac} is fuel expenditures during acceleration of a spacecraft, G_{br} is expenditures during a braking of a spacecraft, and G_{fm} is fuel expenditures within phase of spacecraft s free rotation (between acceleration and braking).

For slew maneuver, important characteristic is an integral

$$S = \int_0^T |\mathbf{L}(t)| dt \tag{6}$$

The value S is determined only by rotation conditions Λ_{in} , Λ_f , and spacecraft s principal central moments of inertia J_1, J_2, J_3. The calculated value S is $S = K_c t_{ex}$, where K_c is arbitrary magnitude of angular momentum ($K_c > 0$); t_{ex} is the expected time of reorientation from position Λ_{in} into position Λ_f , i.e. time when equality $\Lambda = \Lambda_f$ holds for solution $\Lambda(t)$ of system of Equations (2), (5) with initial conditions $\omega(0) = K_c \omega^* / |J_{SC}\omega^*|$, $\Lambda(0) = \Lambda_{in}$ (the corresponding theorem can be proven [24]), where ω^* is solution of the boundary problem $\Lambda(0) = \Lambda_{in}$, $\Lambda(t_f) = \Lambda_f$, taking into account the Equations (2), (5); t_f is time of arrival to position Λ_f obtained by simulation of motion according to the Equations (2), (5).

The boundary value problem $\Lambda(tj)=\Lambda in$, $\Lambda(tf)=\Lambda f$, for the system of Equations (2), (5), has analytical solution (in elementary functions) only for dynamically symmetric and dynamically spherical bodies. For spherically symmetric spacecraft (when J1=J2=J3), solution p(t), **ω** (t) have elementary form: p(t)=const and **ω**(t)=const, or in detail

$$p_i = \nu_i / \sqrt{\nu_1 + \nu_2 + \nu_3} \text{, and } \omega_i = \frac{2\nu_i \arccos \nu_0}{T\sqrt{\nu_1 + \nu_2 + \nu_3}}$$

where $\nu_0, \nu_1, \nu_2, \nu_3$ are components of turn quaternion $\Lambda_t = \tilde{\Lambda}_{in} \circ \Lambda_f$ [1]. Characteristic (6) is equal to $S = 2J_1 \arccos \nu_0$.

For a dynamically symmetric body (when, for example, $J_2 = J_3$), the optimal control problem is solved completely. We write optimal solution $\omega(t)$ in the following form:

$$\omega 1 = \dot{\alpha} + \dot{\beta} \cos\vartheta \text{, } \omega 2 = \dot{\beta} \sin\vartheta \sin(\dot{\alpha} t + \sigma) \text{, } \omega 3 = \dot{\beta} \sin\vartheta \cos(\dot{\alpha} t + \sigma)$$

where $\sigma = \mathrm{arctg}(p_{20} / p_{30})$; ϑ is the angle between the spacecraft s longitudinal axis and the vector **p** ($0 \le \vartheta \le \pi$); $\dot{\alpha}$ is the angular velocity of its own rotation (around the longitudinal axis); and $\dot{\beta}$ is the angular velocity of the precession (around the vector **p**). Characteristic (6) is equal to

$$S = \sqrt{J_1^2 (\alpha + \beta \cos \vartheta)^2 + J_2^2 \beta^2 \sin^2 \vartheta}$$

where α is angle of turn about longitudinal axis; β is angle of turn about vector p (note, p10=cos ϑ). Optimal values of parameters p0, α , β , and ϑ are determined by the boundary angular positions Λ_{in} and Λ_f through the system of equations [23]

$$\begin{aligned}
&\cos\frac{\beta}{2}\cos\frac{\alpha}{2} - p_{10}\sin\frac{\beta}{2}\sin\frac{\alpha}{2} = \nu_0 \text{,} \\
&\cos\frac{\beta}{2}\sin\frac{\alpha}{2} + p_{10}\sin\frac{\beta}{2}\cos\frac{\alpha}{2} = \nu_1 \text{,} \\
&p_{20}\sin\frac{\beta}{2}\cos\frac{\alpha}{2} + p_{30}\sin\frac{\beta}{2}\sin\frac{\alpha}{2} = \nu_2 \text{,} \\
&-p_{20}\sin\frac{\beta}{2}\cos\frac{\alpha}{2} + p_{30}\sin\frac{\beta}{2}\cos\frac{\alpha}{2} = \nu_3
\end{aligned} \tag{7}$$

concurrently with condition $J_1(\alpha + \beta\cos\vartheta)^2 + J\,\beta^2 \sin 2\vartheta \rightarrow \min$ ($|\alpha| \le \pi$, $0 \le \beta \le \pi$), where J1 is the moment of inertia about longitudinal axis of a spacecraft; J is the moment of inertia about transverse axis of a spacecraft. Optimal values of vector p0 and values α, β, and ϑ, which satisfy the given attitudes Λin and Λf in initial and final instants, can be determined with use of known device [30].

It is essential that many known methods are unsuitable for situations when initial angle of turn between attitudes Λin and Λf is large. Many researchers use method of combining synthesis which use predictive model. But such algorithms give final result and control program that completely depends from the assumed form of predictive model (the chosen model of motion forecast completely determines type of controlled rotation during maneuver). Any author has insuperable mathematical difficulties if takes predictive model even little close to reality. Below we consider one method of optimal reorientation which uses the method of guidance by a required velocity and method of free trajectories.

4. Application of the Method of Guidance by a Required Velocity for Controlled Maneuver

Method's essence consists in periodical correction of spacecraft's attitude trajectory at specified instants of time. Control is reduced to correction for which onboard computer determines angular velocity that is necessary for reaching the given attitude Λ_f under free rotation, calculation of the desired angular momentum, corresponding to the calculated angular rate, and a transferring a correction impulse $\Delta\mathbf{L}$ to spacecraft's body having angular momentum $\mathbf{L}$, if the latter is substantially different from the desired value. Every time, guidance is carried out from current attitude $\Lambda(t)$ to the given position Λ_f. Angular rates that are required for next site of attitude trajectory are calculated by condition of minimum fuel expenditure for further control of spacecraft rotation. The used predictive model has specific feature, the form of this model gives forecast of free rotation in class of spacecraft motion along conical trajectories where direction of angular momentum of dynamically symmetric body is constant in inertial coordinate system. Such approach allows us to solve problem of constructing the optimal control of arbitrary spacecraft turn using the iterations method. Free rotation of a spacecraft is a combination of two motions: precession of longitudinal axis *OX* about angular momentum vector **L** and spacecraft's rotation itself about longitudinal axis *OX*.

For axial-symmetric body (J_2=J_3) the rates of precession $\dot{\beta}$ and proper rotation $\dot{\alpha}$ are constant and connected between themselves by the dependence: $\dot{\alpha} = \dot{\beta}$ (J/J_1 - 1)cosϑ, where J is moment of inertia with respect to transverse axis, J_1 is moment of inertia with respect to longitudinal axis, and ϑ is angle of nutation (angle between longitudinal axis *OX* and angular momentum **L**). The desired vector $\mathbf{L}^*$ runs in the plane which is perpendicular to plane X_sOX_f and is deviated from axis *OX* on angle ϑ that guarantees spacecraft's rotation simultaneously through angles α and β in time T_{des} (we note that X_s and X_f are the directions of spacecraft s longitudinal axis before and after reorientation).

Situations when boundary rates ω (0)= ω (T)=0 (such conditions of spacecraft turn are most typical) are of practical importance. Of course, at times t=0 and t=T angular rate for nominal rotation program are not zero. Consequently, transfer phases are necessary: acceleration of rotation as transition from state of rest (when ω = 0) to regime of rotation with angular momentum of maximum magnitude Lm, and braking, i.e. reduction of spacecraft s angular rate to zero (value Lm is specified by turn duration *T*). Between acceleration of rotation and braking, spacecraft carries out free motion.

We find prediction of free rotation in form of regular precession of dynamically symmetric body. Parameters of predictive model are computed using the condition of maximal approximation of the predicted motion to real rotation of a spacecraft. Let us study system of equations that reflects motion within uncontrolled phase ($\mathbf{M}_c$ = 0). For many spacecrafts, $J_2 \approx J_3$, but $J_2 \neq J_3$. Further on, for definiteness we suppose $J_2 > J_3$, and J_3 much more than J_1 and $|J_2$ - $J_3|$ much less than J_1. Then the moment (J_3 - J_2)$\omega_2\omega_3$ is insignificant, and we assume it as perturbation (we neglect its influence on prediction). For complete integrability of equations of rotation (including kinematic equations for spacecraft attitude) we use assumption about dynamical symmetry of a spacecraft (for predicting only). Moment of inertia J around transversal axis must satisfy the relationship $J_3<J<J_2$. For decreasing the errors of model, choice of concrete value J must preserve invariable characteristic equation of the system. Therefore, condition for finding the value J consists in following:

$$\left(\frac{J-J_1}{J}\right)^2 = \frac{(J_2-J_1)(J_3-J_1)}{J_2 J_3}$$

since ω_1 = const = ω_{10} in simplified system (i.e. system (1) without the moment (J_3 - J_2)$\omega_2\omega_3$), and cyclic frequency is $f = \omega_{10}\sqrt{(J_3-J_1)(J_2-J_1)/(J_2J_3)}$ (we know that dynamically symmetric body has cyclic frequency ω_{10}(J - J_1)/J because ω_1=const).

Dynamics of real spacecraft during free motion is described by the following system:

$$\begin{gathered}
J_1\dot{\omega}_1 = \left(J_2 - J_3\right)\omega_2\omega_3 + M_{\text{xp}} \\
J\dot{\omega}_2 + \left(J_1 - J\right)\omega_1\omega_3 = M_{\text{yp}}J/J_2 + \\
\left(J(J_3 - J_2 - J_1)/J_2 + J_1\right)\omega_1\omega_3 \\
J\dot{\omega}_3 + \left(J - J_1\right)\omega_1\omega_2 = M_{\text{zp}}J/J_3 + \\
\left(J(J_3 - J_2 + J_1)/J_2 - J_1\right)\omega_1\omega_2
\end{gathered} \tag{8}$$

where M_{xp}, M_{yp}, M_{zp} are moments of perturbations, and $J = \frac{J_2J_3}{J_2+J_3-J_1}\left(\sqrt{(1-J_1/J_2)(1-J_1/J_3)}+1\right)$.

Torques in right-hand parts of Equations (8) are small (they can be assumed as perturbations), and they are neglected in predictive model. Then, we can write predictive model as the following system: $\omega_1 = \omega_{10}$ = const ,

$$J\dot{\omega}_2 + \left(J_1 - J\right)\omega_1\omega_3 = 0, \quad J\dot{\omega}_3 + \left(J - J_1\right)\omega_1\omega_2 = 0 \tag{9}$$

Solving the boundary value problem $\Lambda(t_j)$=Λ_j , $\Lambda(t_f)$=Λ_f with (2), (9) taken into account, we will find expressions for calculating the required angular rates ω_{10}, ω_{20}, and ω_{30} (at the beginning of segment of the uncontrolled motion). We remind that j is number of correction, t_j is instant of beginning the correction; fist segment of free motion starts with initial angular velocities which satisfy the boundary value problem $\Lambda(0)$=Λ_{in}, $\Lambda(t_f)$=Λ_f for dynamic system (2), (9).

Taking into account that distinction between real and the predicted rotation is insignificant, we apply method of iterative

DOI: https://doi.org/10.30564/jmer.v4i2.3725

guidance in order to synthesise control program, for impulses of jet engines, during reorientation. In accordance with this principle, entire trajectory of attitude is partitioned in a number of sites within which there is no control (impulses of jet engines are absent). Transition from one site to another site is executed by impulses of correction. There is only one requirement to the sites of uncontrolled rotation: they must pass through positions $\Lambda(t)$ and Λ_{f}. At instant of correction impulse, the calculated angular velocity (the programmed value) is determined

$\omega_{i0}=\omega_{i\,\mathrm{nom}}=L_m p_{i0}/J_i$, and

$L_m=m_0 T_{\mathrm{des}}\left(1-\sqrt{1-4S/(m_0T_{\mathrm{des}}^2)}\right)/2$

where $p_{i\,0}$ are computed by the system (7) in which ν_0,ν_1,ν_2,ν_3 are components of quaternion of discrepancy $\Lambda_{\mathrm{d}}=\tilde{\Lambda}\circ\Lambda_{\mathrm{f}}$ at beginning of correction impulse. If correction impulses are carried out continuously then p_{i0} almost not change practically (because correction moments act constantly in this case). If corrections are made periodically and very often, then $p_{i\,0}$ vary very slightly (insignificantly) but it require the increased expense of fuel also. We offer to correct motion at discrete separate instants of time t_j for decrease of fuel consumption. For example, we can do corrections according to the following law: correction impulse is made at instant when condition $\psi_{\mathrm{f}}=k\psi_0$ is satisfied, and

$\psi_0=2\arccos(\mathrm{sqal}(\tilde{\Lambda}_0\circ\Lambda))$; $\psi_{\mathrm{f}}=2\arccos(\mathrm{sqal}(\tilde{\Lambda}_{\mathrm{f}}\circ\Lambda))$, $k=\mathrm{const}$

where t_j is instant of start of motion correction (j is number of correction), ψ_0 is angle of turn from attitude of last previous correction impulse to the current position, and ψ_{f} is angle of turn from current attitude to final position Λ_{f}. After each correction $\Lambda_0=\Lambda(t_{\mathrm{n}})$, where t_{n} is instant of acting the correction impulse. For fist correction $\Lambda_0=\Lambda_{\mathrm{in}}$ (before the beginning of a turn $\Lambda_0=\Lambda_{\mathrm{in}}$).

It is expedient to select value of coefficient k close to unity. When k increases ($k > 1$), size of the uncontrolled sites increases also, perturbations are accumulated, that leads to increasing fuel expenditure. When k decreases ($k < 1$), corrections are made so frequently that control is almost continuous. In this situation, necessary direction of angular momentum is endlessly recomputed (its magnitude remains constant). By virtue of smallness of sites of rotation this direction is also almost constant in inertial coordinate system. This senseless computing expenditure is totally unjustified because it does not reduce fuel consumption in comparison with control when spacecraft rotate along conical trajectory (in form of regular precession with constant angle of nutation). More best version of strategy for correction of spacecraft rotation is variant when correction impulse is made at half of a hitting trajectory (a predicted motion), i.e. when angle between current position and position preset at ending a controlling impulse (acceleration or correction) is equal to the angle between current position and the required final position. Condition for start of correction is

$$\mathrm{sqal}\,(\tilde{\Lambda}_0\circ\Lambda)=\mathrm{sqal}\,(\tilde{\Lambda}_{\mathrm{f}}\circ\Lambda)\,.$$

If the controlling moment **M** is limited, then a boost of spacecraft angular momentum to the required level $|\mathbf{L}|=L_m$ at beginning of a turn and damping of available angular momentum to zero at end of reorientation maneuver occupy some finite time (distinct from zero). In general case, conditions of turn Λ_{in} and Λ_{f} may be such that one cannot neglect transition segments (acceleration and braking). Quite often the vector **M** obey condition (4). Since initial and final angular velocities are equal to zero and magnitude of control moment is constant $|\mathbf{M}|=\mathrm{const}=m_0$, duration of stages of acceleration and braking is identical. Optimal solution $\omega(t)$ during segment of nominal motion (between acceleration and braking) possesses property $|\mathbf{L}|\approx\mathrm{const}$ (inconstancy of modulus of angular momentum can be due to a presence of disturbing moments and inequality of the moments of inertia $J_2=J_3$).

The laws of fastest imparting and reduction of angular velocity under constraint (4) are known [11]. At segment of acceleration, optimal control has following form [11]:

$$\mathbf{M}=m_0J_{\mathrm{SC}}\omega\,/\,|J_{\mathrm{SC}}\omega| \tag{10}$$

where $J_{SC}=\mathrm{diag}\,(J_1, J_2, J_3)$ is spacecraft s inertia tensor. If differentiate by time last equation, taking into account the Equation (1), then we will obtain the following equations

$$\dot{M}_1=\omega_3M_2-\omega_2M_3\,,\ \dot{M}_2=\omega_1M_3-\omega_3M_1\,,$$
$$\dot{M}_3=\omega_2M_1-\omega_1M_2$$

which show that **M** is constant vector relative to inertial basis ***I***, and $|\mathbf{M}|=\mathrm{const}=m_0$. At optimal motion, angular momentum of a spacecraft does not change direction in inertial coordinate system. Magnitude of angular momentum varies according to the law $|\mathbf{L}|=m_0t$. At segment of braking, optimal control is

$$\mathbf{M}=-m_0J_{\mathrm{SC}}\omega\,/\,|J_{\mathrm{SC}}\omega| \tag{11}$$

(the controlling moment **M** makes with angular momentum an angle of 180 degree) [11]. Angular momentum varies according to the law $|\mathbf{L}|=L_{\mathrm{oc}}-m_0(t-t_{\mathrm{br}})$, where $L_{\mathrm{oc}}=|J_{\mathrm{SC}}\omega(t_{\mathrm{br}})|$; t_{br} is time of beginning of damping. For both acceleration and braking, optimal control (as fast response) is control under which the controlling moment is parallel to angular momentum at any moment of time.

The proposed algorithm performs the control of spacecraft rotation according to method of free trajectories. It presumes correction of spacecraft's rotation at certain discrete instant of time. Entire attitude trajectory consists of alternating the controlled phases and uncontrolled phases, and it includes phases of acceleration and braking, phases of free rotation (when $\mathbf{M}_c = 0$) and short-time phases of correcting the attitude trajectory. Task of control is to provide such start conditions for uncontrolled phases that the predicted trajectory of rotation must pass through final attitude Λ_f. For synthesis of control impulses, quaternion of turn $\Lambda_t^{(n)} = \widetilde{\Lambda}(t_n) \circ \Lambda_f$, at beginning of each non-controlled site t_n, is calculated. Using it, initial rates ω_{10}, ω_{20}, ω_{30} are computed for next site of uncontrolled rotation. Usually, from one to three or five correcting impulses (it depends on turn angle) are sufficient for reorientation. Optimization consists in determining the time of rotation's acceleration and damping of rotation. Control torque on segment of acceleration (braking) is specified by conditions: (10) for acceleration segment, and (11) on the braking segment. Control moment remains immobile vector in inertial space during both segments. Duration of acceleration (braking) τ can be determined as $\Delta t_{ac} \approx \Delta t_{br} = \tau = T_{des}\left(1 - \sqrt{1 - 4S/(m_0 T_{des}^2)}\right)/2$, and time of free motion is $\Delta t_{free} = T_{des}\sqrt{1 - 4S/(m_0 T_{des}^2)}$ (it is assumed that $4S < m_0 T_{des}^2$). Let us explain it.

For free rotation, integral of modulus of spacecraft s angular momentum S does not depend from time of turn T [24]. If durations of transition periods Δt_{ac} and Δt_{br} (acceleration and braking) are small, and the sum $\Delta t_{ac} + \Delta t_{br}$ much less than T_{des}, then integral of modulus of angular momentum during rotation time T barely changes and remains close to S, and the change of modulus of angular momentum during acceleration and braking can be considered linear. Then we have the equality $(T_{des} - (\Delta t_{ac} + \Delta t_{br})/2)L_m = S$, where L_m is modulus of angular momentum at phase of nominal rotation (when $|\mathbf{L}| = \text{const}$); Δt_{ac} and Δt_{br} are durations of acceleration and extinction of angular momentum. We have $\Delta t_{ac} + \Delta t_{\text{Tr}} \geq 2L_m/m_0$, since $\tau = L_m/m_0$ is minimal possible acceleration (braking) time with restriction $|\mathbf{M}| \leq m_0$. Hence $L_m \geq S/(T_{des} - \tau)$ and $T_{des} \approx S/L_m + L_m/m_0$ (since times of acceleration Δt_{ac} and braking Δt_{br} are equal).

As a result, control for spacecraft s spatial reorientation consists in following operations:

(1) The computing the turn quaternion $\Lambda_t = \widetilde{\Lambda}_{in} \circ \Lambda_f$, and the determining the required angular velocities ω_{10}, ω_{20}, and ω_{30} for next uncontrolled phase.

(2) Acceleration of rotation to the calculated angular momentum $\mathbf{L}^*$ under control

$\mathbf{M}_c = m_0(\mathbf{L}^* - \mathbf{L})/|\mathbf{L}^* - \mathbf{L}|$,

where $\mathbf{L}^* = \widetilde{\Lambda} \circ \Lambda_{in} \circ \mathbf{L}_{pr} \circ \widetilde{\Lambda}_{in} \circ \Lambda$, and $\mathbf{L}_{pr}$ is preset vector of angular momentum with components $J_i \omega_{i0}$;

(3) Free rotation ($\mathbf{M}_c = 0$) until instant t_n, when $\text{sqal}\,(\tilde{\Lambda}_0 \circ \Lambda(t_n)) = \text{sqal}(\Lambda(t_n) \circ \widetilde{\Lambda}_f)$.

(4) At instant t_n one should calculate new quaternion of turn and compute initial rates ω_{in} for new site of attitude trajectory (new hitting trajectory). Then the controlling impulse $\Delta\mathbf{L}$: $\Delta L_i = J_i(\omega_{in} - \omega_i)$ is calculated. Control torques are computed $M_i = \Delta L_i/\Delta t$, where Δt is calculated from constraint (4) (Δt is minimum possible value but such that constraint (4) is valid).

Then one should set $t_0 = t_n$ and repeat items (3) and (4) until instant for which $2\psi_f > |\omega||\mathbf{L}|/m_0$.

(5) Damping of spacecraft s rotation using control torque (11) for which $\mathbf{M}_c \cdot \mathbf{L} < 0$, $\mathbf{M}_c = \widetilde{\Lambda} \circ \mathbf{M}_{br} \circ \Lambda$, where $\mathbf{M}_{br} = \Lambda_{br} \circ \mathbf{L}_{br} \circ \widetilde{\Lambda}_{br}$, and $\mathbf{L}_{br}$, Λ_{br} are angular momentum and quaternion of spacecraft attitude at instant of start of braking (i.e., control torque is directed exactly against angular momentum, and direction of controlling torque is constant in inertial basis).

The proposed algorithm of spacecraft s attitude control was patented earlier [29]. Angular velocities ω_{in} required for next site of uncontrolled trajectory are determined using the condition of minimum consumption for control of maneuver terminating. Evidently, in neighborhood of the programmed angular rate $\boldsymbol{\omega}^*$ we can assume that $\omega_{in} = \chi\omega_{in}^*$, i.e. direction of angular rate is immobile (it is known after calculating the vector $\boldsymbol{\omega}^*$), and modulus of angular velocity vector must be optimized: $|\omega| \rightarrow \text{var}$. Therefore, consumption of fuel for maneuver terminating is function of single parameter χ. Spacecraft s rotation begins to be damped since the instant when equality $2\psi_f = |\omega||\mathbf{L}|/m_0$ becomes satisfied.

Optimal control problem of three-dimensional reorientation was solved applying algorithm of joint synthesis based on use of predictive model. Constructed control law is quasi-optimal and invariant, and it does not require exact knowledge of rotation model parameters. Efficiency in sense of energy-saving control is reached by the mode when control torque is absent during main part of maneuver ($\mathbf{M}_c = 0$), and high precision is ensured by the constructing the feedback with use of data about spacecraft's attitude and angular velocity when control torques are formed and generated.

5. Application of the Method of Guidance by a Required Velocity with Prediction

For improving an accuracy of reorientation and for decrease of fuel consumption, we can use information about calculated prognostic position Λ^* at instant of satisfaction of condition $\mathrm{sqal}(\widetilde{\Lambda}_{\mathrm{in}} \circ \Lambda) = \mathrm{sqal}(\widetilde{\Lambda} \circ \Lambda_{\mathrm{f}})$, which is obtained for accurately predicted trajectory passed through current position Λ and the required final position Λ_{f} (i.e. $\mathrm{sqal}\ (\tilde{\Lambda}_{\mathrm{in}} \circ \Lambda^*) =$ $\mathrm{sqal}\ (\Lambda^* \circ \tilde{\Lambda}_{\mathrm{f}})$. Taking into account that real spacecraft motion only slightly differs from the predicted one, let us employ method of iterative guidance in order to form the control moments in process of a turn. Its essence consists of regular correction of spacecraft motion trajectory at fixed moments of time. Correction consists of determining the angular momentum $\mathbf{L}^*$, which is necessary for attaining the final position Λ_{f}, and of imparting the correcting impulse $\Delta\mathbf{L}$ to angular momentum $\mathbf{L}$ of a spacecraft. Entire motion trajectory will consist of alternating active and passive sections and include accelerating and decelerating sections, sections of free motion ($\mathbf{M}_{\mathrm{c}} = 0$), and short-term sections of trajectory correction. Problem of control consists of providing initial conditions for such uncontrolled sections, where predicted motion travels through the required position Λ_{pr}. At first correction, the predicted calculated spacecraft position Λ^* is taken: $\Lambda_{\mathrm{pr}} = \Lambda_{\mathrm{f}} \circ \widetilde{\Lambda}(t_1) \circ \Lambda^*$, and quaternion of turn for computation of fist correction impulse Λ_{c} is $\Lambda_{\mathrm{c}} = \tilde{\Lambda}(t_1) \circ$ $\Lambda_{\mathrm{f}} \circ \tilde{\Lambda}(t_1) \circ \Lambda^*$. At all other corrections of spacecraft motion, $\Lambda_{\mathrm{pr}} = \Lambda_{\mathrm{f}}$ and $\Lambda_{\mathrm{c}} = \widetilde{\Lambda}_j \circ \Lambda_{\mathrm{f}}$.

It was assumed in prognostic model that spacecraft is dynamically symmetric with respect to longitudinal axis and that disturbing moments are negligibly small. Specificity of this model is prediction of free motion of a spacecraft, in class of regular precession of rigid body. If we, taking this into account, solve kinematic problem of attitude with aim of transferring a spacecraft from position Λ_0 to position Λ_{pr}, we get the calculated value of vector of angular momentum $\mathbf{L}^*$. Velocities ω_{10}, ω_{20}, ω_{30} required for next section of free motion are determined from condition of fuel consumption minimum for the following control of spacecraft turn. It is evident that, in neighborhood of the calculated vector of angular velocity ω^*, we can consider its direction as fixed. In this case, fuel consumption G is function of only magnitude of angular velocity vector, which should be optimized. Sections of acceleration and deceleration coincide with predicted trajectories (because disturbance moment $\mathbf{M}_{\mathrm{d}}$ is much less than control moment $\mathbf{M}_{\mathrm{c}}$), and their duration is determined by time of a turn, value of control moment that could be achieved, and quaternion of a turn. Duration of free motion sections is determined from condition of minimization of the functional G. Thus, control of spacecraft turn is reduced to successive realization of the following operations:

(1) Calculation of turn quaternion $\Lambda_{\mathrm{t}} = \widetilde{\Lambda}_{\mathrm{in}} \circ \Lambda_{\mathrm{f}}$ and determination of initial angular velocities for passive section ω_{10}, ω_{20}, ω_{30}; prediction of spacecraft angular position Λ^* to instant of first correction $\mathrm{sqal}(\widetilde{\Lambda}_{\mathrm{in}} \circ \Lambda^*) = \mathrm{sqal}(\Lambda^* \circ \widetilde{\Lambda}_{\mathrm{f}})$; determination of the required angular momentum $\mathbf{L}^*$ and control moment $\mathbf{M}$; we set $\Lambda_0 = \Lambda_{\mathrm{in}}$;

(2) Acceleration of a spacecraft to the required angular momentum, and magnitude of control moment is maximal; accelerating torque is $\mathbf{M}_{\mathrm{c}} = \widetilde{\Lambda} \circ \mathbf{M}_{\mathrm{ac}} \circ \Lambda$; and $\mathbf{M}_{\mathrm{ac}}$ is maximal accelerating torque in inertial coordinate system, $\mathbf{M}_{\mathrm{c}} \cdot \mathbf{L} > 0$;

(3) Free motion of a spacecraft ($\mathbf{M}_{\mathrm{c}} = 0$) up to instant when $\mathrm{sqal}\ (\tilde{\Lambda}_0 \circ \Lambda(t_j)) = \mathrm{sqal}\ (\Lambda(t_j) \circ \tilde{\Lambda}_{\mathrm{f}})$, i.e., up to half of turn angle;

(4) At instant of time t_j , determination of new turn quaternion $\Lambda_{\mathrm{t}} = \widetilde{\Lambda}(t_j) \circ \Lambda_{\mathrm{pr}}$ (moreover $\Lambda_{\mathrm{pr}}^{(1)} = \Lambda_{\mathrm{f}} \circ$ $\tilde{\Lambda}(t_1) \circ \Lambda^*$, and $\Lambda_{\mathrm{pr}}^{(j)} = \Lambda_{\mathrm{f}}$ if $j > 1$) and determination of initial angular velocities for new section (new hitting trajectory) ω_{1j}, ω_{2j}, ω_{3j}; determination of the required impulse of angular momentum $\Delta\mathbf{L}$ equal $\Delta L_1 = J_1(\omega_{1j} - \omega_1)$, $\Delta L_2 = J_2(\omega_{2j} - \omega_2)$, $\Delta L_3 = J_3(\omega_{3j} - \omega_3)$ and transfer of it to body of a spacecraft; here control moment $\mathbf{M}_{\mathrm{c}} = \Delta\mathbf{L}/\Delta t$ (Δt is such that condition (4) is satisfied; we assume that $t_{\mathrm{in}} = t_j$ and repeat points (3) and (4) up to instant of time $t = t_{\mathrm{f}} - \tau$;

(5) Slowing down the angular velocities of a spacecraft with maximum control moment $\mathbf{M}_{\mathrm{c}} \cdot \mathbf{L} < 0$, $\mathbf{M}_{\mathrm{c}} = \widetilde{\Lambda} \circ \mathbf{M}_{\mathrm{br}} \circ \Lambda$ (i.e., control moment is directed exactly against the vector of angular momentum).

Scheme of iterative control that is proposed here allows one to take into account random factors on previous stages of spacecraft motion, thus decreasing the fuel consumption needed for control in further corrections. This is achieved due to exploiting the information about random and stochastic factors concerning spacecraft motion before first correction of angular momentum. Quaternion $\Delta\Lambda = \widetilde{\Lambda}^* \circ \Lambda_1$ contains information concerning stochastic factors, random acts and perturbations, and factors that were not taken into account in control law. If we introduce it in sight parameters while forming the first correcting impulse, trajectory of free motion will be passed with lesser deviation from the required final position Λ_{f} (and with lesser expenditures needed for its compensation). Subsequent corrections are realized by guidance at final position (reaiming is done every time, from current position Λ to final one, Λ_f). The obtained control law for spacecraft turn is sufficiently close to optimal one and allows one to decrease significantly the error in reducing the axes related with the spacecraft to a fixed final position Λ_f, in relation to other algorithms for realizing the method of guidance by a required velocity together with method of free trajectories. If conditions of turn Λ_{in}, Λ_f, and time T are such that times of acceleration and braking are very small (in comparison with total time of turn T) and we may to neglect them, then one can consider as impulsive processes both imparting necessary angular momentum L_m to spacecraft and reducing available angular momentum down to zero, and almost during all turn (between acceleration and braking) $|\mathbf{L}(t)|$ =const=L_m. These control algorithms can be easily realized by existing onboard means.

If durations of acceleration and braking are much smaller than duration of turn T, then the torque $\mathbf{M}$ is directed strictly against angular momentum $\mathbf{L}$ at spacecraft braking, and instant when braking begins can be predicted with high accuracy. Duration of rotation damping is $\tau = |\mathbf{L}|/m_0$ [11]. Instant of beginning of braking segment is determined by the condition [26]:

$$4\arcsin\frac{K\sqrt{\delta_2^2+\delta_3^2}}{\sqrt{(J_2\omega_2)^2+(J_3\omega_3)^2}}=\frac{K^2\sqrt{\omega_2^2+\omega_3^2}}{m_0\sqrt{(J_2\omega_2)^2+(J_3\omega_3)^2}}$$

where δ_1, δ_2, δ_3 are components of vector part of mismatch quaternion $\tilde{\Lambda}(t)\circ\Lambda_f$; $K=|J\omega|$ is magnitude of spacecraft s angular momentum. At braking segment, cancellation of angular momentum is carried out according to linear law: $|\mathbf{L}(t)| = L_m - m_0(t - t_{br})$, where t_{br} is instant of beginning of braking.

Thus, we solved the problem of control for a programmed turn optimal with respect to fuel consumption on basis of algorithm with prognostic model. We investigated case when spacecraft s inertial characteristics are not exactly known in advance. Optimal solution to this problem is obtained in class of controls realized by method of free trajectories. Numerical realization of algorithm for coincident synthesis of optimal control in process of spacecraft turn is affected. Effective methods of control of terminal reorientation of a spacecraft is presented, one of which additionally has adaptive qualities - it is invariant with respect to external perturbations and substantially insensitive with respect to parametric errors. Indices of quality (economy and accuracy) of obtained laws are sufficiently high. Relatively low level of fuel consumption for a turn is achieved due to the transfer from permanent control of spacecraft attitude to formation of control moments only at certain definite instants of time. High accuracy of attitude is achieved by correcting angular momentum of a spacecraft by varying its angular momentum up to its calculated value during reorientation process, at stage of free rotation, at discrete instants of time. Determination of time instant t_{br} according to actual (the measured values) kinematic parameters of motion (angular mismatch and angular velocity) improve accuracy of bringing the spacecraft into the required state $\Lambda=\Lambda_f$, $\omega=0$.

6. Example of Numerical Solving the Control Problem and Results of Mathematical Modeling

Let us provide numerical solution of spacecraft s optimal control problem with respect to a programmed rotation. We consider maneuver from initial attitude Λ_{in}, when body axes coincide with axes of the supporting basis $\boldsymbol{I}$, into the given final position Λ_f with the following elements:

$$\lambda_0 = 0, \lambda_1 = 0.8, \lambda_2 = 0.6, \lambda_3 = 0$$

Spacecraft rotates from state of rest to state of rest, therefore initial and final angular velocities are zero: $\boldsymbol{\omega}(0)=\boldsymbol{\omega}(T)=0$. We assume that maximum possible magnitude of the controlling moment m_0 and spacecraft s principal central inertia moments have values:

m_0=75 N m, J_1 = 63559.2 kg m^2, J_2 = 192218.5 kg m^2, and J_3 = 176808.9 kg m^2

Also, we assume that duration of reorientation maneuver should be 360 seconds, approximately. As result of solving kinematic reorientation problem on transition from position $\Lambda(0)=\Lambda_{in}$ into position $\Lambda(T)=\Lambda_f$ (optimal rotation problem in impulse statement), we obtained value of ort of spacecraft s angular momentum for end of acceleration segment $\mathbf{p}_0$={0.600828; 0.451445; 0.659699}, if assume that spacecraft is dynamically symmetric body.

Optimal motion of a spacecraft consists of segments on which control moment maximum in magnitude acts (segments of acceleration and braking), of segments of free rotation, and of several corrections of angular motion within stage between acceleration and braking. On segment of maximal control moment, angular momentum vector $\mathbf{L}$ has permanent direction in inertial space, but it is variable in magnitude (increase up to preset value on acceleration segment, and decrease to zero on braking segment), while moment $\mathbf{M}$ is immovable with respect to reference basis $\boldsymbol{I}$ (the vectors $\mathbf{M}$ and $\mathbf{L}$ are parallel). During spacecraft rotation with maximum angular momentum modulus, parameters of motion are supported maximum nearby to the programmed values by impulses of the controlling moment. In this case, angular momentum vector $\mathbf{L}$ has approximately constant magnitude L_m between acceleration and braking. During correction impulses direction of angular mom

DOI: https://doi.org/10.30564/jmer.v4i2.3725

entum **L** varies from preset position to direction required for a hitting to final Λ_f. The calculated duration of acceleration (braking) is τ = 12 s. Maximal magnitude of angular momentum (the programmed level) is $L_m = 900$ N m s.

Results of mathematical modeling of rotation process under optimal control in accordance with the method of guidance by a required velocity are demonstrated in Figures 1-4. Turn s duration was T=360.24 s. It means that perturbations (including asymmetry of the spacecraft) complicate rotation into required position. Visual illustration of rotation dynamics is given in Figure 1, where we present graphs of the changing angular velocities $\omega_1(t)$, $\omega_2(t)$, and $\omega_3(t)$ in time. In Figure 2 we present graphs of the changing components of quaternion $\Lambda(t)$, determining spacecraft s current attitude during rotation: $\lambda_0(t)$, $\lambda_1(t)$, $\lambda_2(t)$, and $\lambda_3(t)$. Figure 3 shows dynamics of the changing the components $p_1(t)$, $p_2(t)$, and $p_3(t)$ of ort **p** of angular momentum. The following rule is observed for functions $\omega_1(t)$ and $p_1(t)$: these functions are sign functions of time for any combinations of boundary values Λ_{in} and Λ_f. From Figure 1 and Figure 3, we see that number of motion corrections is five. Figure 4 shows character of changing the controlling moment, where we see all phases of controllable turn: acceleration of a spacecraft up to the programmed angular momentum, free motion, braking of spacecraft rotation, and short-term impulses of correction. Corrections of spatial motion are formed by the law that is described in section 4. In Figure 5, we see variations of angles ψ_f and ψ_0; ψ_f is smooth monotonically decreasing function of time, ψ_0 is piecewise continuous function of time, which is monotonically increasing function of time within intervals of continuity (between corrections). Instants of corrections are as follows:

t_1=179.2 s , t_2=267.8 s , t_3=312.72 s , t_4=335.12 s , t_5=346.4 s

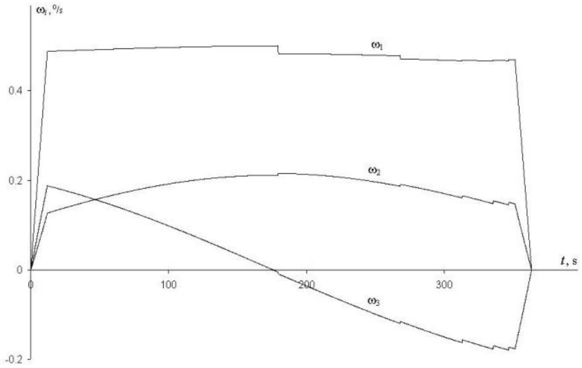

Figure 1. Optimal variation of angular rates during spatial reorientation

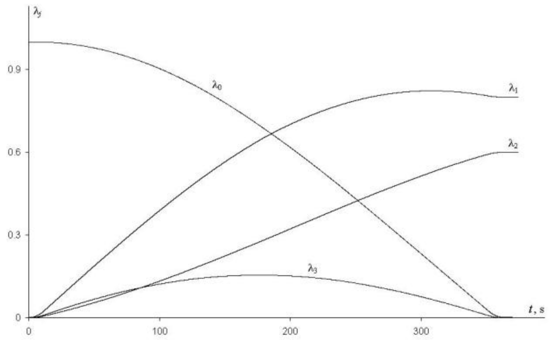

Figure 2. Variation of parameters of attitude during rotary maneuver

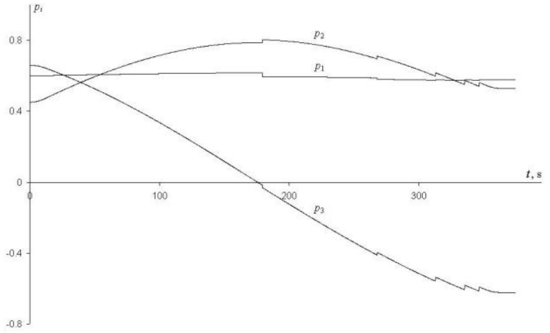

Figure 3. Elements of unit vector **p** as functions of time

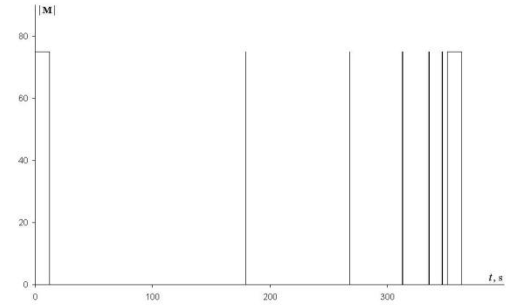

Figure 4. Changing the magnitude of control torque during optimal maneuver

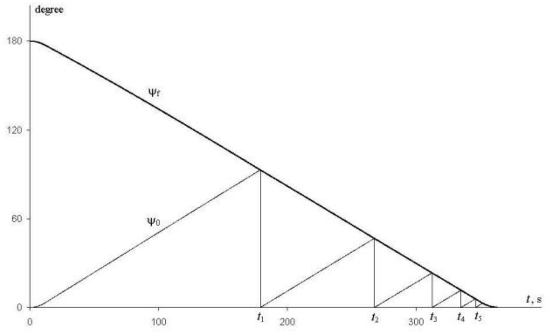

Figure 5. Angles ψ_f and ψ_0 and instants of corrections

DOI: https://doi.org/10.30564/jmer.v4i2.3725

Magnitudes of impulses of angular momentum for rotation correction are:

$\Delta L_1 = 30$ N m s , $\Delta L_2 = 24$ N m s , $\Delta L_3 = 30$ N m s , $\Delta L_4 = 36$ N m s , and $\Delta L_5 = 33$ N m s

Respectively, durations of correction impulses are as follows:

$\Delta t_1 = 0.40$ s, $\Delta t_2 = 0.32$ s , $\Delta t_3 = 0.40$ s , $\Delta t_4 = 0.48$ s ,
$\Delta t_5 = 0.44$ s

Since Δt_n are small, the controlling moment for correction of motion can be calculated as follows:

$$M_{ci} = \frac{m_0(J_i\omega_{in} - J_i\omega_i)}{\sqrt{(J_1\omega_{1n} - J_1\omega_1)^2 + (J_2\omega_{2n} - J_2\omega_2)^2 + (J_3\omega_{3n} - J_3\omega_3)^2}}$$

where ω_{in} are the programmed values of angular velocities for next segment of free motion (for new hitting trajectory); t_n is instant of n-th correction; Δt_n is duration of n-th correction impulse.

Braking of a spacecraft requires some time and spacecraft rotates around angular momentum **L**; the remaining angle φ_{rem} (for a turn around angular momentum from current position Λ into position Λ_{f}) and angle of spacecraft s rotation around vector **L** of angular momentum for time of braking φ_{br} have the following values (because modulus of angular momentum is changed linearly):

$$\varphi_{\text{rem}} = 2\arcsin\frac{K\sqrt{\delta_2^2 + \delta_3^2}}{\sqrt{(J_2\omega_2)^2 + (J_3\omega_3)^2}} ,$$

$$\varphi_{\text{br}} = \frac{K^2\sqrt{\omega_2^2 + \omega_3^2}}{2m_0\sqrt{(J_2\omega_2)^2 + (J_3\omega_3)^2}}$$

The remaining angle φ_{rem} is determined by relative orientation of current attitude Λ and the required final position Λ_{f} (for this purpose, we calculate quaternion of mismatch $\widetilde{\Lambda}(t)\circ\Lambda_{\text{f}}$). Angle φ_{br} required for damping of angular momentum is determined by spacecraft s angular velocity. Variation of angles φ_{rem} and φ_{br} is shown in Figure 6. We begin a braking of a spacecraft when angles φ_{rem} and φ_{br} is identical (and difference $\Delta\varphi = \varphi_{\text{rem}} - \varphi_{\text{br}}$ is zero). If braking begin earlier, then spacecraft will not be moved to the required angular position Λ_{f} (spacecraft will stop before the required position Λ_{f} and not reach position Λ_{f} when rotation will end). If braking begin later, then spacecraft's angular velocity will be distinct from zero at the moment of achievement of angular orientation Λ_{f}. Deviation $\Delta\varphi$ is changed in accordance with Figure 7. At segment of braking, $\varphi_{\text{rem}} \approx \varphi_{\text{br}}$. It means that, at any instant within phase of braking, spacecraft can be turned through angle φ_{rem} during the remaining time of suppressing angular velocity up to zero; on the other hand, at any instant within phase of braking, spacecraft can be stopped to $\boldsymbol{\omega}$=0 during a turn through the angle φ_{rem} (i.e. final position Λ_{f} will be achieved when $\boldsymbol{\omega}$=0). Error of reorientation is $\sigma = 0.11$ degrees (accuracy depends on the acting disturbance moments - gravitational and aerodynamic moments - and due to inequality of transverse moments of inertia J_2 and J_3). Notice, angles ψ_{f} and $\psi_{\text{sub}} = |\boldsymbol{\omega}||\mathbf{L}|/(2m_0)$ is changed in accordance with the Figure 8.

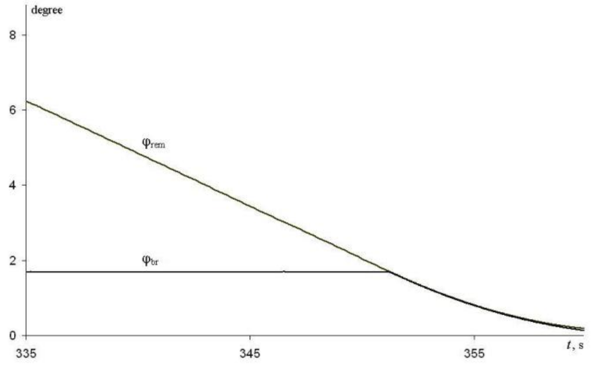

Figure 6. Variation of angles φ_{rem} and φ_{br} in ending of optimal turn

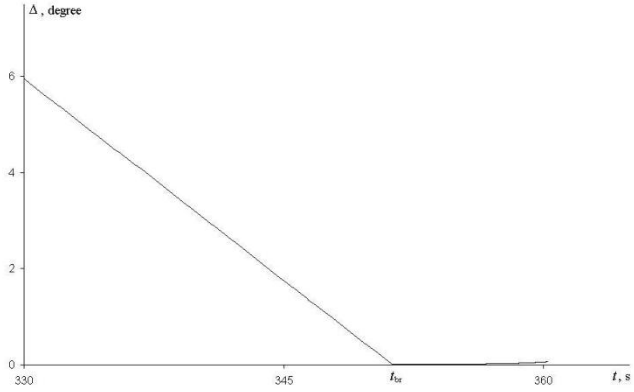

Figure 7. Character of deviation $\Delta\varphi$ before instant of beginning of braking and after it

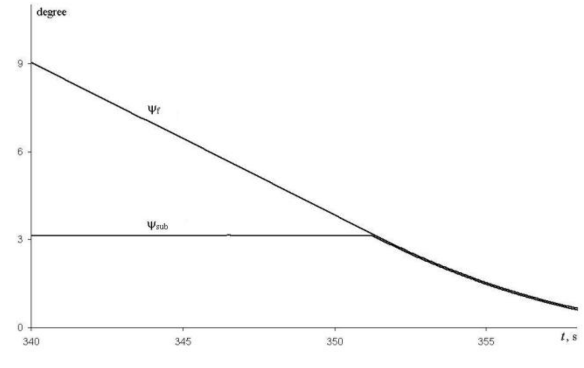

Figure 8. Angles ψ_{f} and ψ_{sub} before instant of beginning of braking and after it

DOI: https://doi.org/10.30564/jmer.v4i2.3725

Important characteristics of control are value of index (3) and accuracy of reorientation into the given final position. They were computed by mathematical simulation. Set of numerical experiments with modeling of spacecraft's rotation process was made. Ratings of control laws and estimates of efficiency of the designed control algorithms (precision of reorientation, and energy-saving efficiency) were calculated for each rotation maneuver in this series. Input data (original parameters of maneuvers - initial and final attitudes, spacecraft's inertial characteristics, and duration of rotation) were identical. Average modulus of angular rate during the rotary maneuvers is 0.5 deg/s. Estimates of fuel expenditure G and error of final attitude σ determined as result of the numerical simulations were: $G = 5.60$ kg with attitude accuracy $\sigma \approx 0.1°$ correspond to iterative control by the method of guidance by a required velocity (without prediction of position at instant of first correction), and $G = 5.55$ kg with attitude accuracy $\sigma < 0.08°$ correspond to mode of iterative guidance with prediction of position at instant of first correction. Also, for comparison, we cite values of same indicators of efficiency for same spacecraft which were specified after realizations of rotary maneuvers carried out according to mode of extensive rotation and rotation in form of regular precession (simultaneous rotation about longitudinal axis and about fixed transversal axis): $G\text{ex} = 7.02$ kg and $G\text{reg} = 6.13$ kg.

With help of mathematical modeling, for each method, we obtain statistical estimates of fuel consumption for one turn. They confirmed optimality of the designed control, which takes into account action of external moments of disturbance. Results of mathematical modeling demonstrate that the suggested methods of execution of the programmed turns improve accuracy of reorientation, given relatively large parametric undeterminacies and external perturbations. Moreover, "price" paid for absence of exact a priori information concerning dynamic characteristics of a spacecraft (some degradation of quality's index) is not too large. Let us note that traditional methods of optimal control not only require much more computational expenditure, but lead to greater fuel consumption with respect to control as well.

7. Conclusions

In this research, new control method of spacecraft attitude is presented. Example and results of mathematical simulation for spacecraft rotation under optimal control are given. The obtained results demonstrate that the designed control method of spacecraft's three-dimensional reorientation is feasible in practice.

Rotary maneuver is one of basic dynamic regimes of motion control system. It was topical problem to design optimal algorithm of attitude control and to calculate numerical index of control efficiency. It seems impossible to solve the problem of slew maneuver of asymmetric spacecraft with minimal expense of fuel, taking into account disturbances (gravitational and aerodynamic torques). Algorithm of numerical constructing the control that satisfies all necessary requirements is suggested. It is limited in magnitude, ensures minimal consumption of fuel, and satisfies the given accuracy of attitude. Available mathematical model of spacecraft motion with respect to center of mass allowed us to use mode of guidance by a required velocity with prognostic model to form optimal control of attitude and to get its implementation. We know two-impulse control which rotate spacecraft along attitude trajectory consisting of three phases: fast imparting the required angular momentum to spacecraft's body with maximal control torque, free rotation without control torque, and quickest damping of rotation with maximal modulus of control torque. Each phase satisfies conditions of optimality: phase of free rotation fits condition of optimality, because there is no expenditure of fuel during it; phases of acceleration and braking also fit criterion of optimality, because minimal expenditure of fuel for acceleration and damping of rotation is determined only by the imparted angular momentum (which in turn is determined by inertial characteristics of a spacecraft, by initial and final conditions, and by duration of maneuver T). But error of reorientation can be unacceptable if external disturbing moments act long time (or angle of turn is large).

For improving the precision of attitude in the required position, one needs to control spacecraft's angular momentum in process of maneuver, using actual parameters of attitude. We present effective algorithms of controlling the reorientation, which are invariant under external disturbances and parametric discrepancy of model. Very effective mode is iteration control at which correction of rotation is carried out impulsively, at discrete instants of time. This mode ensures the required precision of attitude without refusal of control by method of free trajectories. Control commands are formed such that attitude actuators change angular momentum of a spacecraft not continuously, as at known methods, but impulsively at discrete instants of time. Since exact values of parameters of model of spacecraft rotation (e.g., moments of inertia) a priori are not known (they are known only roughly), to simplify onboard algorithms when angular rates are computed for points of beginning the uncontrolled phases, spacecraft is assumed dynamically symmetric body. The developed control laws are free from following typical simplifications: field of possible values of control torques is not closed; the minimized index is quadratic function; there is constraint on angle of turn; spacecraft is dynamically symmetric about longitudinal axis; and finally, perturbation torques are neglected.

We give numerical estimates of fuel expense for implementation of rotary maneuver according to control modes which are presented above. Mathematical simulation allowed us to find values of fuel saving in performance of the described control laws for spacecraft's rotary maneuvers (in particular, for module of orbital station). Numerical modeling has shown that control which realize method of free trajectory with accounting for aerodynamic and gravitational models is sufficiently efficient and close to optimal solution. New control modes allow one to achieve considerable economy of fuel expense as compared to the known methods of control that is important for practice of spaceflight. In addition, these algorithms can be applied using modern onboard systems. The designed control methods of three-dimensional attitude allow expense of fuel for turn of existing spacecraft to be decreased by 20% - 30%. Estimates of fuel-saving efficiency of the presented modes of spacecraft attitude were calculated by statistical methods using numerical simulation in computer. Specific peculiarity of mathematical model of spacecraft rotation accepted in this paper for calculating the estimates of accuracy and fuel consumption is assumption about presence of significant aerodynamic and gravitational torques acting upon body of a spacecraft.

Notice, recent solutions [19-22] are not applicable for general case of three-dimensional turn of arbitrary spacecraft; the work [25] describes synthesis of terminal reorientation control only for spacecraft which moves along circular orbit. But method designed in present article is universal control, it does not depend on a ratio (proportion) of moments of inertia or final position of a spacecraft.

Acknowledgement

No financial exists.

Conflicts of Interest

No conflicts of interest exist.

References

[1] Branets, V.N., Shmyglevskii, I.P., *Use of Quaternions in Problems of Orientation of Solid Bodies*, Nauka, Moscow, 1973. [in Russian]

[2] Razorenov, G.N., Bakhramov, E.A., Titov, Yu.F., Control systems of flight vehicle (ballistic rockets and their head parts), Mashinosrtoenie, Moscow, 2003. [in Russian]

[3] Steven Parsons, Planet Discovered Transiting a Dead Star, *Nature*, 585(7825), 2020, 354-355.

[4] Eliza Kempton., First Exoplanet Found around a Sun-like Star, *Nature*, 575(7784), 2019, 43-44.

[5] Kelley C. Wells, Dylan B. Millet & Jose D. Fuentes., Satellite Isoprene Retrievals Constrain Emissions and Atmospheric Oxidation, *Nature*, 585(7824), 2020, 225-233.

[6] Raushenbakh, B.V., Tokar, E.N., *Spacecraft Orientation Control*, Nauka, Moscow, 1974. [in Russian]

[7] Alekseev, K.B., Malyavin, A.A., Shadyan, A.V., Extensive Control of Spacecraft Orientation Based on Fuzzy Logic, *Flight*, No. 1, 2009, 47-53. [in Russian]

[8] Velishchanskii, M. A., Krishchenko, A. P., Tkachev, S. B., Synthesis of Spacecraft Reorientation Algorithms Using the Concept of the Inverse Dynamic Problem, *Journal of Computer and System Sciences International*, 42(5), 2003, 811-818.

[9] Ermoshina, O.V., Krishchenko, A.P., Synthesis of Programmed Controls of Spacecraft Orientation by the Method of Inverse Problem of Dynamics, *Journal of Computer and Systems Sciences International*, 39(2), 2000, 313-320.

[10] Junkins, J. L., Turner, J. D., *Optimal Spacecraft Rotational Maneuvers*, Elsevier, Amsterdam, 1986.

[11] Levskii, M.V., On Optimal Spacecraft Damping, *Journal of Computer and System Sciences International*, 50(1), 2011, 144-157.

[12] Levskii, M. V., Pontryagin's Maximum Principle in Optimal Control Problems of Orientation of a Spacecraft, *Journal of Computer and System Sciences International*, 47(6), 2008, 974-986.

[13] Reshmin, S.A., Threshold Absolute Value of a Relay Control when Time-optimally Bringing a Satellite to a Gravitationally Stable Position, *Journal of Computer and Systems Sciences International*, 57(5), 2018, 713-722.

[14] Reshmin, S.A., The threshold Absolute Value of a Relay Control Bringing a Satellite to a Gravitationally Stable Position in Optimal Time, *Doklady Physics*, 63(6), 2018, 257-261.

[15] Li, F., Bainum, P.M., Numerical Approach for Solving Rigid Spacecraft Minimum Time Attitude Maneuvers, *Journal of Guidance, Control, and Dynamics*, 13(1), 1990, 38-45.

[16] Byers, R., Vadali, S., Quasi-closed-form Solution to the Time-optimal Rigid Spacecraft Reorientation Problem, *Journal of Guidance, Control, and Dynamics*, 16(3),1993, 453-461.

[17] Scrivener, S., Thompson, R., Survey of Time-optimal Attitude Maneuvers, *Journal of Guidance, Control, and Dynamics*, 17(2), 1994, 225-233.

[18] Liu, S., Singh, T., Fuel/time Optimal Control of Spacecraft Maneuvers, *Journal of Guidance*, 20(2), 1996, 394-397.

[19] Shen, H., Tsiotras, P., Time-optimal Control of Axi-symmetric Rigid Spacecraft with Two Controls, *Journal of Guidance, Control, and Dynamics*, 22(5), 1999, 682-694.

[20] Molodenkov, A. V., Sapunkov, Ya. G., Analytical Solution of the Minimum Time Slew maneuver Problem for an Axially Symmetric Spacecraft in the Class of Conical Motions, *Journal of Computer and Systems Sciences International*, 57(2), 2018, 302-318.

[21] Molodenkov, A. V., Sapunkov, Ya. G., A solution of the Optimal Turn Problem of an Axially Symmetric Spacecraft with Bounded and Pulse Control under Arbitrary Boundary Conditions, *Journal of Computer and System Sciences International*, 46(2), 2007, 310-323.

[22] Molodenkov A. V., Sapunkov Ya. G. Analytical Quasi-Optimal Solution of the Slew Problem for an Axially Symmetric Rigid Body with a Combined Performance Index, *Journal of Computer and System Sciences International*, 59(3), 2020, 347-357.

[23] Levskii, M.V., Optimal Control of a Programmed Turn of a Spacecraft, *Cosmic Research*, 41(2), 2003, 178-192.

[24] Levskii, M.V., Optimal Spacecraft Terminal Attitude Control Synthesis by the Quaternion Method, *Mechanics of Solids*, 44(2), 2009, 169-183.

[25] Zubov, N.E., Li, M.V., Mikrin, E.A., Ryabchenko, V.N.,Terminal Synthesis of Orbital Orientation for a Spacecraft, *Journal of Computer and Systems Sciences International*, 56(4), 2017, 721-737.

[26] Levskii, M.V., On Improving the Maneuverability of a Space Vehicle Managed by Inertial Executive Bodies, *Journal of Computer and Systems Sciences International*, 59(5), 2020, 796-815.

[27] Kovtun, V.S., Mitrikas, V.V., Platonov, V.N., Revnivykh, S.G., Sukhanov, N.A., Mathematical Support for Conducting Experiments with Attitude Control of Space Astrophysical Module Gamma, *News from Academy of Sciences USSR. Technical Cybernetics*, 1990, No. 3, 144-157. [in Russian]

[28] Levskii, M.V., Special Aspects in Attitude Control of a Spacecraft, Equipped with Inertial Actuators, *Journal of Computer Science Applications and Information Technology*, 2(4), 2017, 1-9.

[29] Levskii, M.V. RF Patent No. 2076833, 1997. [in Russian]

[30] Levskii, M.V. RF Patent No. 2146638, 2000. [in Russian]

DOI: https://doi.org/10.30564/jmer.v4i2.3725

BILINGUAL PUBLISHING CO.
Pioneer of Global Academics Since 1984

Journal of Mechanical Engineering Research
https://ojs.bilpublishing.com/index.php/jmer

ARTICLE

Geometrical Dimensional Effect on Natural Frequency of Single Layer Graphene in Armchair Configuration

Harshad Patel[*]

Manufacturing Engineering Department, Central Institute of Petrochemicals Engineering & Technology, Ahmedabad, Gujarat, India

ARTICLE INFO

Article history
Received: 14 October 2021
Revised: 1 November 2021
Accepted: 12 November 2021
Published Online: 18 November 2021

Keywords:
Single layer graphene sheet (SLGS)
Size variation
Fundamental natural frequency
Finite element analysis

ABSTRACT

Graphene has remarkable strength, such as yield strength and elastic constant. The dynamic behaviour of graphene sheet is affected by geometrical variation in atomic arrangement. This paper introduced graphene with armchair atomic structure for estimating fundamental natural frequencies. The presented analysis can be useful for the possible high frequency nanomechanical resonator systems. The analytical formulation, based on classical plate theory and continuum solid modelling based finite element method have been performed for estimation of fundamental natural frequencies of single layer graphene sheet (SGLS) with different boundary conditions. The free edge and clamped edge boundary conditions have been considered. For simplifying analytical formulations, Blevins approach for dynamic solution has been adopted and for validating analytical results. The finite element analysis of SLGS has been performed using ANSYS software. The effect of variation in geometrical parameters in terms of width and length of SLGS has been analysed for realization of ultra-high frequency based nanomechanical resonator systems.

1. Introduction

There are many discoveries for nano structures have been found in which, graphene is the most predominant invention of the engineering science. And till date many broad range of innovation are appraised for exploring the properties such as thermal, electrical, and mechanical of graphene as a nanostructure [1,2]. There are several allotropes, investigated based on carbon in which different phenomenon such as 3-dimensional, 2-dimenionsal and 1-dimensional allotropes were identified as graphite, graphene and nanotube respectively [3-7]. In the structure of graphene, carbon atoms are bonded very densely as honeycomb arrangement with sp2 bond. Graphene has excellent material properties, which attracts the field of application such as nanoelectronic, bio mechanical, nano sensing element, resonators etc [8,9]. In the recent years, grapheme has been placed as stronger material in the field of material engineering due to its stunning material properties such as electrical, thermal, and chemical [10,11]. Properties such as mobility of electron at room temperature as 250000 cm^2/Vs, thermal conductivity 5000 W/mK [12], explored surface area as 2630 m^2/g [13] made it versatile in the today's era.

Numerous researches on single layer graphene sheet have been done, which employ static and dynamic phenomenon such as static behaviors, fatigue and vibration

---

**Corresponding Author:*
Harshad Patel,
Manufacturing Engineering Department, Central Institute of Petrochemicals Engineering & Technology, Ahmedabad, Gujarat, India;
Email: patel.harshad0585@gmail.com

DOI: https://doi.org/10.30564/jmer.v4i2.3831

behaviors. [14,15]. For example, Sakhaee et al. [16] had performed molecular structural mechanics and reported that single layer graphene sheet has remarkable dynamic behaviors. There are many technical phenomenon are completed on graphene for cultivating comprehension of behaviors of graphene with different boundary conditions such as clamped-pinned with mass, Clamped-pinned without mass etc [17]. Moreover, there are many technical aspects which are not explored yet by researchers in the field of material engineering that can distinguish the dynamic approach. Various boundary conditions and support conditions with different theories such as molecular dynamic theory, computational approaches etc. are still in consideration for investigation [18,19].

Graphene has principal applications in the field of biomechanical as sensor or in nanomechanical system as mass sensor [20]. The system based on graphene may have higher sensitivity as a mass sensor for monitoring resonance frequency. In the structural applications, aeronautical applications, automobile sectors, there are various aspects of graphene or graphene based composite material utilization, which can add noticeable advantages in terms of static and dynamic strength [21]. The atomic structures of graphene can be classified as armchair, zigzag and chiral and different types atomic structure of graphene affect significantly to the graphene's behaviors in static and dynamic condition. In the armchair atomic structure, at the free edges along width of graphene sheet carbon-carbon bond of each hexagon are parallel to lateral dimensions as width of graphene sheet. When large portion of graphene is cut along sides of hexagons, then armchair structure is obtained [22]. In the zigzag atomic structure, at the free edges along width of graphene sheet carbon-carbon bond of each hexagon are 60 degrees offset to the axis of width of graphene sheet. When large graphene sheet is cut along sides the vertices of hexagons, then zigzag structure is obtained [22,23].

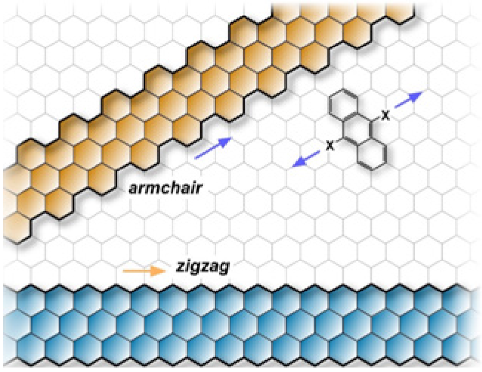

Figure 1. Direction of cutting graphene sheet to obtain armchair and zigzag structure [22]

2. Analysis Approach

In this research work, graphene sheet is simulated by employing three different approaches said, analytical, finite element analysis, and space frame modeling approach. The analytical approach has been employed for obtaining results based on analytical formulations, the obtained results are validated using continuum modeling based finite element analysis using ANSYS workbench.

2.1 Analytical Approach

The analytical formulation of the graphene sheet with armchair configuration has been performed by considering graphene sheet as a rectangular plate like structure. The classical plate theory based on Kirchoff theory for thin plate has been applied on the graphene sheet. Assumption further extended towards single layer of rectangular plate; as graphene sheet is a two-dimensional atomic structure. The thickness has been considered as diameter of carbon atom. The equation of motion has been derived by employing equilibrium approach of solution. And, the natural frequencies are obtained based on Blevins solution for dynamic approach.

There are two motions in the concept of vibration phenomenon, which are important to technical point of view; known as transverse and longitudinal, and both are to be considered for understanding deformation in each direction. Deformation in specific direction decides stress level in particular direction as per boundary and support conditions so fundamental mode shape with natural frequency is become an important aspect of study. In this study, analytical calculation is executed by considering transverse direction only and Blevins solution of natural frequency is employed. As per equilibrium approach, equation of motion can be derived as,

$$D\left(\frac{\partial^4 w}{\partial^4 x}+2\,\frac{\partial^4 w}{\partial^2 x * \partial^2 y}+\frac{\partial^4 w}{\partial^4 y}\right)+\rho h\frac{\partial^2 w}{\partial t^2}=0 \tag{1}$$

Now, considering no deformation at two adjacent sides, x = 0, y = 0. And considering free vibration, i.e. force = 0, solution of equation (1) is given by,

$$\begin{gathered} W(x,y) = a1\sin\alpha x\sin\beta y + a2\sin\alpha x\cos\beta y + \\ a4\cos\alpha x\cos\beta y + a5\sinh\theta x\sinh\varnothing y \\ + a6\sinh\theta x\cosh\varnothing y + a7\cosh\theta x\sinh\varnothing y + \\ a8\cosh\theta x\cosh\varnothing y \end{gathered}$$

Where, $\lambda 2 = \alpha 2 + \beta 2 = \theta 2 + \varnothing 2$

Blevins had derived various dynamic solutions considering numerous boundary conditions such as bridge boundary, cantilever boundary condition etc. Bridge boundary condition is set by clamping two opposite edges and by keeping two free edges whereas cantilever has

DOI: https://doi.org/10.30564/jmer.v4i2.3831

one clamped edge and three free edges [24,25]. Based on mentioned boundary conditions, Blevins had developed various constants as per mode index, which are mentioned below,

$$\omega_{ij} = \sqrt{\left\{\frac{\pi^4 F}{a^4 h\rho}\right\}\left\{H_x{}^4 + H_y{}^4\left(\frac{a}{b}\right)^4 + 2\left(\frac{a}{b}\right)^4\left[\vartheta J_x J_y + (1-\vartheta)K_x K_y\right]\right\}} \quad (2)$$

Where, $F, Flexural\ Density = \frac{Eh^3}{12(1-\vartheta^2)}$

H*x*, *Jx*, *Kx*, *Hy*, *Jy*, *Ky*; all are constants depend on boundary conditions.

Table 1. Edges along Length (Free-Free boundary)

Mode index (j)	Hy	Jy	Ky
1	0	0	0
2	0	0	1.22
3	1.51	1.25	5.017

Table 2. Edges along Length (Clamped-Clamped boundary)

Mode index (j)	Hx	Jx	Kx
1	1.51	1.29	1.25
2	2.5	4.658	4.658
3	3.5	10.02	10.02

Table 3. Edges along Length (Clamped-Free boundary)

Mode index (j)	Hx	Jx	Kx
1	0.597	-0.0870	0.471
2	1.494	1.347	3.284
3	2.5	4.658	7.842

Consider (5,5) armchair configuration for length 10A of the graphene.

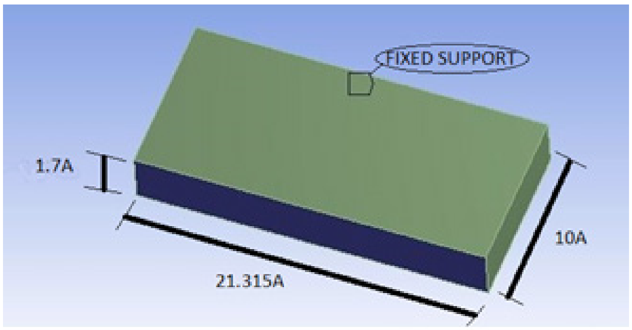

Figure 2. General Dimensions of the Model

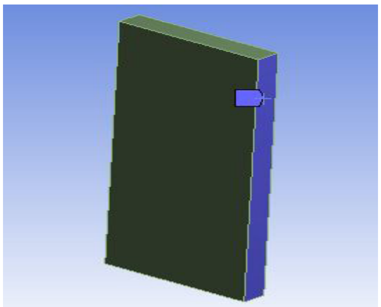

Figure 3. Free-Free-Free-Clamp (F-F-F-C) Boundary Condition (FEM)

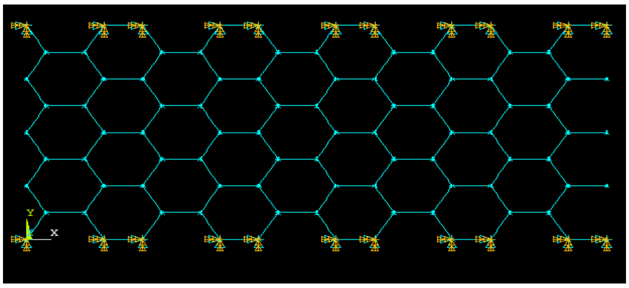

Figure 4. Free-Free-Clamp-Clamp (F-F-C-C) Boundary Condition (SFA)

In general, two major boundary conditions are considered such as bridge boundary condition and cantilever boundary conditions. Bridge boundary condition is defined as Free-Free-Clamp-Clamp (F-F-C-C) whereas cantilever boundary condition is defined as Free-Free-Free-Clamp (F-F-F-C). In bridge boundary condition opposite sides of the Graphene was fixed and two sides are remaining free whereas in cantilever boundary condition three sides of the Graphene remain free and one is fixed.

This concept is applied to all three approaches, numerical, finite element analysis and finite element analysis (Space Frame Analysis). In numerical approach, boundary conditions with constants are presented in Table 1, 2 & 3 through which analytical calculation is carried out for all armchair dimensions whereas FEA and FEA (SFA) are presented as per the below models created in ANSYS modeler and ANSYS APDL.

Now from above tables, constants for bridge boundary condition are decided as,

$\omega_{11} as$ Hx = 1.506, Jx = 1.248, Kx = 1.248,
Hy = 0, Jy = 0, Ky = 0
$\omega_{12} as$ Hx = 2.5, Jx = 4.658, Kx = 4.658, Hy = 0,
Jy = 0, Ky = 0

The one of the basic calculations of (5,5) armchair patter of graphene is derived here as,

DOI: https://doi.org/10.30564/jmer.v4i2.3831

$$\text{Flexural rigidity}\,(F) = \frac{E * h^3}{12 * (1-\vartheta^2)} = \frac{10^{12} \times (3.45 \times 10^{-10})^3}{12(1-0.456^2)}$$

$$= 4.320 * 10^{-18}\text{N.m}$$

$$\omega_{11} = \sqrt{\left\{\frac{\pi^4 * 4.3203 * 10^{-18}}{(10^{-9})^4 * 1161 * 1.7 * 10-10}\right\}\left\{\begin{matrix} 1.506^4 + 0^4\left(\frac{1}{2.13151}\right)^4 + 2\left(\frac{1}{2.13151}\right)^4 \\ \times\,[0.456 * 1.248 * 0 + (1-0.456)1.248 * 0] \end{matrix}\right\}}$$

$= 6.62*10^{12}$Hz

$$\omega_{12} = \sqrt{\left\{\frac{\pi^4 * 4.3203 * 10^{-18}}{(10^{-9})^4 * 1161 * 1.7 * 10-10}\right\}\left\{\begin{matrix} 2.5^4 + 0^4\left(\frac{1}{2.13151}\right)^4 + 2\left(\frac{1}{2.13151}\right)^4 \\ \times\,[0.456 * 4.658 * 0 + (1-0.456)1.248 * 0] \end{matrix}\right\}}$$

$= 6.73*10^{12}$ Hz

2.2 Finite Element Analysis

Continuum finite element method based approach of graphene sheet has been performed in ANSYS workbench for various configuration such as (11,11), (15,15), and (19,19). All the configuration are simulated using ANSYS workbench with bridge and cantilever boundary conditions. Dimensions of graphene sheet configuration was set as 10 x 21.31 Å with thickness of graphene as 170 Å which is diameter of carbon atom. For continuum solid modeling based finite element analysis approach, all the configurations have been simulated as per bridge and cantilever boundary conditions with different length of graphene sheet.

Table 4. Properties of Graphene.

Sr. No.	Property	Value
1	Poisons ratio u	0.456
2	Density ρ	1161Kg/m^3
3	Young's modulus E	1 TPa=10^{12} Pa

Table 5. Geometrical Dimension of Graphene.

Sr. No.	Dimensions	Value
1	length of graphene sheet, *a*	10A =10^{-9} m
2	Width, *b*	21.315A=2.1315 x10^{-9} m
3	Thickness	0.17nm =1.7 x10^{-10} m

2.3 Space Frame Approach (FEA)

Space frame approach is advanced version of FEM based nodal calculation and for getting the advantage of this, ANSYS APDL is employed in the analysis. In ANSYS APDL all the coordinated are deployed from the Nano modeler software and file is exported in ANSYS APDL.Graphene sheet has hexagonal arrangement of atoms such as honey comb structure [26,27]. Results obtained, using continuum solid modeling approach has been validated by performing space frame modeling approach using ANSYS APDL. The development of space frame model of graphene sheet in ANSYS APDL requires the co-ordinates of all the atoms of carbon to represent approximation of single layer graphene sheet. The space frame models of (11,11) configuration has shown in Figure 3, which is developed using ANSYS APDL. Similarly, the space frame model of atomic structures (15,15) and (19,19) have been developed.

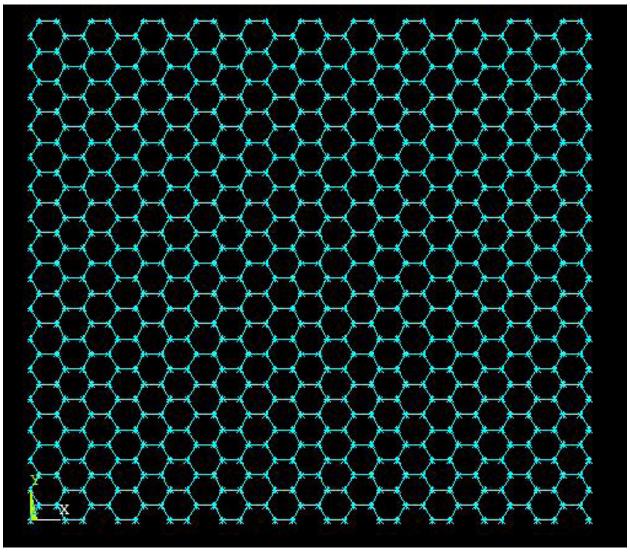

Figure 5. Space Frame of (11, 11) configuration

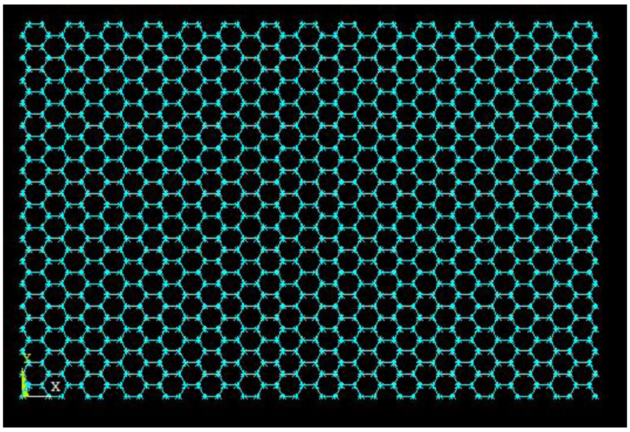

Figure 6. Space Frame of (15, 15) configuration

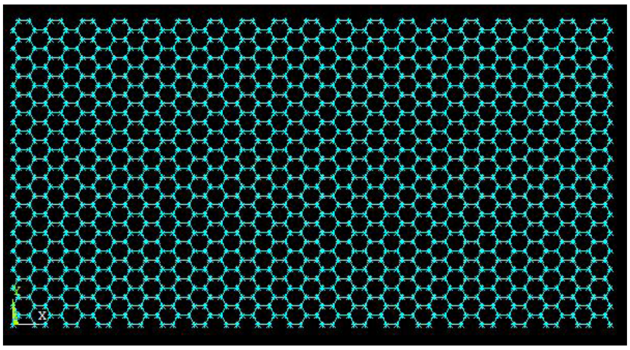

Figure 7. Space Frame of (19, 19) configuration

DOI: https://doi.org/10.30564/jmer.v4i2.3831

3. Results & Discussion

Single layer graphene sheet has been analyzed by three approaches as, analytically, finite element analysis, and finite element analysis with space frame approach. The analysis has been performed with different lengths of the graphene as 41.21A, 83.83A, 126.46A, 169.08A, and 211.71A, for three different widths of 12.31A, 17.23A, and 22.15A of the graphene sheet. The obtained results for bridged and cantilevered configurations are summarised in Table 6 and Table 7 respectively for all the considered approaches.

Table 6. Comparison of Natural Frequency (Bridge Boundary Condition)

Configuration (Armchair)	Width	Length	Analytical (GHz)	FEA (GHz)	FEA(SFA) (GHz)
(11,11)	12.31A	41.21A	669	599	600
		83.83A	162	147	154
		126.46A	71	64.5	66.1
		169.08A	39.7	36.0	38.1
		211.71A	25.3	22.9	24.1
(15,15)	17.23A	41.21A	668	607	632
		83.83A	160	149	158
		126.46A	70	65.2	70.4
		169.08A	39	36.3	38.0
		211.71A	25	23.1	23.9
(19,19)	22.15A	41.21A	665	612	655
		83.83A	158	150	162
		126.46A	68	65.7	68.9
		169.08A	39	36.6	38.7
		211.71A	25	23.2	30.0

Table 7. Comparison of Natural Frequency (Cantilever Boundary Condition)

Configuration (Armchair)	Width	Length	Analytical (GHz)	FEA (GHz)	FEA(SFA) (GHz)
(11,11)	12.31A	41.21A	105	96.1	93.0
		83.83A	25.4	23.0	24.2
		126.46A	11.2	10.1	10.6
		169.08A	6.24	5.61	5.96
		211.71A	3.98	3.57	3.20
(15,15)	17.23A	41.21A	106	97.4	98.0
		83.83A	25.9	23.2	24.9
		126.46A	12.0	10.1	9.10
		169.08A	6.52	5.64	5.50
		211.71A	4.10	3.59	3.91
(19,19)	22.15A	41.21A	106.5	98.5	106
		83.83A	26.0	23.3	29.8
		126.46A	12.1	10.2	10.4
		169.08A	6.72	5.66	6.60
		211.71A	4.19	3.60	4.25

3.1 Bridge Boundary Condition

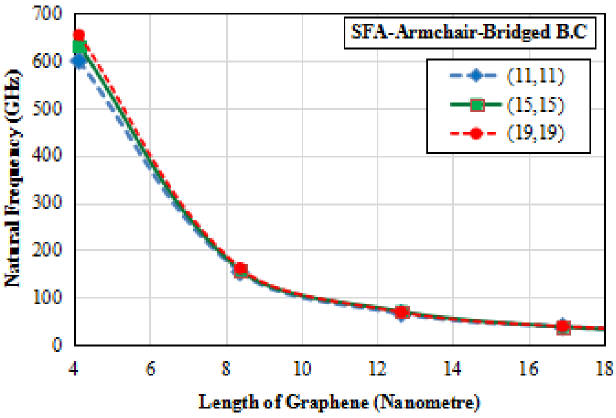

Figure 8. Variation of Natural Frequency in Bridged Boundary Condition

In armchair atomic configuration of graphene sheet, for bridge boundary condition obtained results shows that, the maximum natural frequency for (19, 19) is 655 GHz, whereas for (11, 11) armchair configuration the maximum natural frequency is 601 GHz. From Figure 8, it has been observed that, as the length of graphene sheet increases the natural frequencies decreases irrespective of configuration of (19, 19), (15,15), and (11,11).

3.2 Cantilever Boundary Condition

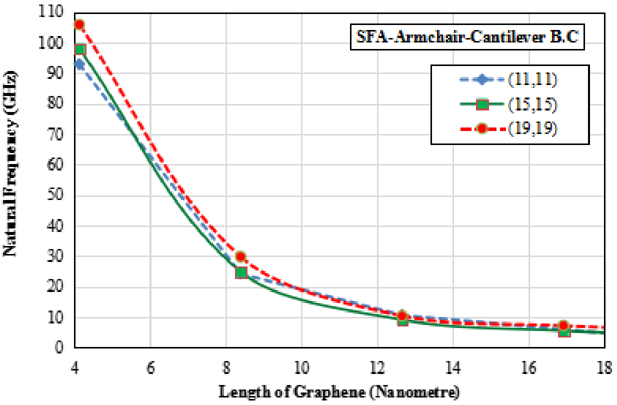

Figure 9. Variation of Natural Frequency in Cantilever Boundary Condition

For cantilevered configuration obtained results (Table 7) also depicts that as the length of graphene sheet increases the natural frequency decreases irrespective of different considered armchair configurations. Also, it has been observed that for the same size frequency of graphene sheet for bridged boundary condition is higher than that for the cantilevered boundary condition (Figure 9). Such results suggest that cantilevered boundary condition is more sensitive than that of bridged boundary condition.

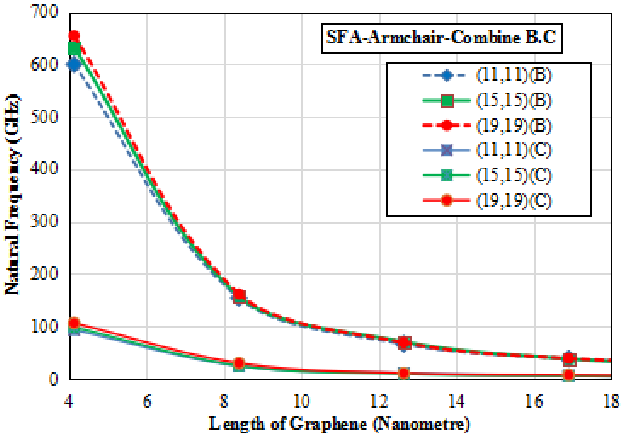

Figure 10. Variation of Natural Frequency in Bridged & Cantilever Boundary Condition

4. Conclusions

The present research work on Graphene was introduced for identification of dynamic behaviours based on analysis of natural frequency variation. Size variation of graphene sheet is carried out by performing modal analysis in finite element analysis and FEA space frame approach in ANSYS APDL and found to be useful for further realization of ultra-high frequency nanomechanical resonators. The present analysis also suggests that as the size of the graphene sheet increases (either width or length) the natural frequencies of graphene sheet decreases. Also, it has been observed that for a particular size of graphene sheet the natural frequency is found higher for bridged boundary condition compared to cantilevered boundary condition in armchair configuration. Such results depict that cantilevered boundary condition is found more sensitive compared to bridged boundary condition the armchair configuration. It has been observed that outcome from the research work is resembled in all analysis domains such as numerical, finite element method, and finite element analysis in space frame approach for natural frequency so the reliability of the space frame approach and finite element analysis can be carried out to nano size of the plate said as for Graphene. The presented analysis is found to be useful for the realization of high frequency sensor system based on nanomechanical resonator, which can be utilized as a mass sensor, gas-sensor, bio-detection sensor system etc.

References

[1] S. Iijima // *Nature* 354 (6348) (1991) 56.

[2] K. Esumi, M. Ishigami, A. Nakajima, K. Sawada, H. Honda // *Carbon* 34 (1996) 279.

[3] F. Scarpa, S. Adhikari, A. Srikantha Phani // *Nanotechnology* 20(6) (2009) 065709.

[4] K. Tanaka, H. Aoki, H. Ago, T. Yamabe, K. Okahara // *Carbon* 35 (1997) 121.

[5] M. Kim, H.S. An, W.-J. Lee, J. Jung // *Electronic Materials Letters* 9(4) (2013) 517.

[6] M. Mazar Atabaki, R. Kovacevic // *Electronic Materials Letters* 9(2) (2013) 133.

[7] W.G. Lee, E. Kim, J. Jung // *Electronic Materials Letters* 8(6) (2012) 609.

[8] C. Berger, Z. Song, T. Li, X. Li, A.Y. Ogbazghi, R. Feng, Z. Dai, A.N. Marchenkov, E.H. Conrad, P.N. First, W.A. de Heer // *The Journal of Physical Chemistry B* 108(52) (2004) 19912.

[9] J.S. Bunch, A.M. Van Der Zande, S.S. Verbridge, I.W. Frank, D.M. Tanenbaum, J.M. Parpia, H.G. Craighead, P.L. McEuen // *Science* 315 (2007) 490.

[10] S.S. Gupta, R.C. Batra, Journal of Computational and Theoretical Nanoscience 7 (10) (2010) 2151-2164.

[11] S. Timoshenko, Theory of Plates and Shells, McGraw-Hill, Inc, London, 1940.

[12] Balandin AA, Ghosh S, Bao W, Calizon I, Teweldebrhan D, Miao F, et al. Superior thermal conductivity og single-layer graphene. Nano Lett 2008;8(3):902-7.

[13] Zhu Y, Murali S, Cai W, Li , Suk JW, Potts JR, et al. Graphene and graphene oxide: synthesis, properties, and application. Adc Mater 2010;22(35):3906-24.

[14] Jena, Subrat & Chakraverty, S.. (2019). Dynamic Analysis of Single-Layered Graphene Nano-Ribbons (SLGNRs) with Variable Cross-Section Resting on Elastic Foundation. Curved and Layered Structures. 6. 132-145. 10.1515/cls-2019-0011.

[15] Ren Wei Jiang, Zhi Bin Shen, Guo Jin Tang, Vibration analysis of a single-layered graphene sheet-based mass sensor using the Galerkin strip distributed transfer function method, 2016.

[16] A. Sakhaee-Pour, M.T. Ahmadian, A. Vafai // *Solid State Communications* 145 (2008) 168.

[17] Laura, P.A.A.; Pombo, J. L.; Susemihl, E.A. A note on the vibration of a clamped free beam with a mass at the free end. J. Sound Vib. 1974, 37, 161-168.

[18] Natsuki, Toshiaki. (2015). Theoretical Analysis of Vibration Frequency of Graphene Sheets Used as Nanomechanical Mass Sensor. Electronics. 4. 723-738. 10.3390/electronics4040723.

[19] Samaei, A.T. & Aliha, M.R.M. & Mirsayar, M.M.. (2015). Frequency analysis of a graphene sheet embedded in an elastic medium with consideration of small scale. Materials Physics and Mechanics. 22. 125-135.

[20] Ekinci, K.L.; Huang, X.M.H.; Roukes, M.L. Ultrasensitive nanoelectromechanical mass detection.

DOI: https://doi.org/10.30564/jmer.v4i2.3831

Appl. Phys. Lett. 2004, 84, 4469-4471.

[21] Geim, A.K. Graphene: status and prospects. Science 2009, 324, 1530-1534.

[22] Rakesh Prabhu T., Tarapada Roy, National Institute Of Technology ROURKELA,2010.Finite element modelling of multiwall carbon nanotube.

[23] Steven J. Koester ,Ultra-smooth Graphene Nanoribbon Formation Using Templated,Etching.

[24] Blevins, R. Formula for Natural Frequency and Mode Shape; Krieger; Hellerup, Denmark, 2001.

[25] Belvins, R.D. (1984) Formulas for natural frequency and mode shape. R.E. Krieger.

[26] Rakesh Prabhu T., Tarapada Roy, "Finite element modeling of multiwalled carbon nanotube". National Institute of Technology Rourkela,2010.

[27] Zenkour, Ashraf. (2016). Vibration analysis of a single-layered graphene sheet embedded in visco-Pasternak's medium using nonlocal elasticity theory. Journal of Vibroengineering. 18. 10.21595/jve.2016.16585.

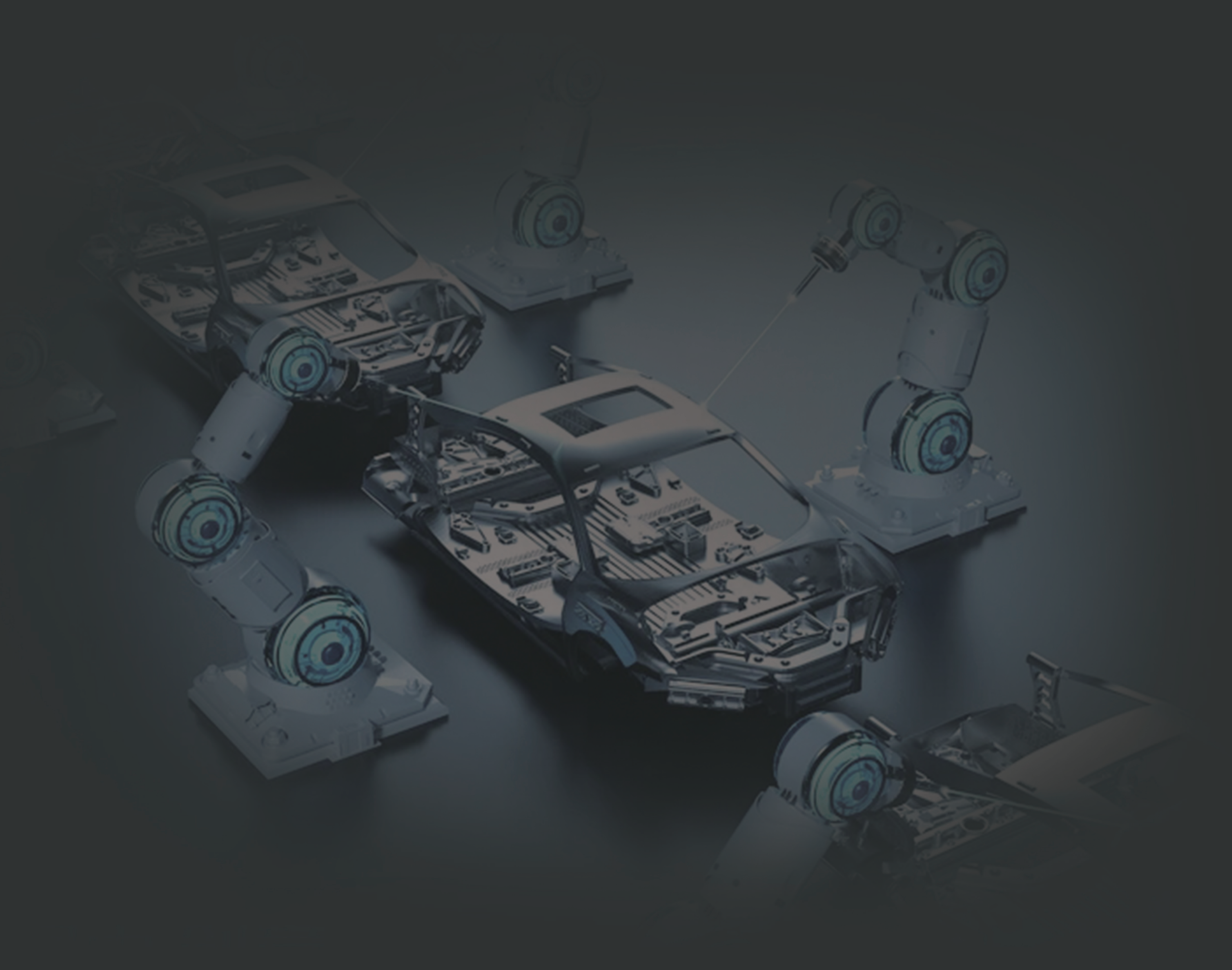

BILINGUAL
PUBLISHING CO.
Pioneer of Global Academics Since 1984

Tel:+65 65881289
E-mail: contact@bilpublishing.com
Website:ojs.bilpublishing.com

ISSN 2630-4945
02
9 772630 494214